Supra-thermal ion emission of solid density ultra-short pulse laser plasma

Inaugural-Dissertation

zur Erlangung des Doktorgrades
der Mathematisch-Naturwissenschaftlichen Fakultät
der Heinrich-Heine-Universität Düsseldorf

vorgelegt von

Jan Riedlinger
aus Düsseldorf

Heinrich Heine
Universität
Düsseldorf

PHASER
PHASE-STABILIZED HEINE LASER

Düsseldorf, März 2026

aus dem Institut für Laser- und Plasmaphysik
der Heinrich-Heine-Universität Düsseldorf

Gedruckt mit der Genehmigung der
der Mathematisch-Naturwissenschaftlichen Fakultät der
Heinrich-Heine-Universität Düsseldorf

Berichterstatter:

1. Prof. Dr. Georg Pretzler
   Institut für Laser- und Plasmaphysik
   Heinrich-Heine-Universität Düsseldorf

2. PD Dr. Götz Lehmann
   Institut für Theoretische Physik I
   Heinrich-Heine-Universität Düsseldorf

Tag der mündlichen Prüfung: 10.07.2026

Abstract

Unconfined, high-energy-density laser plasmas induced by ultra-short laser pulses are known to emit broadband ion spectra in terms of species and their kinetic energy. Under the right conditions, the interaction of such femtosecond laser pulses, in the sub $10^{18}\,\mathrm{W\,cm^{-2}}$ regime, with a solid generates ion emission of bimodal nature, which consists of a slower thermal, and faster supra-thermal part. The main objective of this thesis is to optimize the ion source in terms of the supra-thermal emission and reveal information which they carry about early state plasma properties. Therefore, the first sub-goal of this thesis is to develop an optimized diagnostic and evaluation scheme, which is designed for this specific application.

The diagnostic of choice is the Thomson Parabola method, which is well studied for the particle energies in the MeV range. In this work, however, the spectrometer is required to function down to energies of a few keV. Advancing into this regime requires an accurate knowledge of the spectrometer fields, which were precisely determined by simulations and measurements. Furthermore, the dynamic range was substantially increased by adopting a compact electromagnet instead of a permanent one. We demonstrate how the field parameters can be chosen for obtaining exceptionally broad spectra, while keeping the energy uncertainty minimal. With such a precise spectrometer, together with the developed special numeric methods, we were able to study the conditions to obtain supra-thermal ion emission.

Here, emphasis is placed on the laser intensity, fluence, and duration, and their influence on the ion properties. For this purpose, supra-thermal emission is generated over a wide range of laser parameters in single- and double-pulse configurations.

A key aspect of such plasmas is the high electron density paired with a steep density gradient at the target-vacuum interface. These high densities result in fast thermodynamic equilibration, compared to the time-frame of the emission. Thus, the results are analyzed using the Saha equations to determine the prevalent plasma conditions during emission, assuming local thermodynamic equilibrium (LTE). Thereby, the temporal and spatially localized nature of the ion ejection mechanism is leveraged to obtain a snapshot of the plasma temperature and density in early states of the plasma.

Additionally, one dimensional hydrodynamic simulations were performed using the MULTI-FS code to gain insight into the plasma evolution on picosecond timescales, to compare the results to the experimental findings, and to reaffirm the LTE assumption. The presented results highlight the optimal laser conditions, as well as limitations, to improve the prospects of laser-based ion sources for possible future applications.

Contents

Chapter 1

Introduction

Laser-plasma based ion sources span over numerous experimental geometries and parameters [1, 2], providing a broad range of particle energies. For example, pulsed lasers with Joules of pulse energy can produce MeV-ions in TNSA experiments [3], mJ-pulses on thin foils yield hundreds of keV per particle [4], while mJ-pulses on bulk targets generate tens of keV [5]. Laser generated ions, and also neutral particles in the plasma plume, are used in applications like laser induced mass spectroscopy (LIMS) [6] and surface coatings [7]. However, there are also early developments in radiobiology [8] with laser accelerated MeV carbon ions. Another field of possible future applications is SiC surface modifications, which rely on keV carbon ions [9, 10, 11]. In laser based accelerations, the emitted ions are ejected on time scales similar to the laser's pulse duration, and usually consist of multiple species with broad energy ranges.
Such sources can be roughly divided into thermal, supra-thermal [12], and field acceleration [13]. With laser pulse durations below picoseconds, high intensities and fluences are achieved, compared to longer pulse durations. In this regime, the pulse flank rises fast compared to the thermalization time. When such a pulse interacts with a solid-density target, a solid-plasma transition is initiated some time before the peak intensity of the pulse is reached. The remaining pulse then interacts with the density gradient of this existing pre-plasma. If the density gradient is sufficiently steep, part of the transient laser energy is converted into a much longer-lived field structure of a charged layer [14]. In the case of a sufficiently thin target, ions are ejected from the backside, as in target normal sheet acceleration (TNSA) [15]. While this technique has been studied thoroughly [16], the data regarding emission of the illuminated side of solid density slab targets is still lacking. In this setup, a charged layer is driven by a laser pulse in an expanding pre-plasma near the critical density[17, 18]. This temporary space charge displacement then accelerates the ions perpendicularly into and away from the target surface [19, 20]. The thereby

resulting kinetic energies of the accelerated ions are a product of the electric field strength in the charged layer and its lifetime, similar as in TNSA [21, 16, 22]. Additionally, thermokinetic forces act on the particles due to strong, localized heating by the laser. In this mix of processes, it is not trivial to identify the dominant ones. Thus, the goal of this work is to study the frontside emission with respect to the laser properties for a better understanding of the acceleration mechanism.
To examine the charges and kinetic energies, different diagnostics have been developed, like film stack [23], time-of-flight [24], or Thomson parabola methods. Due to the nearly simultaneous emission, the time-of-flight technique is challenging, as the spectra of the individual species must be deciphered from the signal [4]. In this case, the **T**homson **p**arabola **s**pectrometer (TPS) [25, 26, 27], which relies on parallel electric and magnetic fields, is best suited because of its almost unambiguous mapping of the ions onto the detector. However, accepting a wide range of ion parameters requires variation of both the E- and the B-fields. While the electric field is easy to vary by the voltage applied, multiple groups have further improved the capacitor geometry to increase the dynamic range [28, 29, 30, 31]. Varying the magnetic field is a more challenging task, since usually permanent magnets are employed for setting up the magnetic field. One solution is incorporating a dynamic yoke to adjust the magnetic field strength [32]. Introducing an electromagnet for generating the B-field is another flexible option [33, 34]. So far, TPS developments have mainly focused on particles in the MeV range. However, the supra-thermal regime in this work is expected to be composed of keV particles. Thus, an objective of this work is developing a highly precise and versatile electromagnetic TPS, specifically designed for laser generated ion emission in the keV to MeV range.
One challenge in laser based plasma acceleration is efficiently transferring pulse energy to the electrons in a way that leads to propulsion of the ions instead of vaporization or laser reflection. Previously, single pulse picosecond- and tens-of-fs-lasers were used, which initiate the plasma at a quite undefined point in time [35, 5]. This prevents the study of key aspects, such as the importance of the pre-plasma development. Therefore, the objective is to use down to 8-fs laser pulses, in combination with a well-defined pre-pulse of known temporal advance in order to optimize the pre-plasma conditions.
Ions accelerated from the plasma exceed thermal velocities [36] and the speed of sound [37]. The acceleration is expected to occur predominantly within proximity to the critical density, where the largest fraction of the pulse energy is absorbed [38]. This results is a bimodal energy distribution [39], with a low-energy part due to vaporization and a fast, supra-thermal part. Depending on the local plasma conditions, the thermalization time of the electronic subsystem is comparable, or even shorter, to the picosecond acceleration time of the ions [40]. At the critical density,

the surrounding electrons thermally relax on time scales close to tens to hundreds times the plasma period [40, 41]. This translates to times of only tens of femtoseconds for close to critical density plasma. The heavy particles diffuse on picosecond time scales [42, 43, 44] when the **c**harge **s**tate **d**istribution (CSD) is already determined by the electronic subsystem. Therefore, ions in the high density zone of the plasma experience thermalization in terms of charge states before they reach terminal velocity. Thus, the thermal relaxation affects the emission in terms of kinetic energy, as well as ion species and fast neutrals. During expansion, the ions traverse through an outer section of the plasma where the collisional frequency becomes too low to sustain thermodynamic equilibrium [45, 46]. From this point onward, the charge distribution of the ions becomes decoupled from the present plasma conditions. This is called freezing of the CSD, which can be assigned an effective temperature and density combination [47, 45, 46].
Generally, the experimental determination of laser plasma parameters is a challenging task in laser-solid interactions, as temperature and density vary over many orders of magnitude within only picoseconds and nanometer to micrometer length scales. For temperatures in the tens of eV and close to solid densities, probing with X-rays is one option [48, 49], given a sufficient transmission of the target. Other methods rely on line emission to determine these properties [50]. However, it can only be used at lower temperatures, when the visible lines are relevant [51]. In the early, high-density, high-temperature phase of the plasma, the parameters decrease rapidly; therefore, diagnosing them requires high temporal resolution. To resolve these issues, this work aims to exploit the freezing of the CSD to recover this density and temperature at early plasma stages, and thereby providing insights into the dynamics of fs laser-induced plasmas, which are complemented by independent hydrodynamic [52] and freezing simulations.

Chapter 2

Fundamentals

In this chapter, physical facts that are relevant to the following experiments and their implications are summarized. The description follows the chronological order of events in our experiments.
At the beginning of the chain, there are the **l**ight **a**mplification by **s**timulated **e**mission of **r**adiation (laser) pulses, which are manipulated as desired and used to heat a solid density target. The target then undergoes a phase change to develop into a plasma. This plasma then passes through different regimes as it evolves temporally and spatially. Eventually, a part of the plasma mass leaves the bulk as energetic ion emission. Upon leaving the plasma, these ions pass through a variety of local plasma conditions before they arrive at the spectrometer, which is used to separate them by kinetic energy and charge.

2.1 Mode locked laser pulses

The foundation of laser pulses are described by the Maxwell equations:

$$\vec{\nabla}\vec{E} = \frac{\rho}{\epsilon_0} \tag{2.1}$$

$$\vec{\nabla}\vec{B} = 0 \tag{2.2}$$

$$\vec{\nabla} \times \vec{E} = -\frac{\partial \vec{B}}{\partial t} \tag{2.3}$$

$$\vec{\nabla} \times \vec{B} = \mu_0 \left(\vec{j} + \epsilon_0 \frac{\partial \vec{E}}{\partial t} \right). \tag{2.4}$$

Here, $\vec{E}$ and $\vec{B}$ are the electric and magnetic fields, while ρ and $\vec{j}$ are the charge and current density. Under vacuum conditions $\rho, j = 0$, the wave equation for the electric field E can be

derived:

$$\left(\frac{1}{c^2}\frac{\partial^2}{\partial t^2} - \triangle\right)\vec{E} = 0. \tag{2.5}$$

Here, $c = 1/\sqrt{\mu_0 \epsilon_0} \approx 3 \cdot 10^8\,\mathrm{m\,s^{-1}}$ is the vacuum speed of light. The solutions of interest are of the form

$$\vec{E}(\vec{r}, t) = \vec{E}_0 \exp\left(-\mathrm{i}(\vec{k}\vec{r} - \omega t)\right) \quad , \tag{2.6}$$

with $\omega = c\,k$. This ansatz is separable into an time and space term $E(r,t) = A(r)T(t)$, which can be inserted into eq. (2.5) to obtain the Helmholtz equations:

$$\left(\triangle + k^2\right)A = 0 \tag{2.7}$$

$$\left(\frac{1}{c^2}\frac{\mathrm{d}^2}{\mathrm{d}t^2} + k^2\right)T = 0 \quad . \tag{2.8}$$

This allows an independent discussion of the solution in the time and space domain in the upcoming subsections. Note that the wave and Helmholtz equations can be derived analogously for the magnetic field. However, for the scope of this work, only the electric field is described.

2.1.1 Description in the time domain

First is the description of the time-depended part. In one dimension, the solution of eq. (2.8) in complex notation is:

$$E_\omega(t) = E_{0,\omega} \exp\left(\mathrm{i}(\omega t - \phi_\omega)\right). \tag{2.9}$$

E points in the direction of the polarization, perpendicular to $\vec{k}$, with the amplitude $E_{0,\omega}$, the frequency of the wave ω, and a frequency dependent offset in phase ϕ_ω. In the case of laser pulses, multiple, on the order of 10^6 for a mode locked oscillator, of these modes with different ω overlap spatially, which is depicted for a 30 select modes with a frequency of about $2.35 \cdot 10^{15}\,\mathrm{rad\,s^{-1}}$ ($\lambda = \omega/(2\pi c) = 800\,\mathrm{nm}$) and varying field strength in Figure 2.1. The electric field of the superposition is then:

$$E_p(t) = \sum_\omega E_\omega(t). \tag{2.10}$$

Note that, due to the linearity of eq. (2.8) in T, the sum of solutions is again a solution.
Assuming all the modes are in phase, E_p is close to zero most of the time. On regular time intervals τ_{rep} however, constructive interference occurs. These events can be sufficiently approximated by a Gaussian shape for times smaller than $1/\tau_{\mathrm{rep}}$:

$$E_p(t) = \tilde{E}_0 \exp\left(-2\ln 2\left(\frac{t}{\tau}\right)^2\right)\exp\left(\mathrm{i}(\omega t - \phi_{\mathrm{cep}})\right) \quad . \tag{2.11}$$

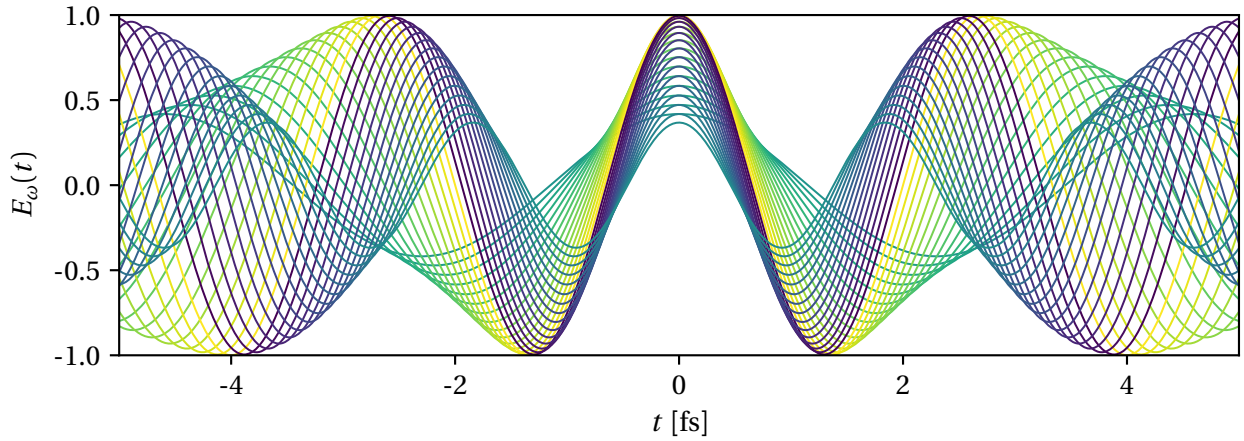

Figure 2.1: Electric field of the sum of modes on a time scale smaller than the repetition rate. Note that all modes are locked at the time $t = 0$.

Here, τ is the pulse duration in terms of the **f**ull **w**idth at **h**alf **m**aximum (FWHM) of the pulse intensity, ϕ_{cep} is the so called carrier envelope phase, and $\tilde{E}_0$ is the peak electric field, which is the sum of the individual $E_{0,\omega}$. This interference is shown in Figure 2.2 on a small ($\ll \tau_{\text{rep}} \approx 0.5$ ps), and large ($\sim 4\tau_{\text{rep}}$) timescale.
Hence, the vacuum intensity $I(t) \propto E(t)^2$ can be expressed as:

$$I(t) = I_0 \exp\left(-4\ln 2\left(\frac{t}{\tau}\right)^2\right), \tag{2.12}$$

with the peak intensity I_0, and the Gaussian shaped pulse envelope, which is narrower than the one of the electric field.

2.1.2 Description in the frequency domain

As initially stated, this is an approximation which relies on the modes being in phase. Often, however, the spectral phase is somewhat nonlinear due to properties of the laser system, or willingly manipulated to modulate the pulse shape and intensity. In these cases, the zero phase approximation fails, the consequences of which are best treated in the frequency domain.
Because the pulses rely on superposition of multiple frequency modes, the description in the frequency domain is inevitably coupled to the time domain. Both ways are related to each other by **F**ourier **T**ransform (FT):

$$\mathscr{F}[E_p(t)] = \tilde{E}(\omega) \quad , \tag{2.13}$$

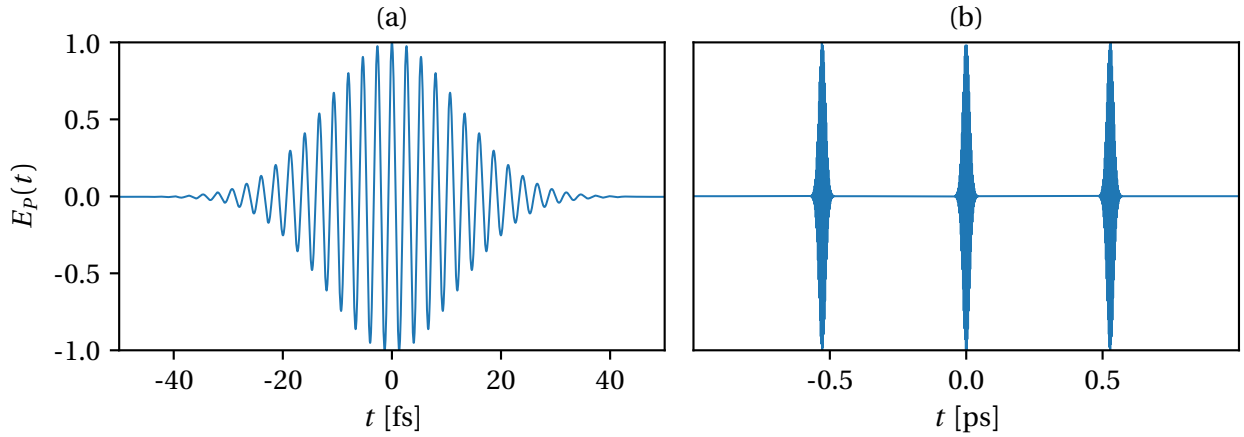

Figure 2.2: Electric field of the sum of modes on a time scale smaller (a) and larger (b) than the repetition rate.

with the complex spectral electric field

$$\tilde{E}(\omega) = E(\omega)\exp\left(\mathrm{i}\phi(\omega)\right) \quad . \tag{2.14}$$

Here, $\phi(\omega)$ is the spectral phase. Because the FT of a Gaussian of width τ is a Gaussian of width $1/\tau$, it becomes clear that for a short pulse a certain spectral width $\Delta\lambda$, sometimes called bandwidth, must be given. A result of this relationship is the pulse-bandwidth product [53]:

$$\tau\Delta\omega = 2\pi c_B. \tag{2.15}$$

c_B is a shape dependent numerical constant, with a value of 0.441 in the case of a Gaussian [53]. Transformation into a wavelength bandwidth limit then gives: $\tau\Delta\lambda \approx 900\,\mathrm{nm{\cdot}fs}$. Therefore, to create a pulse of 30 fs, it must posses a bandwidth of at least 30 nm. Note that, for non-Gaussian spectra, the value on the right hand side of the equation changes.

2.1.3 Dispersion

Now, in the case of non bandwidth limited pulses, any deviations from a linear function of the spectral phase $\phi(\omega)$ change the pulse shape. While the spectral phase can take any intricate shape, a Taylor expansion

$$\phi(\omega) = \sum_{n=0}^{\infty} \frac{(\omega-\omega_0)^n}{n!} D_n \tag{2.16}$$

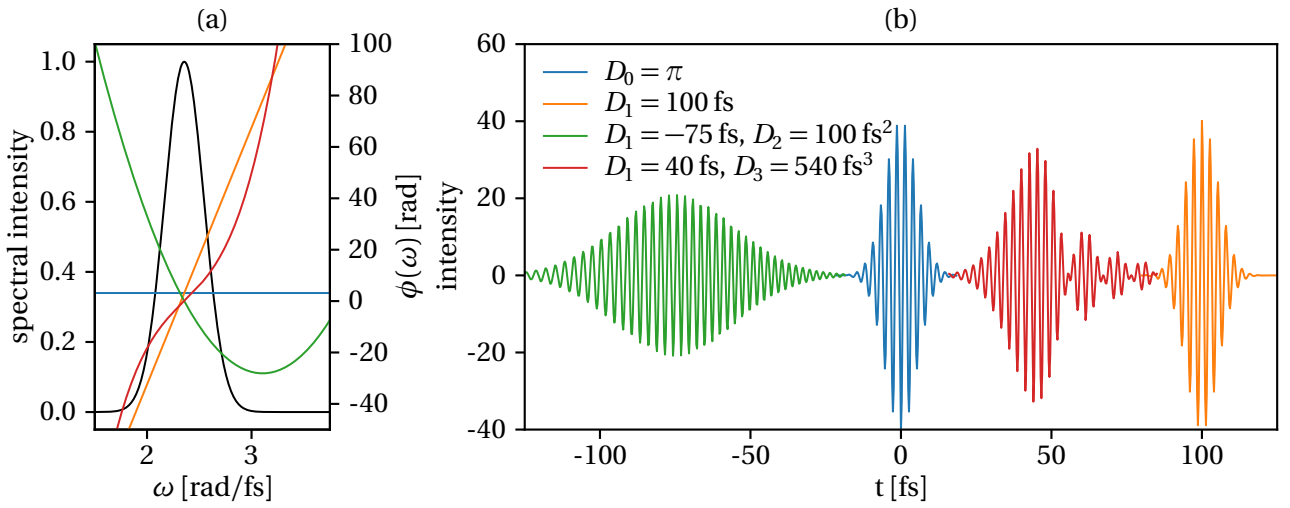

Figure 2.3: (a) Spectrum centered at 800 nm (black curve), and a variety of spectral phases (colors) of order one to three. (b) Pulses resulting from the spectrum and phase combination.

is a commonly used method to discuss the effects of nonlinear contributions.
The

$$D_n = \left(\frac{\mathrm{d}^n \phi(\omega)}{\mathrm{d}\omega} \right)_{\omega=\omega_0} \tag{2.17}$$

are called dispersion coefficients of the n-th order with the units $[D_n] = \mathrm{fs}^n$. Note that only orders $n \geq 2$, shape the pulse as D_0 just changes the pulses **c**arrier **e**nvelope **p**hase (CEP), and D_1 shifts the pulse linearly in time. D_2 stretches the pulse and causes a frequency sweep, the chirp. $D_{n>2}$ usually cause pulse deformations such as pre- or post-pulses. These effects are illustrated in Figure 2.3 for a spectrum that has the same central wavelength as one from a titan sapphire laser. A D_2 of 100 fs^2 is approximately equivalent to 2.8 mm fused silica. While this example already highlights the importance of dispersion control, note that it is even more drastic in terms of intensities. For close-to Gaussian spectra and dominant D_2, the pulse duration can be estimated using

$$\tau = \tau_0 \sqrt{1 + \left(4 \ln 2 \frac{D_2}{\tau_0^2} \right)^2} \quad . \tag{2.18}$$

For ruggedly shaped spectra, however, the temporal pulse profile may become wildly shaped if dispersion is present. In these cases, the FWHM is not a proper metric to judge the duration. Hence, the following equation is used instead throughout most of the work here.

$$\tau \approx \int_{-\infty}^{\infty} \frac{I(t)}{I_{\max}} \mathrm{d}t \tag{2.19}$$

For Gaussian shaped pulses this equation computes to $\tau \approx 1.06$ FWHM. In practice, not only the spectral envelope, but also the phase, is often non-analytically shaped.

Therefore, actual measurements of the pulse shape are inevitable. To do so, a variety of devices, such as the **s**ectral **p**hase **i**nterferometry for **d**irect **e**lectric-field **r**econstruction (SPIDER) [54], **f**requency-**r**esolved **o**ptical **g**ating (FROG) [55, 56], d-scan (dispersion scan) [57], are available. The results of the SPIDER measurements are presented in later chapters.

2.1.4 Description in spatial domain

The spatial part of the solution of the wave equation $A(r)$ can generally take many shapes, associated with Laguerre-Gaussian or Hermite-Gaussian polynomials [58], depending on the waveguides, such as laser cavities or a hollow core fiber.
Lasers mainly output transverse electromagnetic (**t**ransvers **e**lectromagnetic **m**odes (TEM_{mn})) modes, where m, n denote the order of the polynomial in $A(r)$. Transverse means that neither the electric nor the magnetic field point along the direction of propagation $\vec{k}$. The laser used in this work outputs Gaussian beams (TEM_{00}), for which the spatial part takes the form [59, 60]:

$$A(r,z) = A_0 \frac{w_0}{w(r)} \exp\left(-\frac{r^2}{w^2(r)}\right) \exp\left(-\mathrm{i}\left(kz + \frac{kr^2}{2R(z)} - \psi\right)\right) \quad . \tag{2.20}$$

Here, A_0 is an amplitude,

$$w(r) = w_0 \sqrt{1 + \left(\frac{z}{z_R}\right)^2} \tag{2.21}$$

is the radius of the beam waist, with minimal radius $w_0 = f\lambda/(\pi w)$, $z_R = \pi w_0^2/\lambda$ is the Rayleigh length,

$$R(z) = z\left[1 + \left(\frac{z}{z_R}\right)^2\right] \tag{2.22}$$

is the curvature of the wave fronts, and

$$\psi(z) = \arctan\left(\frac{z}{z_R}\right) \tag{2.23}$$

is the Gouy phase.
Finally, the product of eq. (2.20) and eq. (2.11) is displayed in Figure 2.4 for $\tau \to \infty$ and $\phi_{\mathrm{CEP}} = 0$. In real world scenarios, the beam profiles differ from Gaussian shapes, which can lead to vastly different intensity distributions at the focal spot. Additionally, the polarization might depend on the position in the profile, which is the case in vector vortex beams [61], which are treated in more detail in chapter 5.

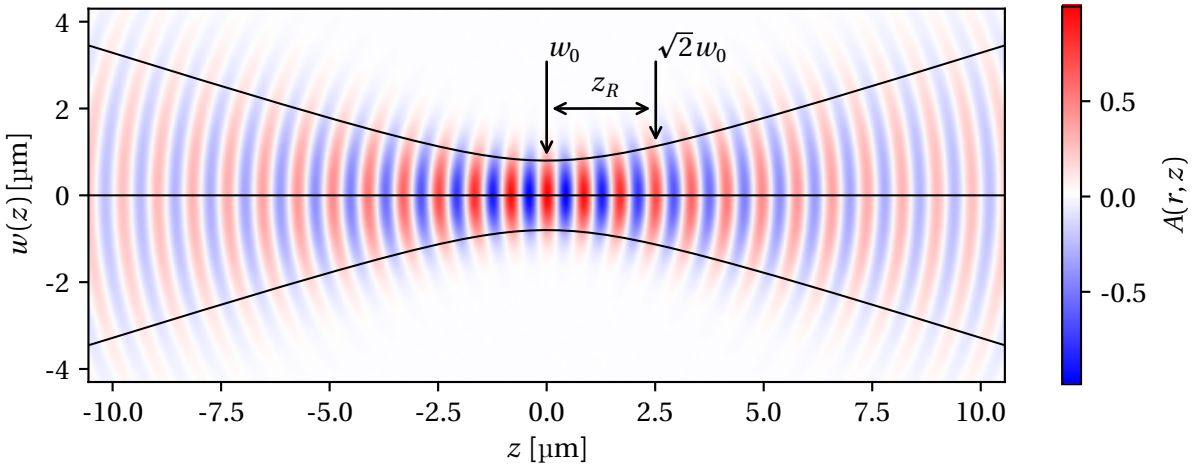

Figure 2.4: Beam waist of a focused Gaussian beam with $w_0 = 0.8\,\mu\text{m}$, $z_R = 2.5\,\mu\text{m}$.

2.2 Plasma initiation

If such a laser pulse is used to illuminate a target, a series of events that depend on pulse and target parameters is started. Eventually, the fluence reaches a threshold where the structure of the solid starts breaking down. Further heating of this "molten" matter may raise the average ionization up until full ionization. Therefore, the state of the target transitions from solid to fluid to plasma. In the fluid phase, however, the average ionization may already be significant. In metal targets, even the solid exhibits plasma properties, due to their conduction band electrons. This makes it difficult to identify a certain point in this process where the plasma phase is started. For this work, it is assumed that the critical fluence on target will be reached at some point before ($\sim$ ps) most of the pulse energy is deposited, due to the finite contrast. Because, shortly after, or even at the initial breakdown, the laser is strong enough to cause ionization of the material, the target is assumed to undergo an instantaneous solid-plasma transition. In this picture, the pulse predominantly interacts with a dense, relatively cold, and quasi neutral plasma cloud instead of the structure of a solid. In the presence of the strong electric field of the main pulse, multiple ionization mechanisms take place.

2.2.1 Ionization

Direct ionization by the laser's field takes place in the form of **t**unnel **i**onization (TI), **b**arrier **s**uppression **i**onization (BSI), and **m**ulti **p**hoton **i**onization (MPI). Which of these is the domi-

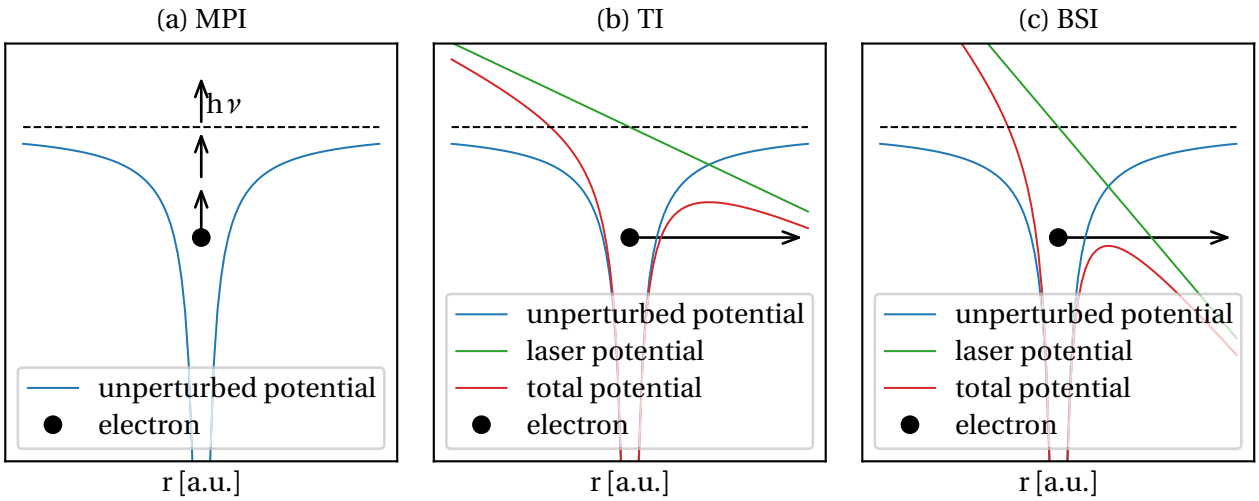

Figure 2.5: Schematic illustrations of (a) multi photon ionization (MPI), (b) tunnel ionization (TI), and (c) barrier suppression ionization (BSI).

nant process can be determined by the Keldysh parameter [62]:

$$\gamma = \frac{\omega\sqrt{2I_P}}{E_0} \quad . \tag{2.24}$$

Here, ω and E_0 are the lasers frequency and field, while I_p is the ionization potential. A value $\gamma \ll 1$ indicates BSI, $\gamma < 1$, TI, while $\gamma \gg 1$ means predominantly MPI. A schematic representation of these three cases is given in Figure 2.5.

Note that the Keldysh parameter is valid only for a limited range of photon energies [63], as such in **vis**ible (VIS) or **n**ear **i**nfra **r**ed (NIR) lasers. As will be shown later on, in the early, dense part of the plasma, ionization is further promoted by **i**onization **p**otential **d**epression (IPD). After the field ionization, the electrons are accelerated according to the electric field. In absence of the laser, they are then able to further ionize surrounding atoms and ions by **c**ollisional **i**onization (CI). As the used NIR laser's electric field tops out at about $10^{11}\,\mathrm{V\,m^{-1}}$, γ becomes smaller than one, which suggests BSI for most of the pulse duration.

Ponderomotive potential

Freed electrons then move in the electric field of the laser. The average kinetic energy, of a such an electron in an oscillating laser field is given by the ponderomotive potential:

$$U_p = \frac{2 \cdot 3.17 e I}{m_e \omega_l} \quad . \tag{2.25}$$

Because the laser field differs spatially and temporally, an electron displaced during one field cycle might not return to its origin. Rather, it is displaced down the gradient of U_p during each

period. Thus, electrons appear to an observer as if they are being pushed away from the high-intensity regions by the so-called ponderomotive force.
While the plasma here will be generally treated quasi neutral, the ponderomotive force is able to establish zones that violate this rule as long as the laser fields are present. Importantly, the ponderomotive potential can be used as a metric for the energy per particle in the plasma during laser interaction. In electron-ion collisions, for example, it is expected that ionization corresponding to energies up to roughly U_p occur.

Critical density

Eventually, the electron density becomes high enough that the plasma frequency exceeds the laser frequency. At this point, the plasma is able to reorganize itself fast enough to screen the transient laser field. This density is called the critical density:

$$n_{\text{crit}} = \frac{\epsilon_0 m_e \omega_l}{e^2} \quad . \tag{2.26}$$

This critical plasma is established during the rising pulse flank, finite pulse contrast, or by a dedicated pre-pulse. If n_c is exceeded, the laser does not propagate further into the plasma, which leads to reflection and absorption.

2.2.2 Absorption

The absorption processes deemed most important are summarized in the following. While they differ in detail, they can be simplified to two principal steps. In the first one, electrons (single or collectively) are set in motion by the laser field. Subsequently, they collide with colder or even stationary atoms, ions, and other electrons, and thereby transfer energy from the laser to the plasma.

Skin-Effect

The Skin-Effect appears if the plasma-vacuum interface consists of a steep, step-like density gradient up to overcritical height, similar to an unperturbed conductor surface. Even though the critical density is exceeded, some of the laser light is able to tunnel into the plasma according to Lambert-Beer's law on a $\sim 10\,\text{nm}$-scale. In this picture, electron motion within the plasma is induced by the laser. This motion is not free, because they scatter on surrounding atoms, ions, and electrons [64]. Thus, they underlay a resistance, as can be described by the Drude-model or Spitzer resistivity. This friction between the driven electrons and proximate particles results in

energy transfer from the laser to the temperature of the plasma in close to the critical density. For higher intensities $> 10^{18}\,\mathrm{W\,cm^{-2}}$, normal skin effect (NSE) turns into the anomalous skin effect (ASE) [65], with an increased skin-depth.

Inverse Bremsstrahlung

If the density gradient is more shallow and below critical, the laser can traverse the plasma. This occurs, for example, in the outer realm of an initially solid density plasma that has expanded for a long time ($\sim 10\,\mathrm{ns}$). This is a favorable environment for inverse Bremsstrahlung. Similar to the first heating mechanism, in the first step of this type of heating, the electrons gain energy in the electric field exerted by the laser [38]. Then, they lose this energy again in collisions with surrounding ions, which are too inert to move correspondingly. Therefore, the light wave loses energy as the plasma heats up along the propagation. Since the collisional frequency in a plasma increases with density, but decreases with temperature, inverse Bremsstrahlung works best at low temperatures, and high, but subcritical, densities.

Resonant and not so resonant absorption

Resonant absorption occurs when the incident laser has an electric field component perpendicular to the target. This is the case for an incident angle $\neq 0$ and p-polarized laser light. If the density gradient is of intermediate steepness and tops out above critical, resonant and not so resonant absorption, also called Brunel absorption, is possible. In this setting, the density gradient causes a gradient in of the refractive index. Consequently, the trajectory of the light is bent away from the target before it makes contact with the critical density.
During reflection, a fraction of the light tunnels behind the critical surface in the form of an evanescent wave, where an electron wave is excited [66, 38] either directly by the electric field or ponderomotive force. The electron wave propagates into further into the target, where it collides with the plasma bulk.
In case of the not so resonant absorption, the electrons are pulled away from target first. In the next half cycle of the laser, they are accelerated back into the plasma, where they deposit their energy by collisions [67].

2.2.3 Thermalization

Once the plasma is left by the laser and accelerated electrons are ejected, thermal relaxation starts. As will be shown in this section, this can be a surprisingly fast process. In a plasma, the

collision rate $\nu_{ei} = 1/\tau_{ei}$ can be estimated by the Spitzer electron-ion collisional time [68]

$$\tau_{ei} = \sqrt{\frac{m_e(\pi k T_e)^3}{2}} \frac{12\epsilon_0^2}{n_e Z_{\mathrm{av}} e^4} \frac{1}{\ln \Lambda_C} \quad . \tag{2.27}$$

Here, $\Lambda_C = 12\pi\lambda_D^3 n_e$ is the Coulomb logarithm, which is of the order of ~ 1 for laser plasma of high density. Inserting $T = 10$ eV and $n_e = n_c \approx 2 \cdot 10^{27}$ m^{-3} yields $\tau_{ei} \approx 5$ fs. The electron-electron collisional time $\tau_{ei} \approx \sqrt{2} Z_{\mathrm{av}} \tau_{ee}$ is even shorter [69]. It should be noted that the Spitzer collision rate is a momentum collision rate, describing how frequently a test particle (first position in the index) changes its initial direction by a right angle in the presence of a field particle (second position in the index), and not how often two particles generally scatter. Therefore, these rates are already weighted by momentum exchange and $\nu_{ei} \sim (m_i/m_e)\nu_{ie} \sim \sqrt{m_i/m_e}\,\nu_{ii}$. Considering the impulse transfer is high in ee-encounters, thermalization of the free electrons is expected to occur on a time scale similar to τ_{ee}.

It has been demonstrated that, on time scales of $10-100/\omega_p$, the electrons redistribute their energy until no principal axis of motion exists anymore [70, 41]. This translates to ~ 50 fs or $10\tau_{ei}$ for $\omega_p = \omega_c$, in the case of a 800 nm laser. On time scales of picoseconds ($\sim \tau_{ie}$), thermal motion of the atoms and ions occurs as well [42, 43].

Thus far, only free electrons were treated. However, the bound electrons are also part of the electronic subsystem that determines the charge distribution in plasma. As most of the collisions involve electrons, the charge distribution is assumed to depend only on the electron density and temperature. Therefore, the **l**aser **i**nduced **p**lasma (LIP) is treated as an **e**lectron **e**xcitation **k**inetic (EEK) dominated plasma [71]. This means it is decoupled from the ion temperature, for example. Here, the excitation time

$$\tau_{12} \approx \frac{1}{n_e \langle \sigma_{12} v \rangle} = \frac{6.3 \cdot 10^4}{n_e f_{12} \langle \overline{g} \rangle} \Delta E_{12} \sqrt{k T_e} \exp\left(\frac{\Delta E_{12}}{k T_e}\right) \quad , \tag{2.28}$$

of a bound state can be approximated using the gaunt factor $\langle \overline{g} \rangle$, and the absorption oscillator strength f_{12}. $\langle \overline{g} \rangle$ is of the order of ~ 0.1 for $E_{\mathrm{kin}} \sim \Delta E$, in the case of positive ions [72]. f_{12} varies roughly in the range of $\sim 1-10^{-2}$ [73, 74]. Using the same typical LIP parameters as before ($T = 10$ eV, $n_e = n_c \approx 2 \cdot 10^{27}$ 1/m^3, $\Delta E_{12} = 9.3$ eV), $\tau_{12} \approx 20 - 2000$ fs is found. In this example, and for reasonable temperatures, it holds that $\tau_{12} > \tau_{ei}$. Therefore, the thermal relaxation time can be approximated by $\tau_{\mathrm{rel}} \approx \tau_{12}$. Note that f_{12} is derived mostly from experimental data, which might not be complete for the required species. To resolve this, it is simply assumed that $f_{12} = 0.1$. However, due to the ongoing expansion, as well as loss of energy to radiation, **c**omplete **t**hermodynamic **e**quilibrium (CTE) is not reached. Rather, the plasma consists of many zones that are in thermodynamic equilibrium with the neighboring ones, and only at a certain temperature, and

for a short period of time, which is called **t**hermodynamic **e**quilibrium (TE). This can be satisfied even with a flow of energy across the system boundaries, as long as all distributions can be described using the same temperature.

In LIP radiation losses occur in each zone since the surrounding plasma is not opaque for all frequencies involved in black body radiation. If the energy losses due to radiation are small compared to other processes, the Planck function changes, but the kinetic energy of the involved particles is still equally partitioned across the degrees of freedom and Boltzmann distributed. This equilibrium is called **l**ocal **t**hermodynamic **e**quilibrium (LTE). This is an important aspect for this work, since, in an LTE, the charge distribution follows the Saha equations. Additionally, the ion and electron temperatures can differ in LTE, which is called a two temperature plasma. This can occur naturally in LIP due to the different thermalization times post laser exposure, as discussed previously. Whether or not it is possible for an LTE to exist in a plasma zone can be evaluated by the McWhirter criterion [71, 75]:

$$n_e > 1.6 \cdot 10^{12} \sqrt{T} (\Delta E_{nm})^3 \, [\mathrm{cm}^{-3}] \quad . \tag{2.29}$$

Here, ΔE_{nm} is the energy transition of the levels n and m, participating in the equilibrium. While there is a more precise criterion from Hey [76], the McWhirter criterion is probably the most prominent, and will be used here as they have the same scaling. Note that the criterion's meaning is limited to whether or not an LTE *can* exist, as opposed to whether it actually exists.

For an LTE to exist, the change in intensive variables, such as density and temperature, must happen slowly when compared to the thermalization time. Therefore, two additional criteria must be satisfied for LTE in a transient and spatially varying plasma. The temporal criterion states that T and n_e change slowly when compared to the relaxation time $\tau_{\mathrm{rel}} \approx \tau_{12}$ [77, 78]:

$$\frac{T(t+\tau_{\mathrm{rel}}) - T(t)}{T(t)} \ll 1 \tag{2.30}$$

$$\frac{n_e(t+\tau_{\mathrm{rel}}) - n_e(t)}{n_e(t)} \ll 1 \quad . \tag{2.31}$$

Similarly, the spatial criterion states that T and n_e are approximately constant over the diffusion length $\lambda = \sqrt{D\tau_{\mathrm{rel}}}$:

$$\frac{T(x+\lambda) - T(x)}{T(x)} \ll 1 \tag{2.32}$$

$$\frac{n_e(x+\lambda) - n_e(x)}{n_e(x)} \ll 1 \quad , \tag{2.33}$$

where D is a diffusion coefficient that can be approximated by [71]:

$$D \approx 3 \cdot 10^{19} \frac{k T_e}{n_e m_u} \quad \left[\frac{\mathrm{cm}^2}{\mathrm{s}} \right] \quad . \tag{2.34}$$

Here, m_u is the relative atomic mass of the heavy particle ($m_u = 12$ in the case of carbon), n_e is given in cm^{-3}.
The relaxation time can be approximated considering the cross section σ_{12} for the energy transition ΔE_{12} between the ground state 1 and first excited level 2 [71]:

$$\lambda = 1.4 \cdot 10^{12} \frac{(kT_e)^{3/4}}{n_e} \sqrt{\frac{\Delta E_{12}}{m_u f_{12} \langle \overline{g} \rangle}} \exp\left(\frac{\Delta E_{12}}{2kT_e}\right) \quad . \tag{2.35}$$

Due to the exp-function, the relaxation time strongly depends on the transition energy and temperature. This means that, if the plasma transitions from hot to cold, the higher ionization orders fall out of equilibrium before the lower ones.
Inserting the same $kT_e = 10\,\mathrm{eV}$ and $n_e = n_c$ in the equation for the diffusion length, $\lambda \approx 0.2\,\mathrm{nm}$ is obtained. This is much shorter than the density gradient found by molecular dynamic simulations [79], which are on the scale of 100 nm during picoseconds ($\gg \tau^{ei}$) post ignition. This indicates that LTE is a reasonable assumption for close to early state LIP. Therefore, the dense part of the plasma passes through a series of LTE stages during expansion and cooling. In outer parts, or later points in time, the plasma eventually falls out of LTE. This region will be investigated in more detail in section 4.8.

2.3 Plasma expansion

2.3.1 Degree of Ionization

If the plasma is in LTE, the present ion species distribution can be estimated using the Saha equations [80]:

$$\frac{n_{i+1} n_e}{n_i} = 2 \frac{U_{i+1}}{U_i} \frac{1}{\lambda_B^3} \exp\left(-\frac{I_i^{\mathrm{eff}}}{k_B T}\right) \quad , i = 0 \ldots Z-1. \tag{2.36}$$

n_i, U_i are the density and partition function of the i-th ion species, λ_B is the de-Broglie wavelength, and $I_i^{\mathrm{eff}} = I_i - I_i^r$ is the effective energy it takes to ionize the i-th species. This energy is comprised of the ionization energy I_i of a single atom/ion, and a term accounting for continuum lowering I_i^r, also called ionization potential depression/reduction.
In order to solve this set of equations for a certain density, temperature combination, the partition functions, as well as the IPD, must be determined. This is a challenging task and still part of active research [81]. Nevertheless, the following section gives an introduction to this topic and explains the steps taken in this work to calculate these quantities.

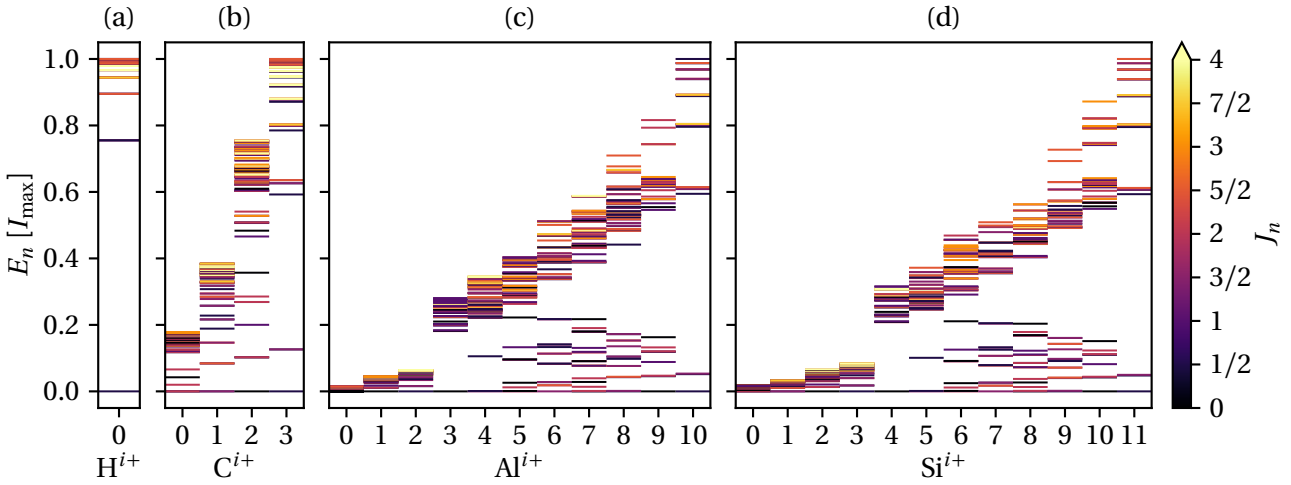

Figure 2.6: (a-d) Atomic and ionic levels and the corresponding degeneracy, as read from the atomic NIST database. For carbon, aluminum, and silicon, only the first four, ten, and twelve species are displayed. Because of the finite line thickness, some levels may be buried.

Partition functions

In terms of the simple case of hydrogen, the atomic partition function U_0^H can be calculated by the well known series [82]:

$$U_0^H = \sum_{n=1}^{\infty} g_n \exp\left(\frac{E_n}{k_B T}\right) \quad , \tag{2.37}$$

with $g_n = 2n^2$ and $E_n = -R_H(1-1/n^2)$. Note that the sum diverges regardless of temperature. However, very high n are of unphysical nature. Recall that the atom radius increases with n^2, which means that for some n^*, the radius becomes larger than the mean interatomic distance at a given plasma density. Beyond this n^*, it would be wrong to attribute this electron as bound to the atom, even though the corresponding energy is lower than the ionization threshold. This effect is called continuum lowering or IPD and will occur as soon as more than one isolated atom is observed.

Figure 2.6 shows all of the available atomic and ionic levels and their quantum number J_n, as found in the NIST database, for a selection of common laser target materials. The degeneracy can then be calculated by $g_n = 2J_n + 1$. As shown, they are apparently, aside from hydrogen, distributed in a random manner, which comes from the complex interactions between the shell electrons. For carbon, one of the here used target materials, an analytical approximation for the partition function exists for a large range of temperatures and moderate potential reductions [83]. At the time of this work, an analytical description does not exist for most materials. Because, at solid densities in plasma, the moderate potential reduction is exceeded, and to be able

to include higher Z atoms, such as aluminum, silicon, or copper, the experimental database of NIST is consulted [84] for the g_n and E_n.
There are a couple of options how the diverging sum can be treated. One is introducing an individual weight w_n to each term, in order to let the sum converge [81]. The other is simply truncating the sum at n^*. The question then becomes, how to choose this number. Again, there are a couple of options [85]. The one discussed here comes down to choosing an IPD according to the type of plasma. Hence, the following section includes a brief discussion regarding this topic. When working with finite experimental data sets, divergence is no issue, of course, but to properly include the IPD even when pressure ionization occurs, the truncation of the partition functions is still important.
As there are different approaches to the IPD depending on the plasma regime, in the following an overview over the different regimes is given.

2.3.2 Plasma regimes

Plasmas appear in a huge parameter range, from low densities at cold temperatures to high density, hot plasma, as shown in Figure 2.7. One interesting aspect of laser-solid interactions is that the plasma is of very transient nature, meaning it runs through many orders of magnitude of temperature and density in a very short time scale. Therefore, the categorization varies depending on the location and time. Note that in illustration 2.7, the stars were added according to solid properties at room temperature (star 1), a temperature estimate based on the ponderomotive potential, and measurements [50] (star 3). This way, a rough trajectory the plasma states take can be drawn. As shown, these states cross multiple boundaries, and hence, a discussion of each regime is inevitable.

Degeneracy

Two key parameters can be derived from the density n and temperature T. Namely, the thermal de-Broglie wavelength λ_B and the Debye length λ_D. The former is a product of quantum mechanics, which states that all particles exhibit wave like behavior. Now, in a plasma, the dynamics change if the wave functions start to interfere. The criterion often used to differentiate such plasmas is a comparison of the volume spanned by the de-Broglie wavelength

$$\lambda_B = \frac{h}{\sqrt{2\pi m_e k_B T}} \quad , \tag{2.38}$$

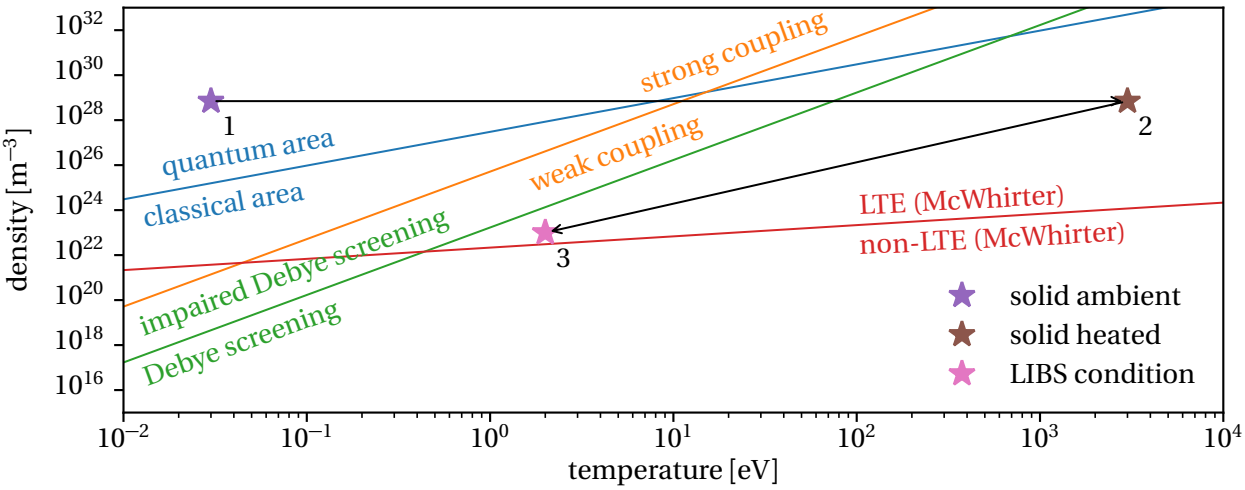

Figure 2.7: Sketch of the plasma trajectory in the temperature-density plane. 1: The target initially sits at solid density and ambient temperature. The energy provided by the laser pulse heats it to the ponderomotive potential. During the heating process, of only fs-duration, the expansion is minimal. The heated solid (2) expands and cools while eventually reaching LIBS conditions (3). This trajectory is only valid if the LIBS plasma is initially overheated, which is usually not done.

and the electron density n_e[86]. In this case, the number of particles per said volume is:

$$N_B = n_e \lambda_B^3 \quad . \tag{2.39}$$

Only if $N_B \ll 1$ quantum effects can be neglected. Otherwise, electron degeneracy sets in. Due to Heisenberg's uncertainty principle, the wave function shrinks with increasing momentum, and therefore temperature. Hence, if the plasma is sufficiently hot, quantum physics becomes negligible again.

Coupling parameter

Since plasma consists of charged particles, they are able to screen electric potentials. The length scale it takes a plasma to so is the Debye length:

$$\lambda_D = \sqrt{\frac{k_B T}{n_e e^2}} \quad . \tag{2.40}$$

With this length, the other key value, the number of electrons per Debye volume, can be derived:

$$N_D = n_e \lambda_D^3 \quad . \tag{2.41}$$

This value is sometimes expressed as the plasma parameter $\Lambda = 4\pi N_D$. It is further linked to the coupling parameter $\Gamma \sim \Lambda^{-2/3}$, which can be calculated for non-degenerate plasma according to

[87]:

$$\Gamma = 2.69 \cdot 10^{-5} Z^2 \left(\frac{n}{10^{12}\,\mathrm{cm}^{-3}} \right)^{1/3} \left(\frac{T}{10^6\,\mathrm{K}} \right)^{-1} \quad . \tag{2.42}$$

This parameter is often used in literature when discussing the validity of a certain IPD in a regime. In a weakly coupled plasma, the Debye volume is densely populated, which means Debye screening occurs. At the same time, interactions between particles are of occasional nature and dominated by collisions. Strong coupling leads to a more continuous inter particle relationship. Figure 2.7 shows these criteria drawn in the temperature density plane. Considering the estimated point 2, it can be seen that the plasma created in this laboratory can be found mostly in the weakly coupled, non-degenerate section post heating.

2.3.3 Ionization potential depression (IPD)

According to these regimes, a suited IPD must be chosen in order to solve the Saha equations. In the case of weakly coupled ones, the potential reduction in compliance with **D**ebye-**H**ückel (DH) theory was derived by minimization of the free energy:

$$I_i^{r,D} = \frac{(i+1)e^2}{4\pi\epsilon_0 \lambda_D} \quad . \tag{2.43}$$

This formulation was introduced by Griem [88] and extended by Ebeling [86], where λ_B was introduced to the denominator in order to comply with the low temperature limit $T \to 0$.
For dense plasma, Debye theory fails, as the number of particles per Debye sphere is too low for proper potential screening. As shown before, this is quite often the case in laser plasma, which is the reason other potential truncations, for example according to the inter particle distances [89], should be chosen. For the strongly coupled regime, **E**cker and **K**röll (EK) have developed a potential reduction based on ion spheres [90]

$$I_i^{r,EK} = c\,\frac{(i+1)e^2}{4\pi\epsilon_0 r_{EK}} \quad . \tag{2.44}$$

Here, $r_{EK} = \sqrt[3]{3/4\pi n_e}$, and c is a constant $c \sim 1$. **E**cker and **K**röll give several values for c ranging from $1.73-3.38$. Because of this uncertainty, simply assuming $c = 1$ is one pragmatic option[91]. **S**tewart and **P**yatt (SP) [92] derived an expression which somewhat unites the result by Griem and EK:

$$I_i^{r,SP} = \frac{3}{2}\frac{(i+1)e^2}{4\pi\epsilon_0\lambda_D}\frac{\left[(a/\lambda_D)^3+1\right]^{2/3}-1}{(a/\lambda_D)^3} \quad , \tag{2.45}$$

with $a = \sqrt[3]{3(z+1)/4\pi n_e}$. Note that in weak coupling limit $a \ll \lambda_D$, the SP model reduces to the DH result up to a constant. For $a \gg \lambda_D$, $I_i^{r,SP}$ approximately resembles the EK result. Note that in

this form, weak coupling is assumed, which is not the case for EK. Considering $I_i^{r,SP}$ is valid where Debye screening is impaired, up to the strong coupling line, this is the reduction best suited for the type of laser plasma treated in this work.
With the reduction, it can be calculated which n corresponds to the effective ionization potential $I_i^{\text{eff}} = I_i - I_i^r$ by [83]:

$$n_i^* \leq \sqrt{\frac{I_i}{I_i^r}} \quad . \tag{2.46}$$

Because the E_n and g_n are read from the database, n^* is chosen such that U is truncated at $E_{n_i^*} \leq I_i^{\text{eff}}$.

2.3.4 Freezing of states

While the ions are ejected from the plasma, they experience zones of less dense and different temperature plasma. Eventually, there comes a point along the trajectory at which the frequency of collisions gets too low to sustain thermodynamic equilibrium [46]. Since the electron velocities are Maxwellian distributed in an LTE, collisions with high energy transfers are less probable. Suppose an atomic particle, which is located in an inner, dense volume of the plasma of constant temperature. Further, assume that, at this initial position, all its atomic and ionic transitions are in LTE and eq. (2.29) is satisfied. If this particle is observed in a time resolved manner, it becomes apparent that it constantly exchanges charges with the surrounding plasma. It randomly cycles charges according to the prevalent plasma conditions, but on average, it has the mean charge state as dictated by Saha. Now, suppose this particle traversed out of the plasma into vacuum. In vacuum, there are no longer collisions, and thus the particle is stuck at the charge state it obtained in its last few collisions, or even last collision. Another way to describe this is by saying the charge state is frozen. Similarly, if multiple particles were assumed, their charge state distribution was frozen. Note that freezing is inevitable as long as the particle ends up in the vacuum. It is important, however, how fast it passed through the density decay (assuming constant temperature). If the particle went from high density to vacuum very quickly, it “feels” the density gradient as a step function. In this case, it did not spend sufficient time at a lower density for its charge state to be reshuffled. It freezes at approximately the mean charge state of the high density area. Whereas, if it passes very slowly, it is exposed to low densities sufficiently long to thermalize. Therefore, the mean charge state which would be measured is dictated by Saha for vanishingly small densities.
For intermediate “velocities”, the state of freezing becomes more complicated. The reason being that the equilibration time ($\approx \tau_{12}$ eq. (2.28)) depends on the excitation energy. As a consequence,

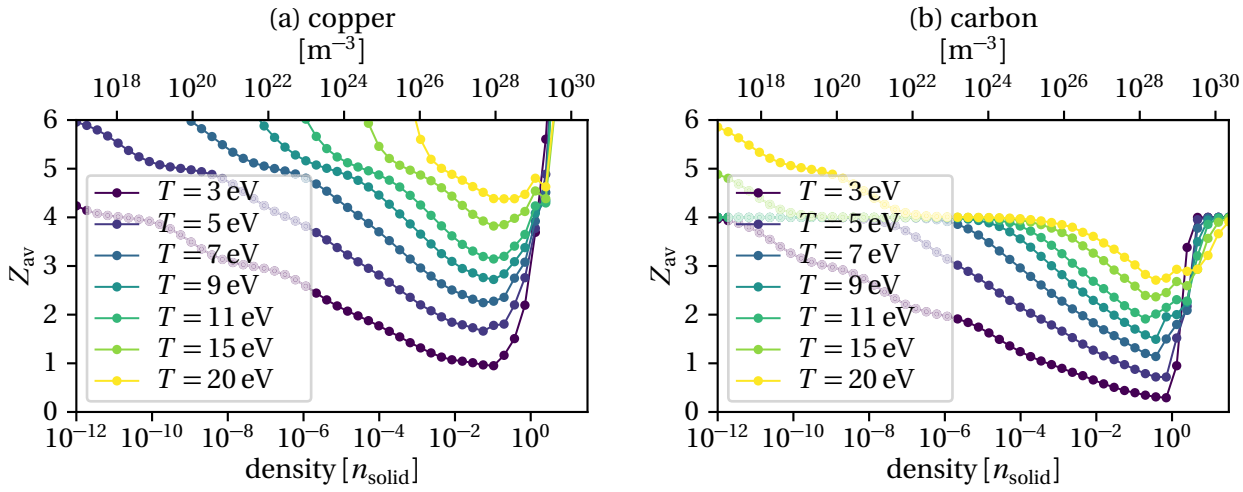

Figure 2.8: (a) Average ionization Z_{av} of copper at different densities and temperatures. (b) Average ionization Z_{av} of carbon at different densities and temperatures. The valley of freezing occurs at about 10 % of the solid density for both materials.

high energy transitions, or high ionization states are the first ones to fall out of LTE, which is the point at which they stop following the Saha equations. Therefore, the observed CSD cannot be described by a single (temperature, density)-pair. To simplify this issue, this work assumes instantaneous freezing [47, 45], whose validity will be discussed in hindsight. It is assumed that the points of freezing lie sufficiently close to one another so an effective temperature and effective density can be assumed [47, 45]. Alterations of the charge state due to random collisions without proper thermalization are also accounted for by the "effective" values.

With this assumption, it is possible, by just measuring the average charge state Z_{av}, to assign a range of values for the plasma temperature and density at the point of freezing. The reason being that not every Z_{av} is possible at each temperature, density (T,n) combination. This can be seen in Figure 2.8, where the average ionization Z_{av} in thermodynamic equilibrium for copper (a) and carbon (b) was calculated according to the Saha equations and SP potential reduction. Note how $Z_{av} = 1$ is never reached for $T > 3$ eV in the copper example. At solid density, which is about $n_{solid} = 7 \cdot 10^{28}$ m^{-3} for many solids, the plasma is highly ionized due to pressure ionization. Upon plasma expansion, Z_{av} drops rapidly to a minimum, which will be referred to as the valley of ionization [45]. Left of the valley is where freezing of CSDs occurs.

By comparing (a) and (b), a few additional observations can be made. In carbon, pressure ionization sets in at higher densities compared to copper, and therefore, higher densities are observable in theory. This makes carbon a good candidate for being used as target material, because it allows to potentially observe high densities.

Finally, it should be noted that the CSD freezing was predominantly studied with vacuum arc cathode discharges. There, the kinetic energies and plasma expansion can be considered rather thermal, while here, the particles undergo additional acceleration. Additionally, the density gradient is steeper because of the short timescales with respect to the point of ignition. Therefore, the model of instantaneous freezing of the CSD is expected to hold better when compared to the arc discharges.

2.3.5 Ablation and acceleration

Since it was previously discussed how the charge states are affected during plasma expansion, this section is dedicated to the mechanism by which target material is removed by laser radiation. Target material removal falls under the general term of ablation. The underlying mechanisms however, change drastically depending on the experimental setup, laser parameters, target parameters, and time scales. Therefore, we divide these mechanisms into ablation and acceleration processes. In ablation, the laser energy is predominantly converted into heat, which then leads to vaporization of the heated matter. This is how most of the material in a laser-solid interaction is removed, which leaves a crater.

Laser-plasma acceleration, on the other hand, is the act of converting laser energy into kinetic energy of particles. Some well established schemes are the **l**aser **w**ake **f**ield **a**cceleration (LWFA)[13] or **t**arget **n**normal **s**heet **a**cceleration (TNSA)[15]. These require special targets, in the form of a uniform gas jet or very thin foils, to function properly. But, if set up correctly, are able to produce MeV kinetic energies.

When using a thick solid target ($d \sim 1\,\mathrm{mm}$) the majority of the material is removed by thermal evaporation. As previously stated, however, some particles might also be accelerated. In this case, the emitted particles include accelerated, as well as evaporated, particles. This becomes apparent if the energy spectrum of the ions is bimodal, with a slower part due to thermal evaporation and a faster, accelerated part. Further, these sections of the spectrum can have varying principle axis of emission and divergence.

There are a few mechanisms that are able to drive a bimodal kinetic energy distribution, the fast part of which will be called the supra-thermal spectrum. On a fundamental level, their origin is either thermal, radiation, or electrostatic pressure, or a combination of those. In the first step, a pre-plasma is ignited using low intensity laser light. This can be either a dedicated pre-pulse, or the rising pulse flank of a single laser pulse. In the second step, the main pulse is reflected in the density gradient at about the critical density. In this area, the energy density is high because the incoming and reflected beams interfere. For a large range of sub-relativistic intensities, from

roughly $10^{15} - 10^{16}\,\mathrm{W\,cm^{-2}}$, and short pulses < 1 ps, the laser is able to create an electric field in a double layer by charge separation due to ponderomotive forces in the density gradient[20, 18, 93]. A positive layer is enclosed by a negative layer on the vacuum and target side. After the layer is established and the pulse is gone, the fields start to collapse by two competing processes. The layers are accelerated towards each other while the positive layer disperses, similar to a **C**oulomb **e**xplosion (CE) [94, 95, 96]. As a result, ions are accelerated out of, as well as into, the target. At higher intensities $> 10^{20}\,\mathrm{W\,cm^{-2}}$, the layer becomes more asymmetric, with a stronger force driving the ions toward the inside of the target, which is known as radiation pressure acceleration hole boring (RPA) [97, 98].
Close to the critical density is also the region where absorption is strongest by the Skin-effect and Brunel absorption. This causes strong local heating of electrons, which are trapped by colder plasma on the target as well as vacuum side. As the heated region is embedded in a density gradient, the inertia on the target side is larger than the vacuum side. This bubble of hot plasma bursts on the vacuum side and thereby pushes the low density side to supra-thermal velocities. Which process dominates is usually not easy to identify, since they occur in similar laser regimes and might take place simultaneously to some extent. The results of a series of experiments will be presented in section 4.6, with the objective of identifying whether thermal or electric potentials cause the supra-thermal emission observed in this work.

2.4 Ion spectroscopy

In order to disperse the ion spectrum into the different species for observation, a suited diagnostic is needed. Such diagnostics can be divided into two parts. One is the dispersive element, which maps ion properties, such as kinetic energy or charge, onto one or two spatial dimensions and possibly time. The second part is the detector, which should be able to detect a wide range of kinetic energies at a large dynamic range. Further, the detector should have known spectral detection efficiency and linear response to the incoming number of particles.
One commonly used option is the **t**ime-**o**f-**f**light (TOF) diagnostic [35], which consists of a drift tube to calculate the particle velocities, paired often with an **m**icro **c**hannel **p**lates (MCP) detector. While it is well suited in many cases, under some conditions, its mapping becomes ambiguous, for example, when different atomic species and/or different ionic states are present with broad energy spectra. Under those conditions, the signal might only be deciphered by adding vast assumptions [4].
A more unique mapping is offered by the TPS technique. Here, the particles are mapped onto

two dimensions instead of one, such that the q/m ratio, as well as the energy distribution, are unambiguous. Since this work requires separate, precise spectra of the various species, the TPS method was chosen. It was adapted to our problem by modifications made to the standard setup. The implementation of the TPS, including the detector, is elaborated upon in the next section.

2.4.1 Thomson parabola spectrometer

A TPS uses parallel electric U and magnetic fields B to deflect particles with mass m according to their energy $\sim v^2$ in one dimension (y), and momentum $\sim v$ in the other (x). With the length of the fields l, and a free flight distance s, the deflections can be approximated:

$$x = \frac{qBl}{mv} s \tag{2.47}$$

$$y = \frac{qUl}{mv^2} s \quad . \tag{2.48}$$

Thus, parabolic traces are drawn on the detector with a slope proportional to m/q. The corresponding equation can be retrieved by eliminating the velocity v from the equations above:

$$y = \frac{mU}{qB^2 ls} x^2 \quad . \tag{2.49}$$

The length of the trace is determined by the present kinetic energies E, which is illustrated in Figure 2.9. In this picture, each black dot represents a distinct kinetic energy.
In practice, the entrance aperture is of finite size d, meaning that the energies are not mapped onto a single point on the detector, but rather a circular shape corresponding to the **p**oint **s**pread **f**unction (PSF) of the experimental setup. This is represented by the green circles. As a consequence, the resolution of the diagnostic becomes finite in terms of q/m, and E.
As a consequence, the ability to resolve the neighboring species $(q \pm 1)/m$ is compromised because the PSFs of the traces may merge. Of course, this happening in practice depends on the actual spectra and fields in the TPS. But, if sufficiently high kinetic energies are present, this will occur as the parabolas converge at the origin.
In Figure 2.9, the shortest distance to the neighboring parabolas is illustrated as blue lines for each black dot. Therefore, if the diameter of the PSF exceeds the length of the blue line, the species cannot be resolved anymore.
The other introduced uncertainty is about the energy. Because of the finite pinhole size and detector resolution, multiple particle energies become indistinguishable as they strike the same location on the detector. In Figure 2.9, this is illustrated by the red lines for each black dot. The red lines demonstrate how long a segment on the parabola is if the energy is varied by ±10%.

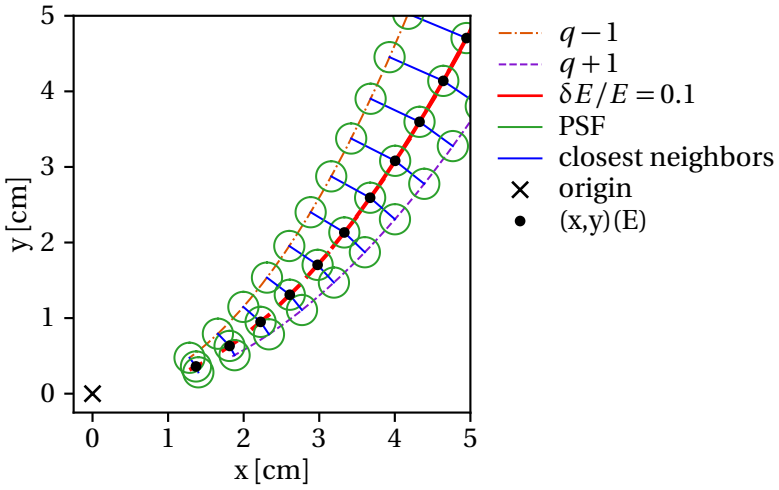

Figure 2.9: Coordinates of a variety of kinetic energies, as dispersed in the TPS (black dots). Traces of the neighboring ion species (dashed lines in orange and lavender), as well as the closest points to the black dots (blue lines). Point spread function (green circles) and spread of a $\delta E/E = 0.1$ energy uncertainty along the parabola (red lines). The origin is represented by the black X at (0,0).

Due to the nonlinearity of the mapping, the lines become shorter for high energies. This means that energies are less separated closer to the origin. This limits the energy resolution because a larger range of energies fits into the PSF. In the following, this will be called energy resolution. Mathematically, the length of the detector segment that takes the differential energy δE can be formulated as:

$$\delta l_E(E) = \sqrt{(x(E) - x(E+\delta E))^2 + (y(E) - y(E+\delta E))^2} \quad . \tag{2.50}$$

Eventually, at some threshold value of E, δl takes a value larger than the PSF circle, which is the here used definition of the energy resolution.

Figure 2.10 (a) displays the highest energy at which the species separation is satisfied for a reasonable range of electric and magnetic fields in the here used spectrometer. It can be seen that there is an optimal balance between U and B in terms of species resolution on the diagonal ($E/B \approx 0.5\,\mathrm{V\,mT^{-1}\,mm^{-1}}$).

Using a threshold of

$$\delta E/E \leq 0.1 \quad , \tag{2.51}$$

a similar graph can be computed for the energy resolution. The results are shown in Figure 2.10 (b). Here, the behavior is different, as arrows disperse from the lower left corner in an almost radial pattern. This means that it is more effective to further increase the dominant field compared to the balanced case of $E/B \approx 0.5\,\mathrm{V\,mT^{-1}\,mm^{-1}}$ if the species resolution is already suffi-

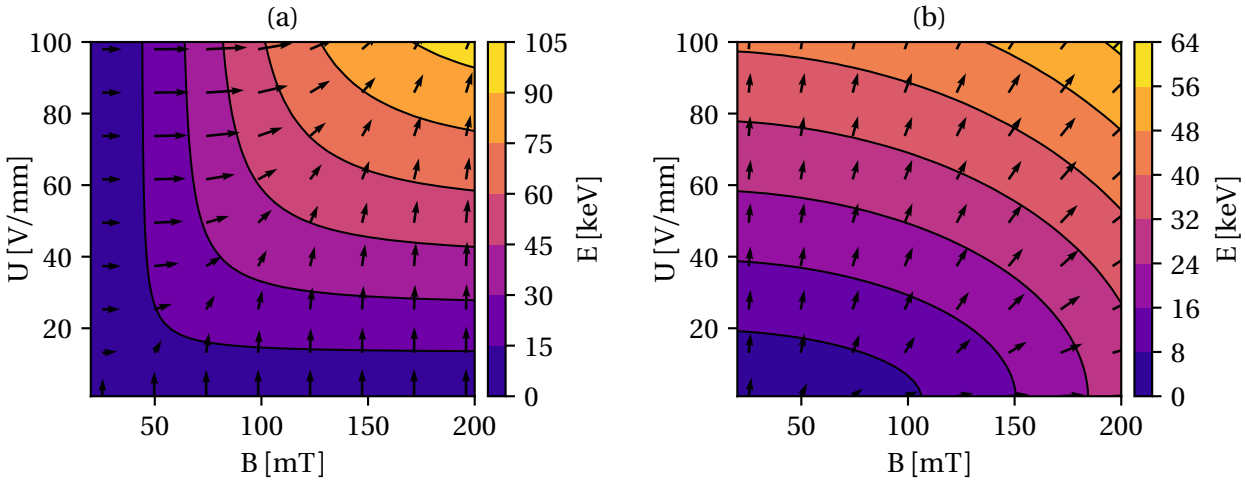

Figure 2.10: (a) Highest resolvable kinetic energy until the parabolas of neighboring ion species merge for different spectrometer settings. (b) Highest resolvable kinetic energy until the energy resolution hits an uncertainty of 0.1 .

cient. Note that neither (a) nor (b) depend on the free flight distance s, since both the length of the lines (Figure 2.9) and the PSF diameter scale linearly with s.

Following a path at which U/B^2 is constant allows for a comparison of how the ion charge q plays in the uncertainty. In Figure 2.11 (a), it is shown that the energy uncertainty is largest for the smallest charge to mass ratio. Note that the dashed and solid lines represent the upper and lower side of E, because strictly speaking, the values of δl_E depend on the sign of δE (solid line: $\delta E > 0$, dashed line $\delta E < 0$). Also, note the black lines are the errors introduced by the uncertainty of the free-flight path s. This error is unaffected by the charge.

Figure 2.11 (b) shows how the error at 15 keV decreases if U and B are raised. At high fields, the error decreases only slowly until, at some point, the free-flight error is dominant (black line). Usually, however, this error is smaller than the PSF one, and will hence be omitted from here onward.

2.4.2 Choice of detector

Next, the options for the type of detector are discussed. Some popular options are: MCP, **f**lourescent **l**ayers (FL), **C**olumbia **R**esin 39 (CR-39) plates, **i**mage **p**lates (IP), and semiconductor based ones, such as **c**harge **c**oupled **d**evice (CCD)s. To form a decision, some criteria should be set up first, in accordance with the operating principles described previously.

(i) The detector should be large in size, when compared to the projection of the used aperture.

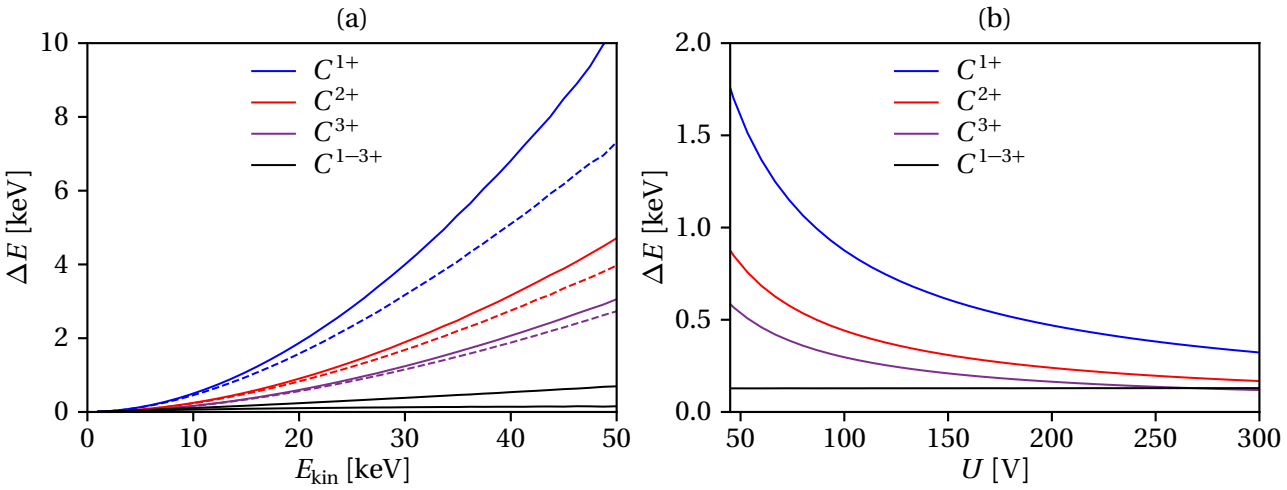

Figure 2.11: (a) Calculated energy uncertainties caused by the pinhole (colored lines) and the free-flight distance (black lines). The solid lines show the upper (ΔE_+), and the dashed ones the lower uncertainty (ΔE_-) due to the nonlinear mapping of the TPS. (b) Average pinhole error ($(\Delta E_+ + \Delta E_-)/2$) for different spectrometer settings at a particle energy of 15 keV (colored lines for the pinhole and black line for the free-flight error). The settings were chosen such that U/I^2 is constant, with U being the voltage applied to the electrodes.

detector	(i)	(ii)	(iii)	(iv)	(v)
MCP	☆	☆	☆	☆	☆
IP	☆	☆	☆	☆	(☆)
CR39	☆	☆	☆		
CCD	(☆)	☆	☆	☆	☆
FL	☆	☆	☆	☆	

Table 2.1: Comparison of a selection of detector types in terms of suitability for TPS keV ion detection, according to the five set criteria defined above. A "☆" means the criterion is met, an empty slot means it is not, and a "(☆)" means further discussion is necessary.

(ii) A sufficient resolution of at least some pixel per diameter of stated projection is required.

(iii) It must scale linearly with the incident fluence, or the scaling must be known.

(iv) Ion and X-ray sensitivity must be given.

(v) Somewhat intuitive usage.

Because 1. and 2. depend on the geometry of the setup, an arbitrary size of at least 1 cm^2, and a similar arbitrary resolution of 100 µm is defined. Overviewing these criteria in table 2.1, shows three possible choices, which will be discussed in more detail.

While CCDs are available in sizes large enough, these are rather rare, as the majority tends to be

small. Custom solutions to this problem create an empty space at point (iv), which renders the CCD inferior compared to the other five star options. Due to these reasons, the measurements were carried out using IPs and MCPs.

Image plates

The available IPs are made by Fujifilm. They are of the BAS-TR2040 type, which does not have a protective layer. This is important because keV-ions, with their penetration depth of $\sim 0.1\,\mu m$, are not able to penetrate protective layers [99]. Instead, these plates consist of approximately 0.5 mm thick plastic foils, only coated with a 150 µm active layer of BaFBr:Eu^{2+} crystals [100].
If energy is incident, meta-stable states are populated in the active layer. Exposing them to red light, excites them to higher-lying states and leads to emission of blue light. The readout device made by the same company, scans the plates with a tightly focused **H**elium **N**eon (He:Ne). The blue light emitted from this small focus is captured simultaneously. Because the captured blue light is logarithmically amplified in the scanner to what is called the **q**uantum **l**evel (QL), the signal is converted to the linear **p**hoto-**s**timulated **l**uminescence (PSL) [101]

$$PSL = \left(\frac{R}{100}\right)^2 \cdot \frac{4000}{S} \cdot 10^{L\left(\frac{QL}{2^G-1}-\frac{1}{2}\right)} \tag{2.52}$$

scale, according to the scanner specific parameters G, S, R, L [102]. For the scanner used in this work, the bit depth is $G = 16$, the sensitivity is $S = 4000$, the resolution is $R = 50\,\mu m$, and the latitude parameter is $L = 5$. This equation is used to rescale the signal such that it is proportional to the deposited dosage on the IP.
The meta-stable states also decay on their own on 30 min time scales, which can be corrected for according to the PSL_{30} convention [101]

$$PSL_{30} = \left(\frac{30}{t}\right)^{-0.161} PSL(t) \quad , \tag{2.53}$$

where t is the time until readout in minutes. Note that the exponent varies between different works [103]. This conversion takes the time t from exposure of the IP to the scanning process, and gives out the signal strength as it would be 30 min after exposure.
Due to this fading, the time it takes to accumulate the ion signal on the detector must be kept short compared to the time from the accumulation to the readout. Otherwise, early exposure during the measurement contributes less to the total signal than later one.
In tests, a number of 800 accumulated events turned out to be an appropriate compromise between signal strength and duration of the measurement. At a repetition rate of 6 Hz, the measurement takes about 2 min. On a single IP, up to 12 individual measurements are taken. Thus,

the largest time difference Δt between measurements is about 24 min. A comparison between the signal strength of the first and last measurement

$$\frac{PSL_t}{PSL_{t+\Delta t}} = \left(1 + \frac{t}{\Delta t}\right)^{-0.161} \quad , \tag{2.54}$$

demonstrates that the relative difference becomes smaller with larger t. Therefore, to reduce possible errors, as neither the exponent is known for the exact case, nor the precision of t exceeds 2 min, some time should be let pass before the readout. At $t = 10$ min, the deviation becomes less than 20 %.

In our measurements no significant fading was found. This indicates that the absolute value of the exponent might be smaller than 0.161 in this work's use case. One possible reason is that the amount of stray light incident on the IP was kept as low as possible during and after exposure, which includes any sources of light in the laboratory. Thus, as long as t exceeds 10 min, the fading is assumed negligible.

IPs are not the most convenient detector type since they require frequent breaking of the vacuum, but they excel in dynamic range. An advantage of IPs is, that they are only limited in size by the scanning device, which supports up to $250 \times 225\,\mathrm{mm}^2$. Another advantage is that the PSL signal is standardized and thus can be directly compared between different works. Once a calibration exists, it can be used for other setups as well. While they are a proven tool for fast ions, at the time of writing, the data on IP signals of keV ions is scarce, including data on saturation behavior.

Saturation can occur when an incident ion tries to excite a meta-stable state in a volume of the IP where the degree of meta-stable is already high. For example, by striking an already densely populated area, or if deposits too much energy per penetration depth [104, 103].

Generally, the response of a detector to incident dosage ρ per area $\mathrm{d}A$ can be expressed by eq. (2.55).

$$\frac{\mathrm{d}PSL}{\mathrm{d}A} = \left(\frac{\rho}{a}\right)^b \tag{2.55}$$

Here, a is a factor including the detection efficiency, which might depend on the particle energy, and b is the non-linearity. This factor might also depend on the the particle energy. In the case of a linear detector, b is always 1 across the whole spectrum and employed ρ-range. Usually, the calibration is done using a known spectrum or by counting single particle events.

Given a well characterized TPS and reproducible ion spectra, ρ can be varied across the spectrum to find the exponent response function eq. (2.55). The key part is that, ρ can be varied not only by the number of incident particles at a single event, but also by accumulation over multiple N events, or by stretching the parabola $\mathrm{d}E/\mathrm{d}r$ along its length. Since in a TPS the width of

the parabola is given by the constant aperture, the area $\mathrm{d}A = \mathrm{d}r_l\,\mathrm{d}r_t$ can be split in a constant transversal part $\mathrm{d}r_t$ and a setting dependent longitudinal part $\mathrm{d}r_l \equiv \mathrm{d}r$.
Equation (2.55) allows us to compare two spectra, which were captured at different energy densities ρ and ρ'

$$\frac{\mathrm{d}PSL'}{\mathrm{d}r} = \frac{\mathrm{d}PSL}{\mathrm{d}r}\left[\frac{\rho'}{\rho}\right]^b \quad . \tag{2.56}$$

Now substituting N and $\mathrm{d}E/\mathrm{d}r$ into this equation, yields

$$\frac{\mathrm{d}PSL'}{\mathrm{d}r} = \frac{\mathrm{d}PSL}{\mathrm{d}r}\left[\frac{N'}{N}\left(\frac{\mathrm{d}E}{\mathrm{d}r}\right)'\left(\frac{\mathrm{d}r}{\mathrm{d}E}\right)\right]^b \quad . \tag{2.57}$$

Since both N and $\mathrm{d}E/\mathrm{d}r$ are known, as well as the signal strength of the detector, b can be concluded. This is easiest if the ln is taken on both sides, which results in a linear function with the slope b.
In Figure 2.12 (a), various points across the spectrum of an IP measurement are compared at a different number of accumulations N. Averaging over all points that were taken into account yields $b = 1$. Part (b) shows the result for the exponent b, resolved by the colors from (a), which represent the different energies. Overall, a fairly consistent value of 1 is retrieved. Note that, below 7 keV, the signal on the IP is low, which causes the drop in b, as the spectra merge with noise. A reason for this might be a beginning cutoff for low carbon energies. Above 20 keV, a similar issue appears where the signal is low. This causes b to consistently take values above one, due to errors in the readout process.
However, the measurements show that the signal chain behaves linearly. Usually, the scanner clips due to its digital limits before the IP starts to saturate, which was not the case even for 1200 exposures. This makes IPs well suited detectors for the purpose of keV ion detection, with an excellent signal to noise ratio, because very low energy particles are not detected.

Micro channel plates

The scaling of MCPs, which is strictly speaking a combination of an MCP with a phosphorus screen and camera, might depend on the settings. Non-linearity might occur if the incident dosage is so large that a large number of freed electrons in the multiplier tube causes a collapse of the amplifying electric field within the tube, or over-saturates the phosphor screen due to quenching. Therefore, the response in the specific use-case must be verified for coherent results, which is especially important here, as the ions are bunched on $\sim\mu$s time scales when they arrive at the detector [105, 106]. Here, a response of the measured signal S similar to the PSL

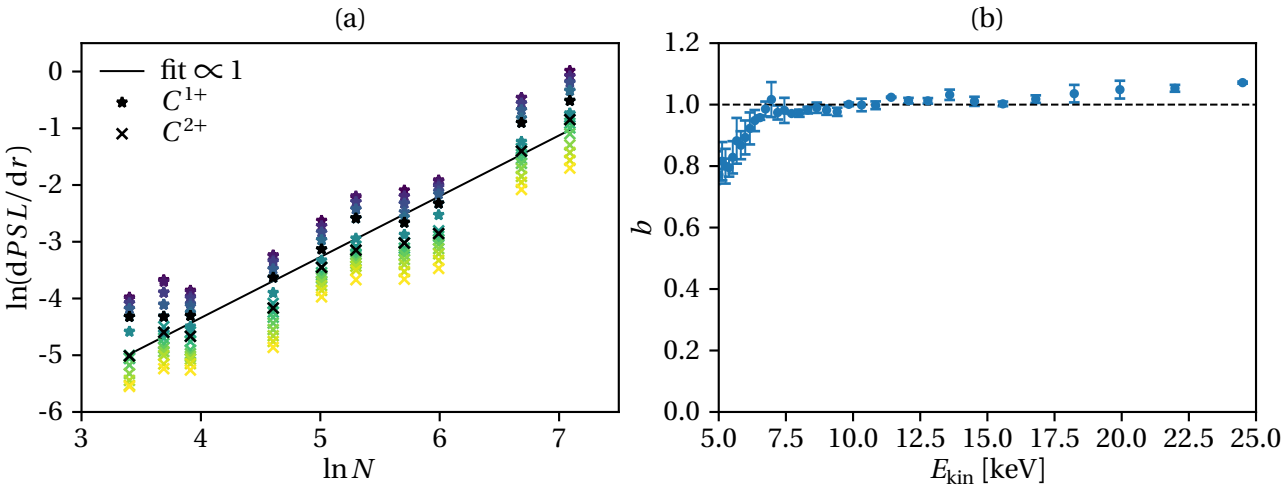

Figure 2.12: (a) Signal strength PSL in dependence of the number N of exposures for several sections of the spectrum (different colors) in terms of C^{1+} (stars) and C^{2+} (crosses). (b) Nonlinear exponent b across the spectrum.

from before is assumed

$$\frac{\mathrm{d}S}{\mathrm{d}r} = \left(\frac{\rho}{a}\right)^b \quad . \tag{2.58}$$

The goal is to find a voltage (or gain) setting at which the response of the chain is linear and fully uses the dynamic range of the camera, because this element is known to be linear throughout the digital range.

As MCPs are a "single shot" diagnostic, accumulations on the detector are not possible. In order to sample the linearity, parabolic traces of the same spectrum were stretched to a different extent. The results of this measurement are displayed in Figure 2.13 (a). In part (b), the incline of the fit is resolved by kinetic energy. It becomes apparent that the exponent b stays close to one for lower kinetic energies for the MCP compared to the IP. This graph was truncated at 3 keV because lower energies are partly not observable at the higher spectrometer settings, but also begin to overlap with thermal particles.

Note that the pixel values cover about half of the dynamic range of the used camera. Since the MCP was driven at a voltage of 900 V (Gain $\approx 10^4$) instead of the maximum 1200 V (Gain $\approx 10^5$), it has a headroom of about one order of magnitude in terms of gain.

The potential difference between MCP out and phosphor screen was set to 3600 V, out of the maximal allowed 4000 V. A higher value increases the brightness of the phosphor screen, and therefore also on the camera. Because it remains unclear how much dynamic range is available in the phosphor screen, most of the measurements were performed at this tested potential difference of 3600 V.

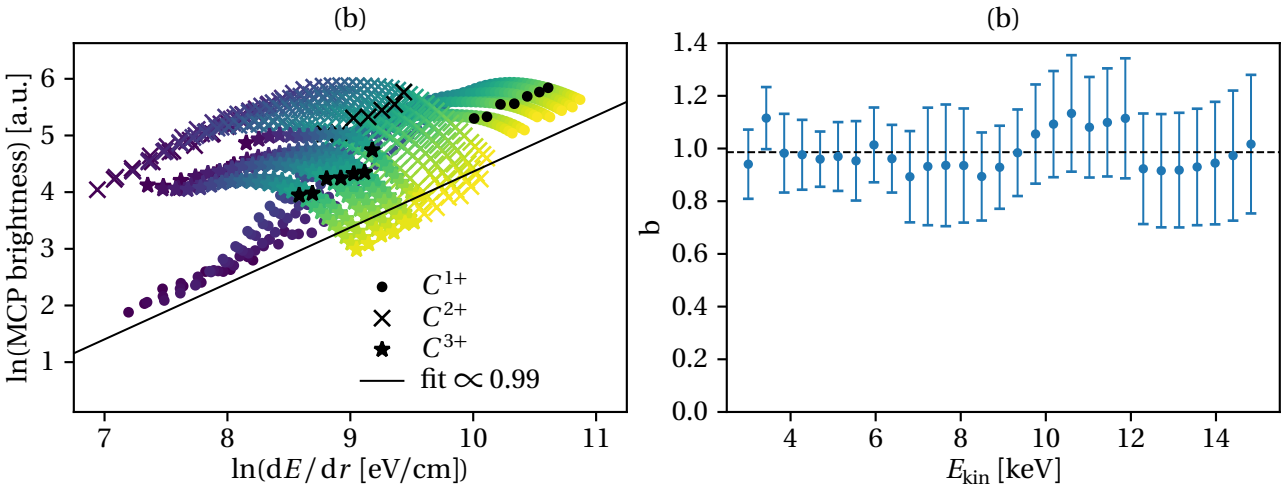

Figure 2.13: (a) Signal strength in terms of pixel value versus the stretch of the parabola for several points across the spectra of C^{1+} (dots), C^{2+} (crosses), and C^{3+} (stars). The data of each marker-shape and color belongs to one fit. To illustrate this, some corresponding data is highlighted in black. The average slope of the fits is shown by the black line. (b) The total non-linearity across the spectrum, as calculated from all three species.

Based on these measurements, linearity of the IP and MCP is assumed over the whole region of interest and full dynamic range of the camera and scanner. Please note that these measurements are not sufficient to calculate the actual number of incident particles. Even though the detection efficiencies for keV ions on MCPs is roughly known [107], the number of ions per pixel value increment is missing. This value is specific to the experimental setup and requires calibration by known radiation or a calibrated method such as nuclear reaction analysis [108].

Chapter 3

Methods and experimental setup

In this chapter, the methods and experimental setup which were used to generate the data sets are discussed. All of the experiments were performed under vacuum conditions from $10^{-4} - 10^{-6}$ mbar, which is sufficiently low to not disturb any particle trajectories and to implement an MCP.

3.1 PHASER Laser

The laser system used in this work is the **P**hase-stabilized **H**eine l**aser** (PHASER), located at the **H**einrich-**H**eine-**U**niversität (HHU) in Düsseldorf, Germany. As the name suggests, the system is able to provide ultra-short CEP stabilized pulses of 5 fs duration and above.
This system can be roughly divided into three parts, as illustrated in Figure 3.1. In the first one, the pulses are created in a titan sapphire oscillator, which is the commercial Rainbow™ by Femto Laser. In the oscillator, the pulse train consists of 5 nJ pulses with a repetition rate of about 75 MHz. These pulses are then amplified to 2 mJ at a reduced rate of 1 kHz in a Femtopower™ amplifier.
The next section is concerned with adjustments in terms of spectrum and repetition rate, such that the conditions in the experiment are optimal. At the beginning of this section, the bandwidth is 40 nm, which yields 25 fs pulses post compression by the grating pair. After that, the pulses enter a neon filled hollow core fiber in which they are spectrally broadened due to self modulation [109, 110]. Depending on the neon pressure (0-1000 mbar), this effect is more or less present, which comes at the cost of varying transmission efficiencies due to ionization losses. The pulse energy is also reduced because of losses that occur during excitation of the correct mode [111]. Post fiber, bandwidths up to 300 nm are possible, with energies up to 1 mJ. Then, a

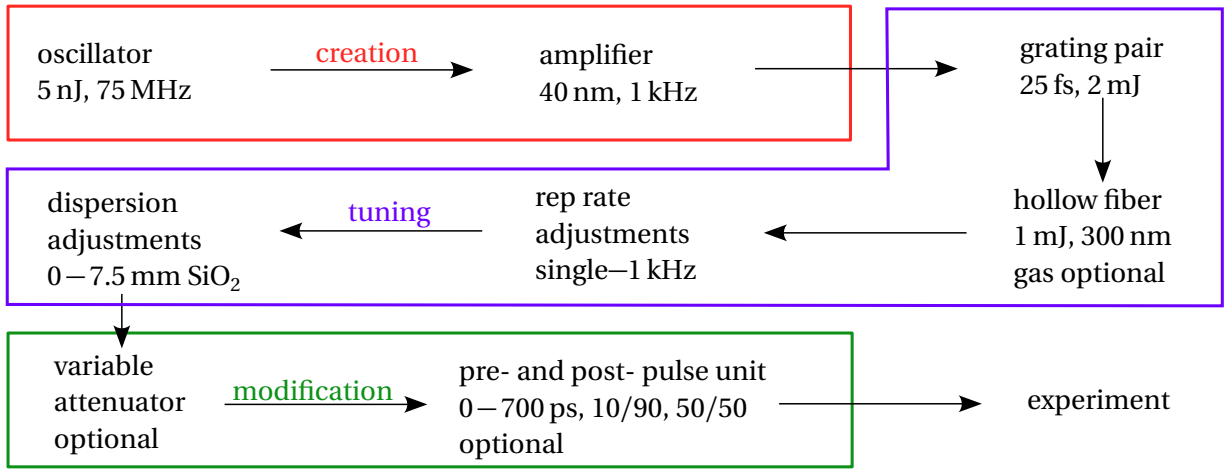

Figure 3.1: Flow chart of the key elements in the laser system PHASER.

reduction of the repetition rate $f_{\text{rep}} = 1/\tau_{\text{rep}}$ is done by an optical chopper wheel and a mechanical shutter.

In the last section, the pulses pass through a variable attenuator [112] and pre- and post pulse unit [113], which are described in further detail in the next section, as they were used for multiple measurements within this work.

After that, the pulses are passed to the experiment and pulse diagnostics, such as the SPIDER[54], to determine their duration. For our measurements, mainly three modes of operation were used: Pulses without gas in the in the fiber, also called amplifier pulses, and 1000 mbar neon in the fiber, either with the attenuator, or with the double-pulse unit.

3.1.1 Contrast

The pulse contrast is an important parameter for the experiments in this work since it defines the target conditions at the arrival of the main pulse, but it is difficult to measure on a day-to-day basis. On time scales longer than a few picoseconds, the contrast is determined by the amounts of self-**a**mplified **s**pontaneous **e**mission (ASE) in the amplifier [114], while picosecond contrast can be attributed to perturbations in the spectral phase. Figure 3.2 (a) shows the performance of the PHASER as measured with a commercially available third order autocorrelator, SEQUOIA™ from Amplitude [115]. A ratio of 10^{-8} is exceeded until the contrast worsens shortly before the main pulse.

The graph in section (b) is the fluence (time accumulated intensity) under the assumption that the ASE of 10^{-8} is present throughout the opening window of the **P**ockels **c**ell (PC) ahead of the

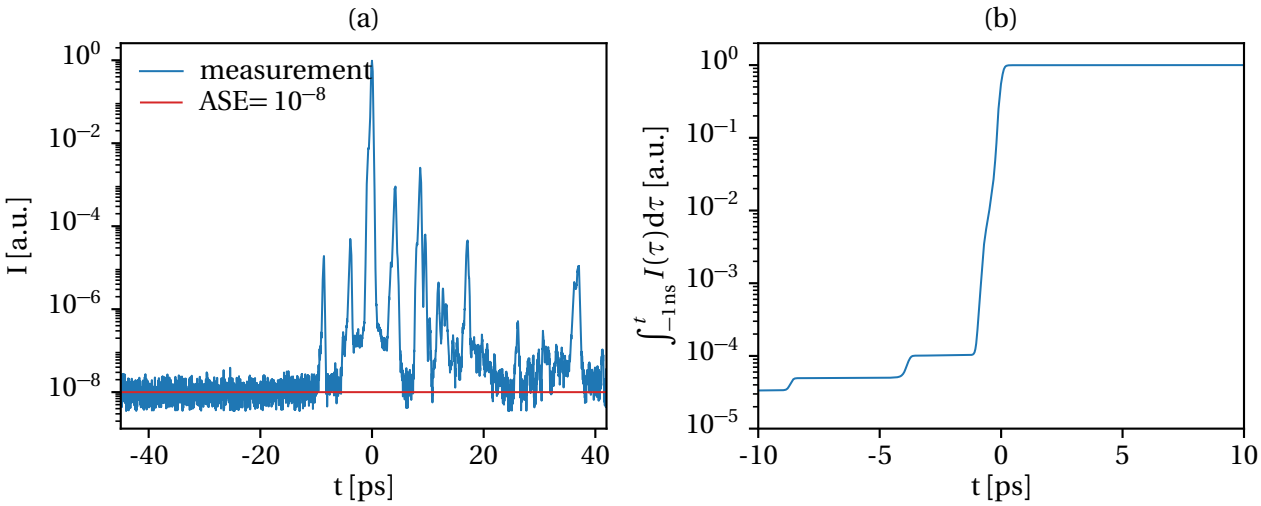

Figure 3.2: (a) The trace of the third-order autocorrelator Sequoia. (b) Normalized time integration of the trace.

pulse center, which is about 1 ns.

$$J_{acc}(t) = \int_{-1\,ns}^{t} I(\tau)\, d\tau \tag{3.1}$$

This is a worst case approximation, since the pulse is temporally located shortly after the opening flank of the PC. In this case, 10^{-4} of the pulse energy illuminates the target before the main pulse strikes. Depending on the pulse energy and focal position, this can cause the ignition of a pre-plasma. When exactly the pre-plasma is formed depends on the target material and spot size.

One simple way to check if a plasma is present at a certain time is to compare the material specific **l**aser **i**nduced **d**amage **t**hreshold (LIDT) to the fluence deposited by the laser. If the deposition is sufficiently rapid, the particles undergo a solid-plasma transition, skipping the molten phase. Table 3.1 lists the used target materials and their damage threshold, as well as the time when the LIDT is exceeded.

It is important to note, that the LIDT usually decreases with shorter durations. Below about 100 ps, the threshold fluence approaches a constant value [116]. Thus, it is important to distinguish between fs, ps, and ns LIDTs.

Another factor which affects the exact threshold is the laser wavelength. In terms of gold, the range of tabulated wavelengths from 790 nm to 1030 nm change the threshold by less than a factor of two [116]. Even though the found literature was taken using different lasers, the LIDT is assumed to sufficiently resemble the 800 nm LIDT values.

The procedure to determine the LIDT, often used in literature, is by monitoring the depth of a

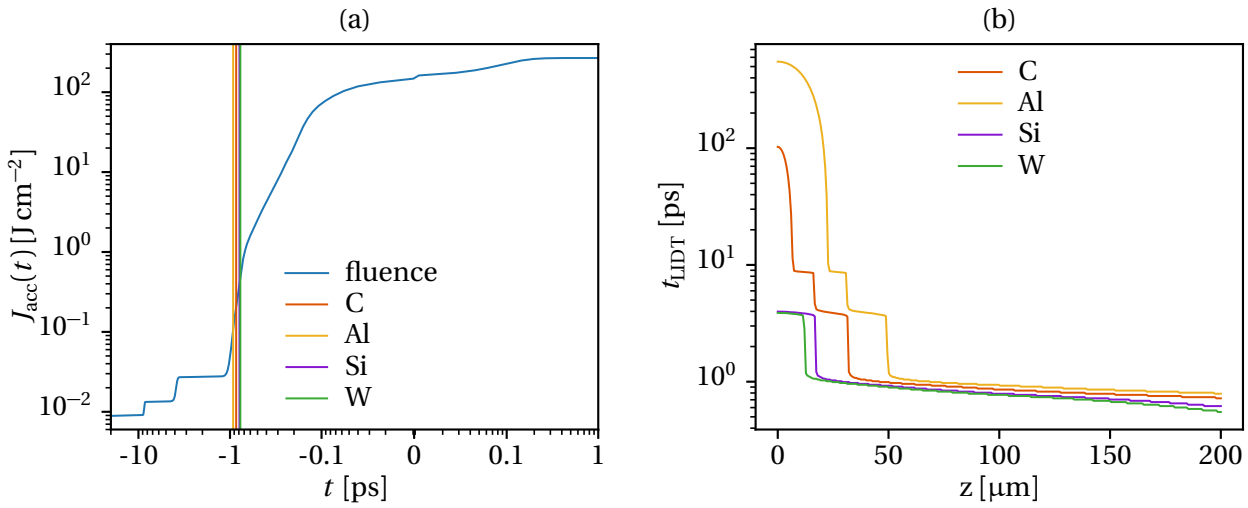

Figure 3.3: (a): accumulation of the laser pulse fluence at a defocused position ($z = 100\,\mu$m). The peak fluence J_{max} in this position is about 130 J cm^{-2}. The vertical lines show when the damage threshold of some selected materials is reached. (b) Times t_{LIDT} at which the fluence exceeds the LIDT for different focal positions.

crater a laser pulse leaves on the target against the applied fluence. A fit is then used to find the fluence at which zero crater depth is generated. One caveat with this procedure is that the found LIDT depends on the fluences used for the fit. High fluences ($\gtrsim 10\,\mathrm{J\,cm^{-2}}$) lead to higher LIDT than low fluence ($\lesssim 1\,\mathrm{J\,cm^{-2}}$) [117]. To make things even more complicated, in addition to the LIDT, which has the unit of a fluence, there is also an intensity threshold on the order of $10^{12}\,\mathrm{W\,cm^{-2}}$ [118]. To give a final disclaimer, often the surface conditions, like roughness or contaminants, are unknown during these experiments. Especially, a high surface roughness creates nontrivial results because it increases the surface and randomizes the incident angle [119].
When the LIDT is surpassed depends on the focal position, laser contrast, and how the fluence is defined. In the calculations presented here, the maximal accumulated fluence J_{max} is defined as

$$J_{max} = J_{acc}(\infty) \tag{3.2}$$

$$= \int_{-1\,\mathrm{ns}}^{\infty}\int_{0}^{\infty} 2\pi r I(\tau)\exp\left(-2\left(\frac{r}{w(z)}\right)^2\right)\mathrm{d}\tau\,\mathrm{d}r \tag{3.3}$$

$$= \frac{2E_{max}}{\pi w(z)^2} \quad . \tag{3.4}$$

material	LIDT
glassy carbon	$\sim 0.2\,\mathrm{J\,cm^{-2}}$ (790 nm) [120] (fs-LIDT) $\sim 0.2\,\mathrm{J\,cm^{-2}}$ (800 nm) [121] (ps-LIDT) $\sim 0.2\,\mathrm{J\,cm^{-2}}$ (532 nm) [122] (ns-LIDT)
aluminum	$\sim 0.1\,\mathrm{J\,cm^{-2}}$ (800 nm) [123, 124] (fs-LIDT) $\sim 1\,\mathrm{J\,cm^{-2}}$ (1064 nm) [125] (ns-LIDT)
silicon	$\sim 0.4\,\mathrm{J\,cm^{-2}}$ (1030 nm) [117] (fs-LIDT) $\sim 1\,\mathrm{J\,cm^{-2}}$ (1030 nm) [126] (ps-LIDT) $\sim 3\,\mathrm{J\,cm^{-2}}$ (1064 nm) [127] (ns-LIDT)
tungsten	$\sim 0.5\,\mathrm{J\,cm^{-2}}$ (800 nm) [108, 124] (fs-LIDT) $\sim 1\,\mathrm{J\,cm^{-2}}$ (355 nm) [128] (ps-LIDT) $\sim 10\,\mathrm{J\,cm^{-2}}$ (1064 nm) [129] (ns-LIDT)

Table 3.1: Laser induced damage threshold (LIDT) of some materials. As glassy carbon consists of irregularly packed and curved graphene sheets, its LIDT value was approximated by the one of graphene. Note that the cited work investigated a differently cut crystal structure of silicon (001) than the one used as target material (111).

Since the accumulated pulse energy E_{max} can be deduced from the average power and the laser repetition rate, J_{max} was approximated as shown in eq. (3.4). Figure 3.3 (a) shows the previous third order **a**uto-**c**orrelator (AK3) trace with better resolution along the time axis, normalized to the peak fluence J_{max} reached at a defocused position of $z = 100\,\mu\mathrm{m}$. This value of z was used in experiments, of which the results are presented later. It should be stated that this metric might differ from the one that was used to deduce the literature values of the LIDTs, as the exact procedure and/or beam profile in combination with a pulse contrast measurement is often not disclosed. The vertical lines show when the damage threshold of the tabulated materials from Table 3.1 is reached. For this Figure, the fs-LIDT was used for the following reason. In Figure 3.3 (a), the threshold is reached in a steep part of the graph, besides the fs-fluence being the lowest tabulated values. This means that most of the fluence is deposited within a short time period of less than a picosecond. Therefore, the fs-LIDT is best suited to approximate the time of the solid-plasma transition at a given z-position.

Figure 3.3 (b) shows the times at which the fluence exceeds the LIDT (t_{LIDT}) for different focal positions. For small z, the ignition curve shows steps, each of which corresponds to a pre-pulse peak in the AK3 signal (Figure 3.2). According to this calculation, carbon and aluminum ignite at about $\sim 100\,\mathrm{ps}$ before the pulse peak when the target is perfectly in focus. However, note that times $t_{\mathrm{LIDT}} > 10\,\mathrm{ps}$ should be viewed with caution, because the fs-LIDT was used instead of

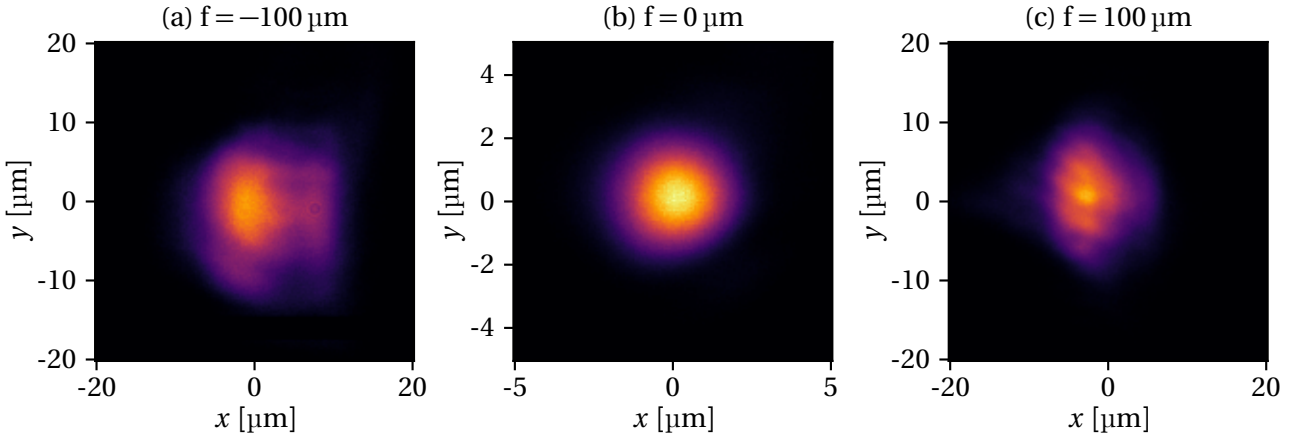

Figure 3.4: Magnified ($V = 33.3$) image of single pulse beam profiles taken (a) 100 µm behind the beam waist (intermediate focus), (b) in the beam waist, and (c) 100 µm in front of the beam waist (towards the parabola). The blue halos in the ±100 µm positions are caused by clipping of beam with microscope aperture.

the ns-LIDT. While on ns-time-scales, the target is heated until it is unable to sustain its shape, fs pulses cause damage by strong fields ($I \sim 10^{12}\,\mathrm{W\,cm^{-2}}$), which lead to ionization effects as discussed in Figure 2.5. While the ns-LIDT is higher than the fs-LIDT and more appropriate to apply to the ASE, the literature values lay in a fairly tight range for glassy carbon and aluminum. In contrast, silicon and tungsten hold up until about 4 ps, which is when the second spike and the elevated pedestal appear in the AK3 trace. For $z > 50$ µm, t_{LIDT} has moved to about 1 ps which can be considered an early part of the rising pulse flank, according to Figure 3.2 (a). From there on, the z position can be used to tune the exact timing down to a point where the final fluence is below the LIDT ($z \gtrsim 3000$ µm). However, for reasonable values of z, the solid-plasma transition is expected to occur between some hundreds of femtoseconds to a picosecond before the pulse peak.

3.1.2 Focal spot

For the fluence, as well as intensity, the beam profile on target plays an important role. The laser is focused by a 3"-diameter, 90° deflection angle off-axis parabola, with an effective focal length of 127 mm. Pre-parabola, the Gaussian width is 14 mm, which results in a theoretical beam waist of $w_0 = 2.28$ µm and a Rayleigh length of $z_R = 20.65$ µm. The focal plane is imaged with a magnification of $V = 33.3$ onto the Imaging Source DMK37BUX226 [130], with a pixel size of 1.85 µm, by an objective of a microscope. Figure 3.4 shows a series of magnified images of

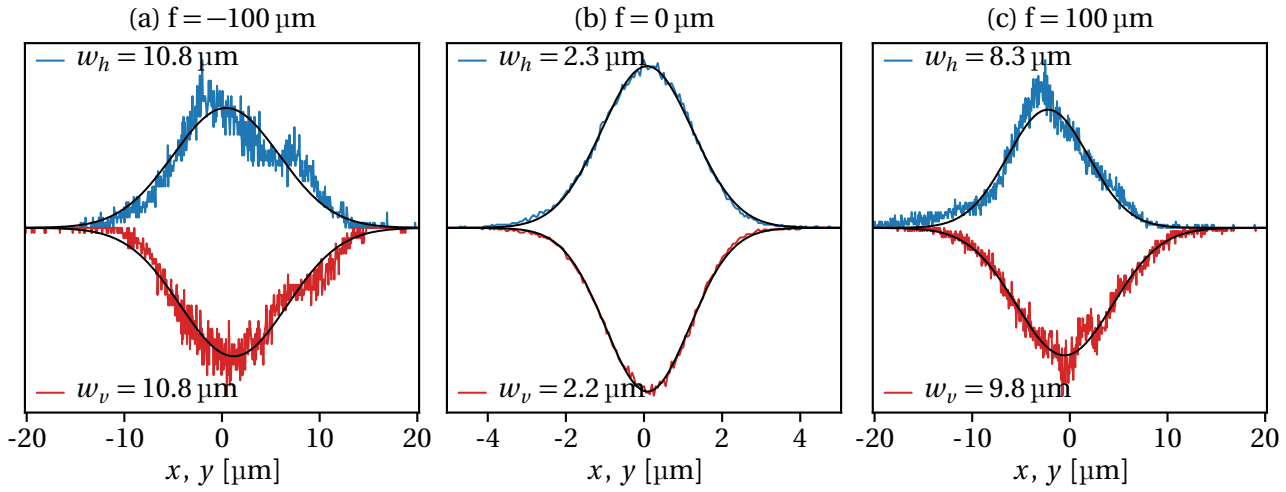

Figure 3.5: Horizontal (blue) and vertical (red) lineouts taken from the magnified (V=33.3) image of single pulse beam profiles and fits (black). (a) 100 µm behind the beam waist (intermediate focus), (b) in the beam waist, and (c) 100 µm in front of the beam waist (towards the parabola).

the beam in 100 µm steps. Note, that the absolute position of the best focus is only accurate to ±10 µm. The 100 µm interval corresponds to roughly five Rayleigh lengths. The shape remains Gaussian-like throughout. This is a key attribute of the PHASER due to its hollow fiber, which acts as a long spatial filter. In Figure 3.5, horizontal and vertical lineouts, including a Gaussian fit, are presented. The theoretical limit of $w_0 = 2.28\,\mu m$ is met, and $z_R \approx 20\,\mu m$ is confirmed as the radius increases roughly by a factor of five. Thus, a Gaussian profile is assumed also at the defocused position.

3.1.3 Variable attenuator

The energy contained in the beam profile can be adjusted in the **v**ariable **a**ttenuator (VA), as set up by Wegner [112]. This device consists of a set of four exchangeable mirrors with different reflectivities due to a varying gold thickness coated onto **f**used **s**ilica (FS) substrates. This way, the pulse energy can be lowered by more than six orders of magnitude, while keeping the dispersion unaffected. Its integration in the laser system is schematically drawn in Figure 3.6 (a), together with a sketch of a segmented mirror. The reflectivities of each mirror are listed in table 3.2. They span a range of 0.94 for a solid gold surface and 0.009 for the bare fused FS.

	M1	M2	M3	M4
S1	0.94	0.94	0.94	0.94
S2	0.51	0.59	0.67	0.47
S3	0.37	0.45	0.26	0.25
S4	0.24	0.0090	0.0090	0.0090

Table 3.2: Reflectivities of the different mirrors M1-M4, and their segments S1-S4 as listed in [112].

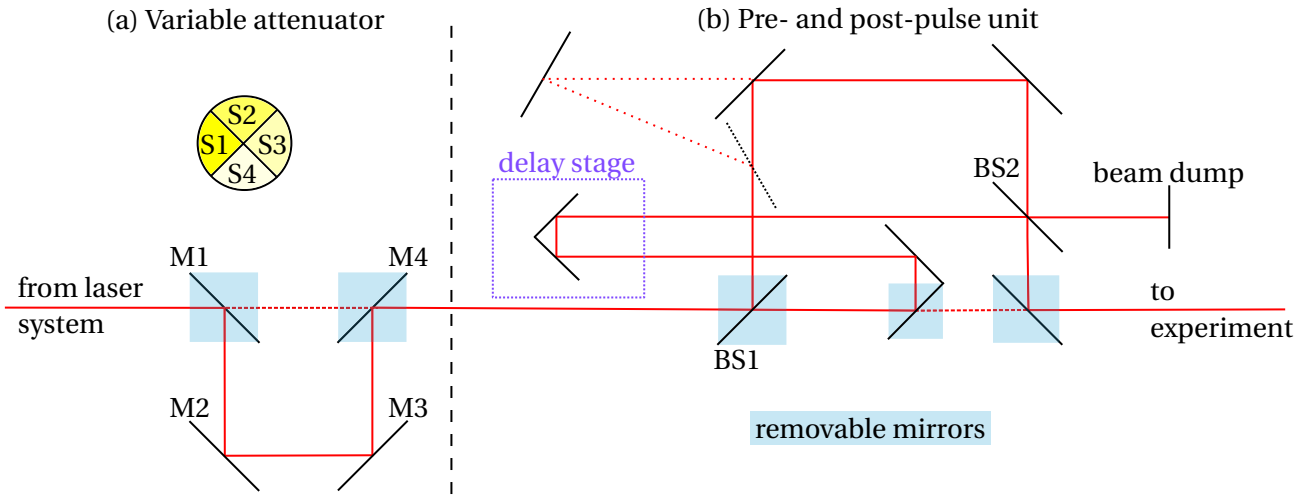

Figure 3.6: Schematic drawing of the variable attenuator (a) and pre-(post-)pulse unit (dotted line) (b). Both devices can be individually removed by taking out the removable mirrors. In this case, the laser takes the direct path (dashed lines).

3.1.4 Pre- and post-pulse unit

Figure 3.6 (b) shows that after the attenuator comes the pre- and post-pulse unit, which is an extended version of the initial pre-pulse device set up by Mittelmann [113]. This device creates an identical pulse pair in a Mach-Zehnder-like setup.

The upper arm has two possible beam paths, which change the sequence of the pulses. Thus, a pre-pulse from the solid path can become a post-pulse by using the dotted path. The beam splitters in the setup (BS1, BS2) are exchangeable to either a 50/50 or a 10/90 transmission/reflection configuration. The former configuration yields a pulse pair with 25/25 percent intensities of the ingoing pulse, while the latter one creates a 01/81 percent one. Note that the creation of the duplicates reduces the total pulse energy because one exit of the interferometer is dumped. Sometimes, the notation refers to the distribution normalized to the total throughput (sum of the pulse energies). In this notation, 25/25 becomes 50/50, and 01/81 becomes $\approx$ 01/99. The linear translation stage in one arm of the interferometer allows for time delays between zero and

700 ps.
The initial time overlap is found in a spectrometer, where the collinear propagating pulses create fringes in a spectrum. From the fringe-to-fringe distance, the temporal shift can be calculated. This way, the temporal overlap is found with an accuracy of about 1 pulse length $\sim 1\,\mu\text{m} \sim 5\,\text{fs}$.

3.2 Spectrometer

3.2.1 Electromagnetic Thomson parabola spectrometer

Creating a variable magnetic field for the vacuum environment is an involved process, which has been tackled by multiple groups [33, 34]. They involve, for example, movable yoke or magnet configurations [32]. This way, the cooling required by electromagnets is circumvented. But, since electromagnets possibly offer a larger tunability of the field, and moving parts in vacuum introduce difficulties on their own, this was the method of choice for this work.
In an electromagnet with a yoke and a small yoke gap of width l_{vac}, the magnetic field B can be estimated to good proximity [131, 12]

$$B = \frac{NI}{R_{\text{m}}A} \qquad \Big| \quad R_m = R_{\text{yoke}} + R_{\text{vac}} = \frac{l_{\text{vac}}}{\eta\mu_0 A} \tag{3.5}$$

$$= \eta\mu_0 \frac{NI}{l_{\text{vac}}} \qquad \Big| \quad N = \frac{\xi l h}{\pi r_{\text{wire}}^2}, \quad I = J\pi r_{\text{wire}}^2 \tag{3.6}$$

$$= \xi\eta\mu_0 \frac{l}{l_{\text{vac}}} h J \quad , \tag{3.7}$$

with the number of windings N, wire current I, reluctance R_m, and yoke cross section A. A visual representation of the made approximations is shown in Figure 3.7. Here, ξ is the packing fraction, and $\eta = 1/[1 + l_{\text{yoke}}\mu_0/(l_{\text{vac}}\mu_{\text{yoke}})]$ is the yoke's efficiency. The packing fraction $0 < \xi < 1$ describes how densely the wire can be wound into the coil. A value of $\xi = 1$ means there are voids between the wires. Since the wires are usually round, and have an isolation coating, they cannot be stacked without gaps. Therefore, the canonical packing fraction $\xi = 0.5$ is assumed [131]. l_{vac} is the gap width of the yoke, l_{yoke} is the length of the yoke itself, and μ_0 and μ_{yoke} are the permeabilities of the vacuum and yoke, respectively. J is the current density through the wire, and lh is the gross coil area with the coil length l and height h, where h is proportional to the number of stacked layers.

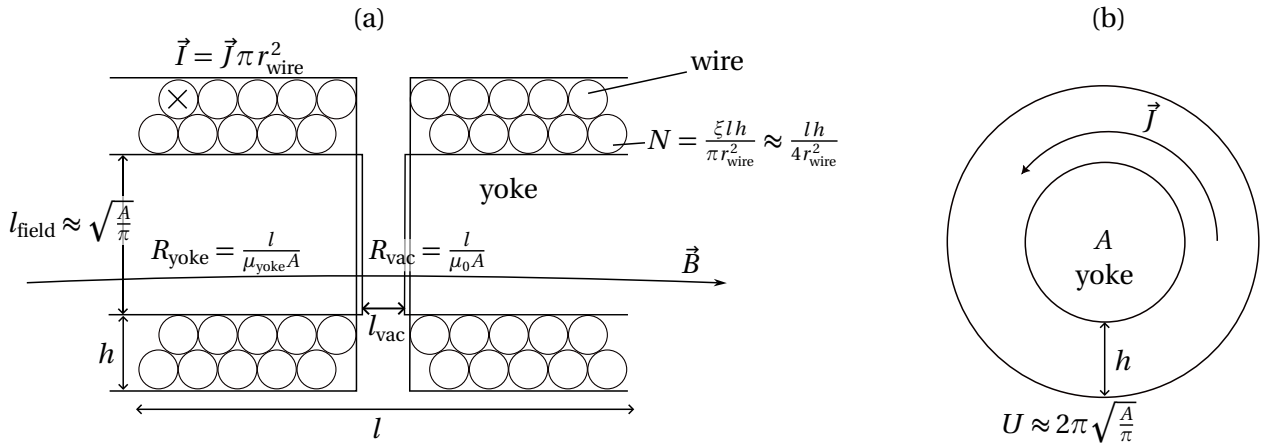

Figure 3.7: (a) Vertical and (b) horizontal cross sections of the TPS magnet shown in Figure 3.8.

With eq. (3.7), the deflection angle

$$\phi_B = \frac{q B l_{\text{field}}}{m v} \qquad \Big| \quad B = \xi \eta \mu_0 \frac{l}{l_{\text{vac}}} h J, \quad l_{\text{field}} \approx \sqrt{\frac{A}{\pi}} \tag{3.8}$$

$$= \frac{\xi \eta \mu_0}{\sqrt{\pi}} \frac{q}{m v} \frac{l}{l_{\text{vac}}} h J \sqrt{A} \quad , \tag{3.9}$$

can be expressed. Here, A is the area of the yoke cross section, which is also the area of the capacitor plates. Because the effective field length depends on the trajectory of the particle through the spectrometer, l_{field} was approximated conservatively by $l_{\text{field}} \approx \sqrt{A/\pi}$. Using the Stefan-Boltzmann law $P = \sigma O (T - T_{\text{ambient}})^4$, the temperature

$$T^4 = \frac{P}{\sigma O} + T_{\text{ambient}}^4 \qquad \Big| \quad P = R I^2, \quad R = \rho_{\text{wire}} \frac{l_{\text{wire}}}{\pi r_{\text{wire}}^2} \tag{3.10}$$

$$= \frac{\rho_{\text{wire}} l_{\text{wire}} I^2}{\sigma O \pi r_{\text{wire}}^2} + T_{\text{ambient}}^4 \qquad \Big| \quad I = J \pi r_{\text{wire}}^2, \quad O = 2\pi \sqrt{\frac{A}{\pi}} l \tag{3.11}$$

$$= \frac{\rho_{\text{wire}} l_{\text{wire}} J^2 r_{\text{wire}}^2}{\sigma 2\sqrt{A/\pi} l} + T_{\text{ambient}}^4 \qquad \Big| \quad l_{\text{wire}} = 2\pi \sqrt{\frac{A}{\pi}} N, \quad N \approx \frac{l h}{4 r_{\text{wire}}^2} \tag{3.12}$$

$$= \frac{\pi \rho_{\text{wire}}(T)}{4\sigma} h J^2 + T_{\text{ambient}}^4 \quad , \tag{3.13}$$

can be deduced assuming a linear temperature dependence of the wire resistivity $\rho_{\text{wire}}(T)$

$$\rho_{\text{wire}}(T) = \rho_{\text{ambient}}(1 + k T) \quad , \tag{3.14}$$

and power loss only due to black-body radiation. O is the radiating surface, and σ is the Stefan-Boltzmann constant. From these equations, the most important design cues can be derived. Because the temperature of the coils does not scale at all with the length l, the yoke should be

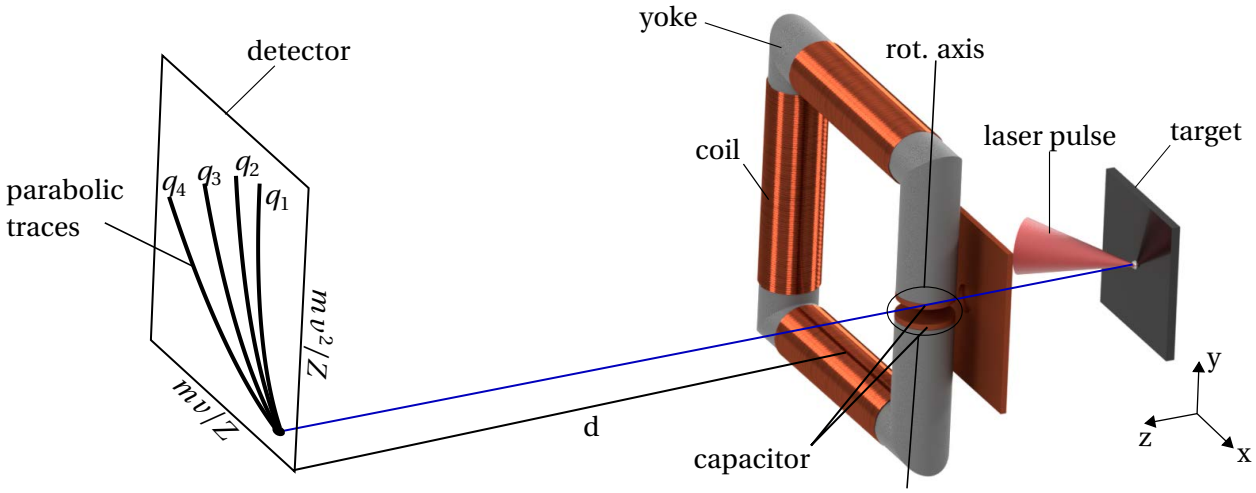

Figure 3.8: Semi-photorealistic sketch of the developed TPS setup in detail. A laser pulse (red cone) illuminates the target and drives ion emission. These ions pass through a 200 µm pinhole before entering the 2 cm long field zone. Here, they are deflected by parallel E- and B-fields (both tunable), according to their kinetic energy, momentum, and charge. By turning the yoke around the rotation axis, it can be aligned more closely with the flight path if more clearance is required. Dimensions of the detector (3 cm by 3 cm) and target to pinhole distance (10 cm) are not drawn true to scale.

kept rather long to reduce the number of layers $\propto h$, and lower the current $\propto J$.

Secondly, for a limited coil length, multiple layers are preferable to a higher drive current due to the scaling of eq. (3.13) with T.

Lastly, the cross section A increases the deflection angle without increasing the temperature, which comes at the expense of compactness.

The spectrometer constructed for this work has a yoke with an approximately $l = 3 \cdot 10$ cm long coil, consisting of three smaller ones in series, as displayed in Figure 3.8.

A wire thickness of 500 µm was chosen, which results in 600 windings per layer, of which two are done in total. Note that the wire thickness itself only matters in terms of the required drive current and voltage, but not performance of any sort. Choosing a thick wire decreases the resistance, resulting in high drive currents and a small operable voltage range. The thickness chosen here gives a total resistance of 7.99 Ω at ambient temperature, and thus operating voltages of 0 to 27 V. Figure 3.9 shows a comparison between the yoke's actual performance and the estimate in terms of the magnetic field (a), as well as temperature (b). In the calculation, a permeability of $\mu_{\text{yoke}} \approx 1000\mu_0$ was used. At currents exceeding 1 A, the electromagnet starts to suffer from saturation behavior. One cause of this might be the square corners obstructing the field lines. Below a current of 1.5 A, the drive current is applied continuously, but above that, only short bursts

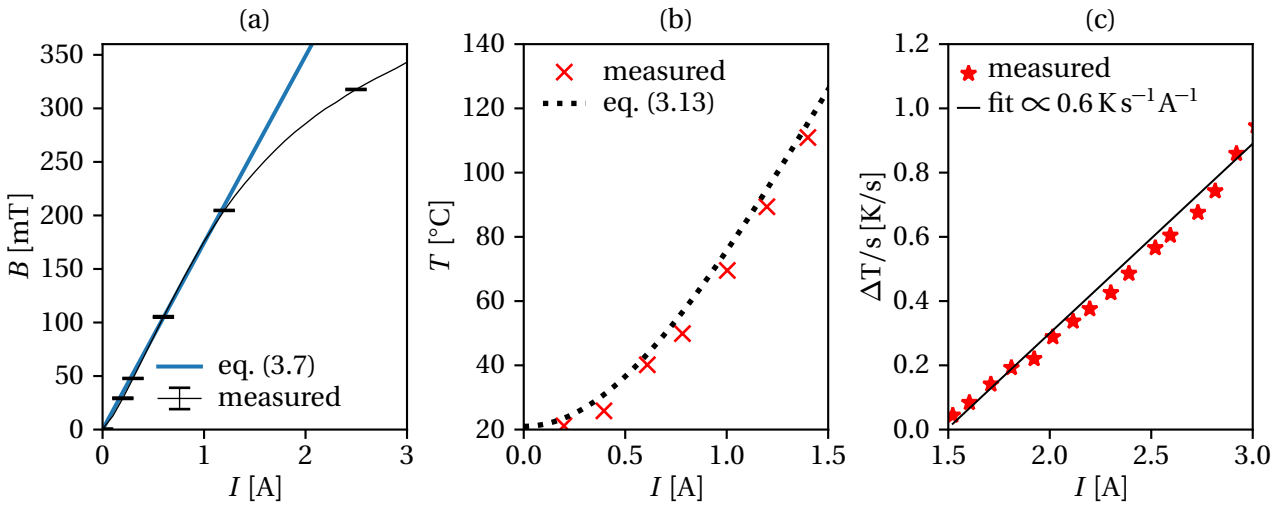

Figure 3.9: (a) Measured (black) and predicted (blue) magnetic field, according to eq. (3.7). (b) Measured (red) and predicted (dotted) temperature of the coils, according to eq. (3.13). Above 1.5 A, the current is applied in a pulsed manner. Therefore, the change in temperature over time is displayed instead (c).

are recommended to prevent overheating. For this reason, Figure 3.9 (c) shows the temperature change per second as a function of the current in black. At $I = 3\,\mathrm{A}$, it can be operated for about 150 s before the maximum tested temperature of 150 °C is exceeded.

The yoke is made from S235JR steel, which has a high magnetic conductivity. However, because it is ferromagnetic, it is also susceptible to remanence fields. During the simulation of the particle trajectories in the spectrometer, the magnetic field is derived from the applied current, so a fresh magnetization is needed every time current is reapplied to ensure a correct value. For this purpose, an H-bridge inverter was used to apply alternating currents to the coils. It is programmed to output a **p**ulse **w**idth **m**odulation (PWM) signal with a period of 150 ms. The vanishing AC duty cycles demagnetize the spectrometer reliably to ±0.5 mT. Note that the remanence field could mostly be prevented if a laminated soft iron core was used. Additionally, this type of demagnetization might not be possible if the inductance is large. When current is reapplied, the magnetization follows the well-defined new magnetization curve, as illustrated in black in Figure 3.9 (a). To also account for the correct shape of the field, a three axes Hall sensor (Infineon TLE493D-W2B6) was moved across the gap. This was repeated for multiple currents in the range between 0 and 0.7 A of applied current. The mean results per current are displayed in Figure 3.10. The slight asymmetries in amplitude originate from manufacturing tolerances and were found to have a negligible effect on the trajectories because the asymmetric fraction contributes two orders of magnitude less to the effective field.

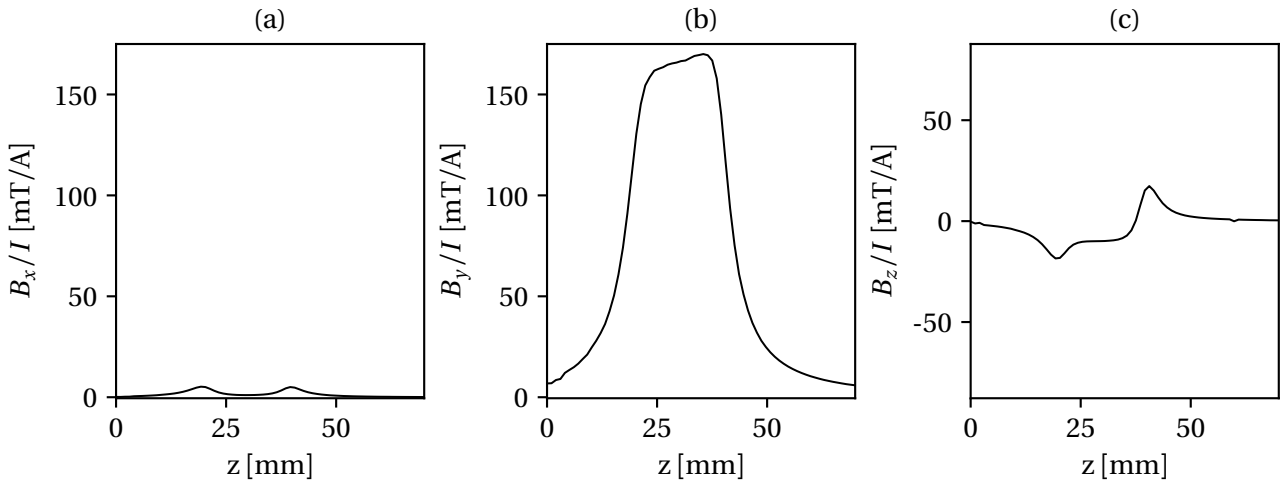

Figure 3.10: Measurement of the magnetic field components across the yoke gap which sits between the 20 mm and 40 mm mark. The directions are the same as shown in Figure (1). (a) Illustration of the component in y-direction for different currents. (b) Magnetic field in z-direction for a current of 0.7 A. (c) x-component for 0.7 A.

In terms of the electric field, simulations by Laplace interpolation [132] were performed to obtain the proper vector field per unit of voltage. The result of the simulation is shown in Figure 3.11. Due to the radial symmetry of the capacitor, the three dimensional field is fully known by the two dimensional cross section.
In a last step, it was verified that the orientations of the electric and magnetic fields are perpendicular. This was done using the ion emission of a plasma by sequentially switching on and off different types of fields. Figure 3.12 shows that the alignment is close to perfectly perpendicular, as the deflection is orthogonal.

3.2.2 TPS spectra

This section is dedicated to the process of reading the spectra from the measured parabolas [12]. In a first step, the particle trajectories through the spectrometer are simulated determining the fields as shown in the previous section. They are then fed into a ray-tracing algorithm that solves the equation of motion with a Runge-Kutta scheme of fourth and fifth order [133]. This is done for a set of particles spanning an appropriate range of kinetic energies and charges. This way, it is known which point in the detection plane is crossed, and by which particle. Thereby, the particle energies are chosen such that they are equally spread on the detector

$$E_{\mathrm{i}} = \left[\left(\frac{1}{(E_{\mathrm{max}})^{3/2}} - \frac{1}{(E_{\mathrm{min}})^{3/2}}\right)\frac{\mathrm{i}-1}{\mathrm{N}-1} + \frac{1}{(E_{\mathrm{min}})^{3/2}}\right]^{-2/3}, \quad i = 1...N. \tag{3.15}$$

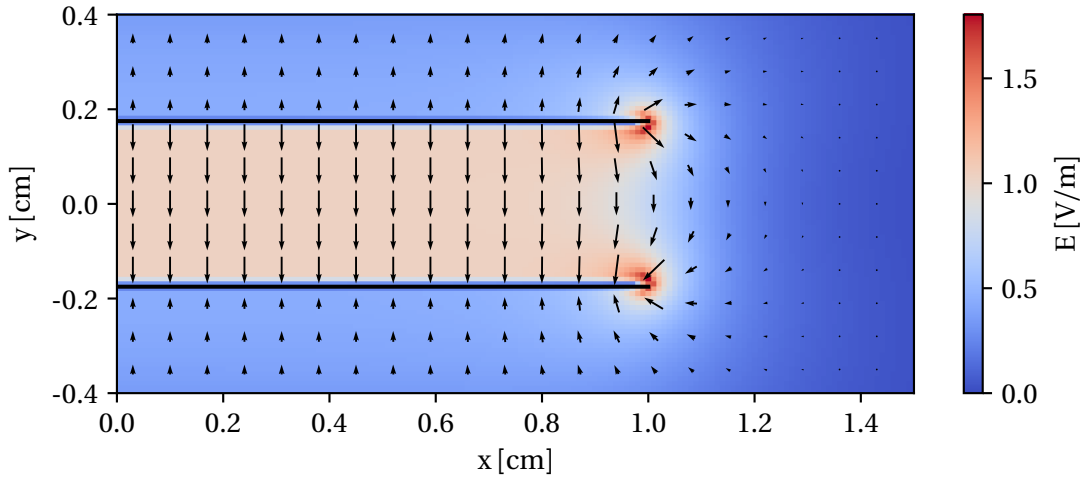

Figure 3.11: Half cross section of the electric field, as simulated according to Laplace interpolation [132]. Due to the rotational symmetry of the problem, the 2D field can be rotated around the y-axis to obtain the full result.

This way, the issue of too thinly sampled spectra in the low energy area is addressed, while also preventing the same detector pixel from being read multiple times. After that, the coordinates on the detector, which intersect the calculated parabolas, can be assigned a certain particle energy and species.

Due to the actual aperture size, the pixel values are not exactly the wanted spectra f, but rather a convolution $(f \circ g)$ of the normalized **t**ransfer **f**unction (TF) g with f. Therefore, to obtain f, the convolution theorem for Fourier transforms

$$\mathscr{F}(f \circ g) = \mathscr{F}(f) \cdot \mathscr{F}(g) \quad , \tag{3.16}$$

is applied. Note that an alternative method, without the use of **f**ast **F**ourier **T**ransform (FFT)s, is also presented by Burger and van-Cittert[134, 135].

However, how to measure $(f \circ g)$ and retrieve f is not trivial. The main reason is that the parabolic trace on the detector is a two dimensional object instead of a pixel perfect thin line due to the aperture. But, the final spectrum is only one-dimensional, and thus, one dimension must be integrated out in the readout process. This process is tied to g, which is composed of two parts. One part is due to the spectrometer dependent **o**ptical **t**ransfer **f**unction (OTF), which is convoluted with the mapping of the ion spectrum. The other one comes from the readout process, during which inevitably some area of the detector is integrated, as described by the **a**mplitude **t**ransfer **f**unction (ATF).

The OTF describes how a single, mono-energetic spectral point is spread on the detector, in our

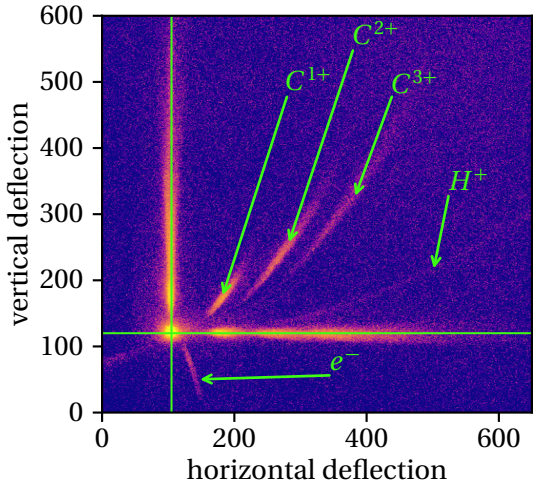

Figure 3.12: Measurement of the orthogonality of the TPS fields with: The magnetic field only (horizontal line), electric field only (vertical line), and both combined (parabolas). While the electron trace is also visible (for the electric field only measurement), additional deflection is caused by magnetic field of the Earth.

case. For this reason, it is also referred to as PSF in literature. In optics, where diffraction is not negligible, the PSF takes to form of Airy discs, for example. Because diffraction is virtually non present for ions, the PSF resembles an enlarged image of the aperture

$$PSF(r,l) = \begin{cases} 1 & ;\sqrt{l^2 - r^2} \leq \frac{D}{2} \\ 0 & ;\text{else} \end{cases} \quad , \tag{3.17}$$

with diameter D. The PSF is shown in Figure 3.13 (a) as the light blue circle. Here, l is the coordinate along the parabola, and r is the coordinate across.
The ATF function describes how the two-dimensional signal $S_D(r,l) = (f \circ PSF)$ of a single parabola on the detector is collapsed into the one dimensional convolution

$$(f \circ g)(l) = \int_{-\infty}^{\infty} \int_{-\infty}^{\infty} S_D(r,l) \cdot ATF(r, l^* - l) \, dr \, dl^* \quad . \tag{3.18}$$

One basic approach is simply reading the detector values along the simulated parabola, with Dirac delta functions

$$ATF(r,l) = \delta(r)\delta(l) \quad . \tag{3.19}$$

Finally, the transfer function $TF = (ATF \circ PSF)$ can be calculated due to the associativity of

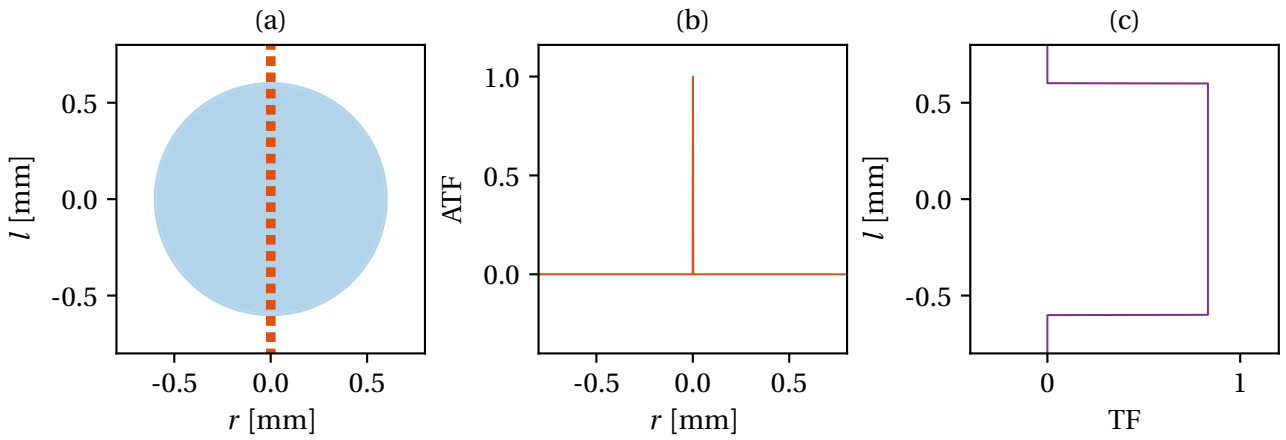

Figure 3.13: (a) OTF (blue) and points at which the detector values are read (orange). (b) Delta function ATF for the dots in the left frame. (c) TF obtained by integrating out the r-dimension.

convolutions

$$TF(l) = \int_{-\infty}^{\infty}\int_{-\infty}^{\infty} PSF(r,l^*)\cdot ATF(r,l^*-l)\,\mathrm{d}r\,\mathrm{d}l^* \tag{3.20}$$

$$= \begin{cases} 1 & ;|l| \le D/2 \\ 0 & ;\text{else} \end{cases} \quad . \tag{3.21}$$

Figure 3.13 (a) shows the ATF as orange dots across r and the convolution axis. (b) shows only the ATF along r, while (c) displays the resulting step function. The normalized TF g is simply the TF normalized to one

$$g(l) = \frac{TF(l)}{\int_{-\infty}^{\infty} TF(l)\,\mathrm{d}l} \quad . \tag{3.22}$$

To minimize the noise, however, it is favorable to also include the pixels perpendicular to the parabola in the readout process, for example, with

$$ATF(r,l) = 1\cdot\delta(l) \quad . \tag{3.23}$$

In this case, the TF is given by the chord length of the circle at position l:

$$g(l) = \begin{cases} \frac{8}{\pi D^2}\sqrt{\left(\frac{D}{2}\right)^2 - l^2} & ;-D/2 \le r \le D/2 \\ 0 & ;\text{else}\,. \end{cases} \tag{3.24}$$

This scenario is shown in Figure 3.14.

It should be noted that, in most practical cases within this work, the length of the spectrum on

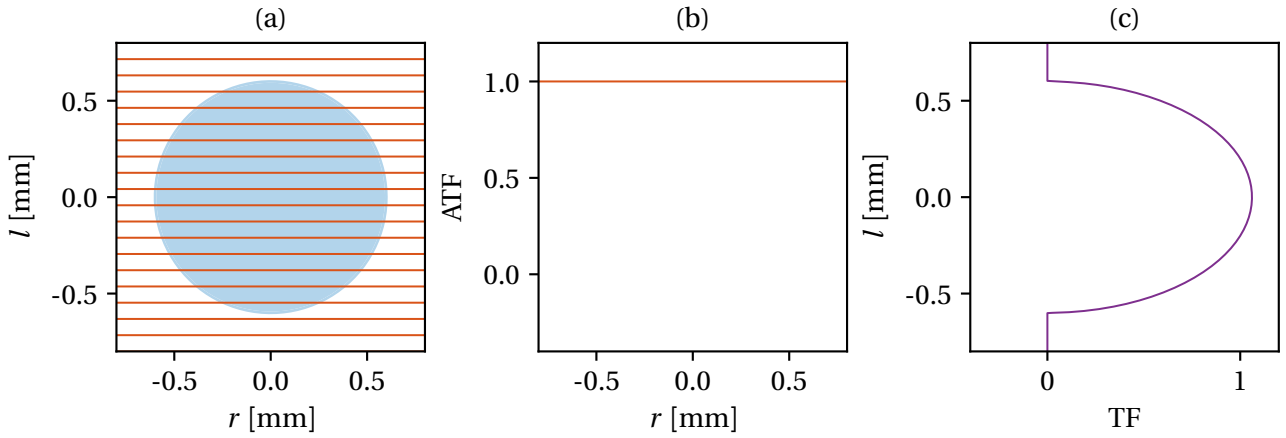

Figure 3.14: (a) OTF (blue) and lines along which the detector values are read (orange). (b) Constant ATF for the lines in the left frame. (c) TF obtained by integrating out the r-dimension.

the detector is significantly longer than the aperture image D. Therefore, the spectra are almost unchanged by the deconvolution. Note that operations, such as smoothing the spectra, are also a type of convolution which changes the TF. When the spectra are smoothed, the size of the frame should therefore be sufficiently small when compared to the total spectrum, such that its low frequency impact can be neglected.

Both ATF approaches presented above yield the same spectra under noiseless conditions. In practice, however, using the latter approach yields less noisy results because it averages over a larger area of the detector.

Sometimes, the Fourier transform of the TF g approaches zero in a region where the FT of $f \circ g$ is not quite zero itself. This leads to artifacts of f due to division by zeros. The simplest solution in this case is to truncate $\mathscr{F}(f \circ g)$ where $\mathscr{F}(g) \to 0$. However, this takes out high frequencies, which is the reason the deconvoluted spectra might appear smoothed. So, in practice, a choice must be made between a deconvolution with some smoothing, and no deconvolution with no smoothing.

Shifted Maxwell Boltzmann distribution

Once the spectra are measured, it is useful to parametrize them. An often used method in the context of laser plasma expansion is the shifted Maxwellian distribution [136, 137, 138]

$$\frac{\mathrm{d}f}{\mathrm{d}E}(v) = A\left(\frac{m}{2\pi k_B T_c}\right)^{3/2} v^3 \exp\left(-\frac{m}{2k_B T_c}(v - v_c)^2\right) \quad . \tag{3.25}$$

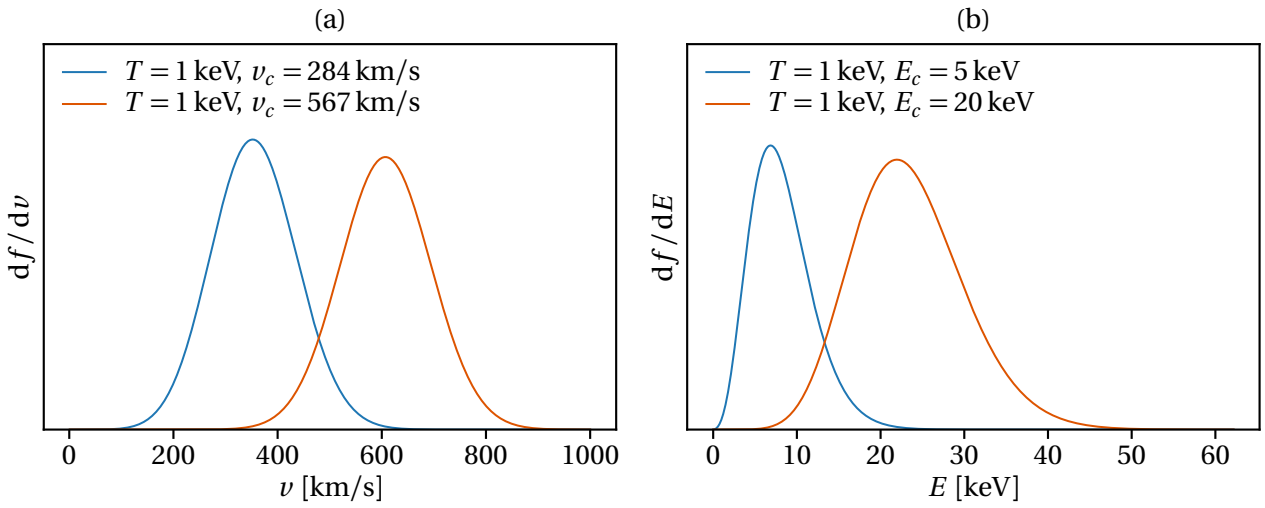

Figure 3.15: Examples of a shifted Maxwell distribution in (a) the velocity representation and (b) the energy representation.

Here, A is a normalization constant, T_c is a temperature, m is the particle mass, and v_c is a velocity offset. The idea behind this equation is that thermal ions, whose velocities are Maxwellian distributed, get offset due to additional acceleration. Because, in many cases, static electric fields are the cause, it is also called **C**oulomb **s**hifted (Maxwell-)**B**oltzmann (CSB) distribution, and the variables carry the $_c$ subscript.

The temperature T_c must be treated cautiously because it is generally not comparable to the one causing the charge state distribution. Opposed to the former electron temperature T, which is reached during expansion, T_c is the (ion) temperature during early and dense states of the plasma, and is thus higher.

Sometimes, an additional velocity term $v_a = \sqrt{\gamma k T/m}$ (speed of sound [139]) accounting for the adiabatic expansion is included in the exponent [4, 140]. This was omitted here, because the supra-thermal velocities are higher, and the term is generally small compared to v_c. It should be noted, however, that consequentially, v_c is an integrated offset velocity accounting for all mechanisms.

Figure 3.15 shows an example of the shifted Maxwellian distribution in its velocity $\mathrm{d}f/\mathrm{d}v$ and energy representation $\mathrm{d}f/\mathrm{d}E$. It is apparent that the most probable energy is not the shifted energy E_c due to the nonlinear conversion from energy to velocity. Also, note that T_c is a rather descriptive term, as there are other reasons that broaden a spectrum, such as spatial or transient field effect.

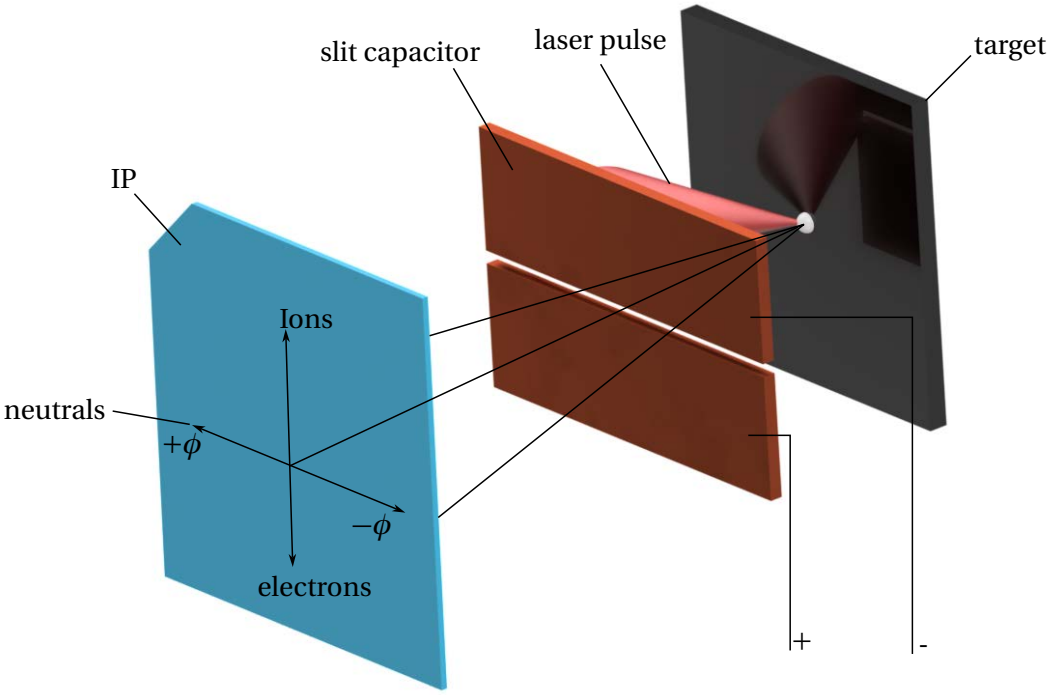

Figure 3.16: The experimental setup used to find the principal emission axis of the ions. The slit capacitor resolves the particle emission by kinetic energy, charge, and emission angle in the horizontal plane.

3.2.3 Slit capacitor

One major point of interest is the emission cone of the ions in order to set up the TPS properly. For this purpose, a simple setup using a charged slit aperture paired with an 20×20 cm IP was used. This assembly is shown in Figure 3.16.

The gap is 0.5 mm wide, has a depth (along ion trajectory) of 3 mm, and is 60 mm long. It is placed 5.5 cm in front of the plasma and 6.5 cm in front of the IP. An applied voltage of 300 V proved to be a good value for a sufficient species separation.

Due to the nonlinear deflection and decreasing solid angle $d\Omega = \mathrm{d}\phi\,\mathrm{d}\theta$ per pixel $1\mathrm{px} = \mathrm{d}x\,\mathrm{d}y$, the brightness values must be corrected.

$$\frac{\mathrm{d}PSL}{\mathrm{d}\phi\,\mathrm{d}v} = \frac{\mathrm{d}PSL}{\mathrm{d}x\,\mathrm{d}y} \cdot \frac{\mathrm{d}x}{\mathrm{d}\phi} \cdot \frac{\mathrm{d}y}{\mathrm{d}v} \tag{3.26}$$

$$= \frac{\mathrm{d}PSL}{\mathrm{d}x\,\mathrm{d}y} \cdot \frac{a}{\cos^2\phi} \cdot \frac{\mathrm{d}}{\mathrm{d}v} \cdot \frac{qUlb}{mv^2\cos^2\phi} \tag{3.27}$$

$$= \frac{\mathrm{d}PSL}{\mathrm{d}x\,\mathrm{d}y} \cdot \frac{a}{\cos^2\phi} \cdot \frac{k_q b}{v^3\cos^2\phi} \tag{3.28}$$

In this equation, q is the charge, and $k_q = -2qUl/m$ is a constant which includes the geometry (l and s) and field parameters (U) of the particle deflection in a capacitor, similar to Equation (2.48). Since the effective field $U_{\text{eff}} = U/\cos\phi$ and free flight distance $s = b/\cos\phi$ depend on ϕ, a factor of $1/\cos\phi$ is added for both variables.
a is the distance from the plasma to the detector, b is the distance from the aperture to the detector, ϕ is the horizontal deflection, and v is the particle velocity. After this conversion, the brightness values are corrected due to the nonlinear mapping.
Because the species are normally not entirely separated, a CSB can be assumed to extrapolate the full spectra, as will be shown in section 4.1.

3.3 Saha solver

As previously mentioned, the scheme discussed in [80] was used to find the solution to the Saha equations. In a first step, the root in Z_{av} of the equation

$$Z_{\text{av}} - \sum_{j=1}^{J} c_j \underbrace{\left(\sum_{i=1}^{Z_j} \frac{i \prod_{m=1}^{i} S_{m,j}}{(Z_{\text{av}} n_H)^i} \right)}_{\Xi_1^j} \underbrace{\left(1 + \sum_{i=1}^{Z_j} \frac{\prod_{m=1}^{i} S_{m,j}}{(Z_{\text{av}} n_H)^i} \right)^{-1}}_{1/\Xi_2^j} = 0 \tag{3.29}$$

is found. Here, $S_{m,j}$ is the Saha coefficient of the m-th ionic, and j-th elemental species

$$S_{m,j} = 2 \frac{U_{m+1,j}}{U_{m,j}} \frac{1}{\lambda_B^3} \exp\left(-\frac{I_m^{\text{eff}}}{k_B T} \right) \quad , \tag{3.30}$$

and c_j is the fraction of the elemental species.
For this purpose, the bisection algorithm [141] was used, since it can yield better results close to solid densities, where rapid changes in the average ionization and sudden truncations of the partition functions happen, when compared to the Newton method [142], for example. While this can be set to any accuracy, note that for high IPDs, sometimes convergence is not reach for the desired accuracy, as levels are depressed out of the partition function. An accuracy of 10^{-3} was found to be a good compromise in terms of reliability and speed.
However, it was also found that the algorithm does not always converge because of the finite precision of the floating-point format. This issue occurs predominantly for high-Z materials, where Ξ_1 and Ξ_2 sometimes diverge. A first fix was normalizing all densities to the heavy particle number density n_H, including $1/\lambda_B^3$. While this is sufficient in most cases, high ionization of about 20 and above causes issues in the product terms. For this reason, eq. (3.29) was solved in

the log-space with the help of the log-identities

$$\ln\left(\frac{i}{(Z_{\mathrm{av}})^i}\prod_{m=1}^{i}S_{m,j}\right)=\underbrace{\ln i - i\ln Z_{\mathrm{av}}+\sum_{m=1}^{i}\ln S_{m,j}}_{b_i} \quad , \tag{3.31}$$

the sums in eq. (3.29) become

$$\Xi_1^j=\sum_{i=1}^{Z_j}\exp(b_i-b_{\max}) \tag{3.32}$$

$$\Xi_2^j=\exp(-b_{\max})+\sum_{i=1}^{Z_j}\exp(b_i-\ln i-b_{\max}) \quad . \tag{3.33}$$

Here, $b_{\max}=\max(b_i)$, $i\in 1...Z_j$ are the maximum terms of the sum. This shift by $b_{\max}$ in the exponent is what makes divergence of the sums less likely if many species ($\gg 10$) are present. Further, if $b_{\max}$ is so large that $\exp(b_{\max})$ cannot be sufficiently described by a typical floating point number ($b_{\max}\sim 700$ for 64-bit), the first term of $\Xi_2^j\to 0$ becomes negligible, while $\Xi_{1,2}^j\to 1$ approach one. In any case, in the fraction Ξ_1^j/Ξ_2^j the shift cancels out, leaving the result unchanged. Finally, eq. (3.29) can be calculated with the fraction of the sums

$$Z_{\mathrm{av}}-\sum_{j=1}^{J}c_j\frac{\Xi_1^j}{\Xi_2^j}=0 \quad . \tag{3.34}$$

This way, materials such as gold can be computed, even at high degrees of ionization. The other quantities of interest, average ionization per elemental species, fractions of the i-th ionization of the j-th species, can then be derived analytically. By first computing

$$\alpha_{0,j}=\frac{c_j}{\Xi_2^j} \tag{3.35}$$

$$\alpha_{m+1,j}=\frac{\alpha_{m,j}}{Z_{\mathrm{av}}}S_{m,j} \quad , \tag{3.36}$$

and then, calculating the wanted densities

$$n_{m,j}=\alpha_{m,j}n_h \tag{3.37}$$

$$n_e=Z_{\mathrm{av}}n_h \quad . \tag{3.38}$$

As this will be heavily used throughout this work to examine the plasma emission, a few test cases are discussed here to demonstrate that it was properly implemented. At first, the simple analytical scenario of low density hydrogen is calculated, where the IPD is negligible. If we take

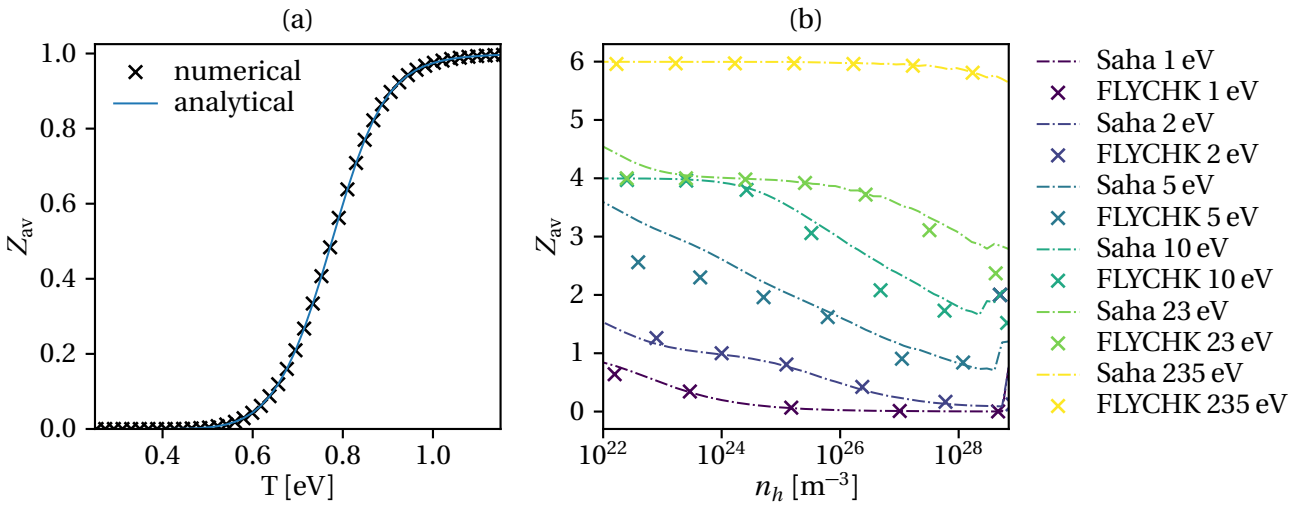

Figure 3.17: (a) Comparison of the analytical solution of a hydrogen plasma to the numerical solution of the implemented Saha solver. (b) Comparison of FLYCHK results to the Saha solver for a carbon plasma over a set of temperatures.

only the ground state degeneracies $U_I = 2$, $U_{II} = 1$ into account, the Saha equation becomes

$$\frac{n_{II} n_e}{n_I} = \frac{1}{\lambda_B^3} \exp\left(\frac{-R_h}{k_B T}\right) \quad . \tag{3.39}$$

This can be done as the energy levels of the above ground states $E_{n>1}$ are all at least 10.2 eV higher than E_1, which drastically diminishes the Boltzmann coefficient. After introducing the heavy particle density $n_H = n_I + n_{II}$, this equation can be written as

$$\frac{n_{II}^2}{n_H^2\left(1-\frac{n_{II}}{n_H}\right)} = \frac{1}{n_H \lambda_B^3} \exp\left(\frac{-R_h}{k_B T}\right) \quad . \tag{3.40}$$

Here, the electron density was substituted by the hydrogen ion density $n_e = n_{II}$. In the special case of hydrogen, the fraction n_{II}/n_H equals the average ionization Z_{av}, which yields

$$\frac{Z_{\text{av}}^2}{(1-Z_{\text{av}})} = \frac{1}{n_H \lambda_B^3} \exp\left(\frac{-R_h}{k_B T}\right) \quad . \tag{3.41}$$

For a given particle density and temperature, this equation can now be solved for Z_{av}. The results for different temperatures are shown in Figure 3.17 (a). Here, a heavy particle density of $n_h = 10^{20}$ m^{-3} was used.

As a benchmark for high densities, the solutions can be compared to the non-LTE code FLYCHK [143]. However, it should be noted that FLYCHKs results are best for highly ionized plasma and intermediate electron densities. Therefore, the comparison is limited to the glassy carbon solid density range of $7 \cdot 10^{28}$ m^{-3} to $1 \cdot 10^{22}$ m^{-3}. In this regime, both methods show mostly good agreement. While FLYCHK also uses the SP IPD, it is noteworthy that a slightly different definition of

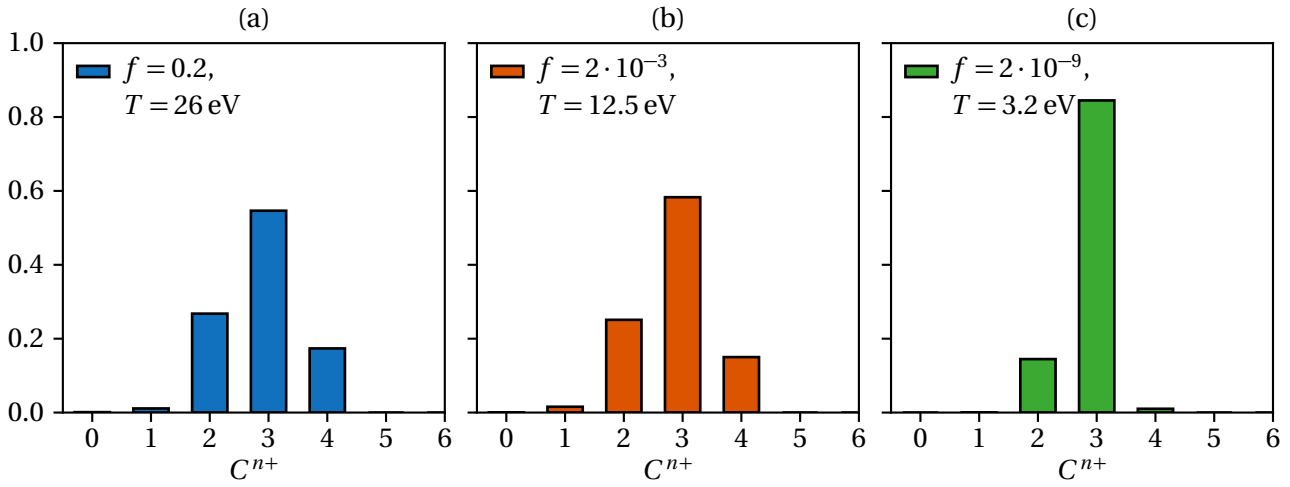

Figure 3.18: Comparison of carbon plasma at three different densities and temperatures, but the same average ionization Z_{av}. The f value gives the plasma density in multiples of the solid density $n_{\text{solid}} = 7 \cdot 10^{28}\ \text{m}^{-3}$.

the ion sphere radius is used [144]. The difference is a factor of $(1/\pi)^{1/3} \approx 0.68$. Here, however, it was decided to use the definition given in [92].

3.4 Retrieval of plasma parameters

With the use of the Saha solver, a plasma temperature and density can be deduced from a CSD. The idea is to solve the Saha equation for a wide variety of (T, n) values and compare the results with the measured data. Over simplified one could say that at a fixed temperature, a low density yields a narrow CSD down to a single dominant species. This can be seen in Figure 3.18 (c), where a carbon plasma of about $10^{20}\ \text{m}^{-3}$ density and 3.2 eV temperature is populated mainly by the C^{3+} species.

By temperature variation, the dominant species can be selected. An increase in density broadens the CSD, which can be seen in Figure 3.18 (a) and (b). If we compare (a) and (b), it is apparent that the distributions are lookalikes, even though there is a density difference of two orders of magnitude and the temperatures differ by a factor of two.

Therefore, the assumption that each (T, n) yields a unique distribution is valid only for a certain parameter range, instead of a precise value combination. On the plus side, this makes the model of instantaneous freezing more applicable, as it allows for some variation in the variables before the CSD changes drastically.

Another unknown is the influence of plasma contaminants due to residue on the target surface,

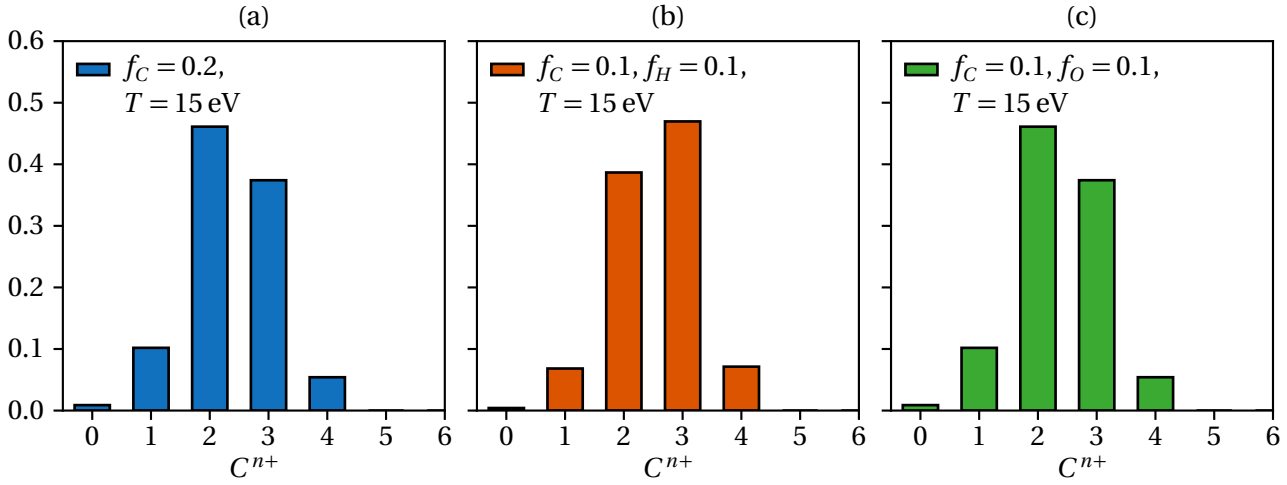

Figure 3.19: Comparison of carbon charge state distributions within plasmas of the same number density and temperature, but different mixtures of carbon, hydrogen, and oxygen.

for example. As these may or may not be detectable in the TPS, Figure 3.19 (a-c) is a brief analysis of the CSDs. Section (a) displays the CSD of a pure carbon plasma at $f = 0.2$ and $T = 15$ eV. In part (b), the plasma has the same heavy particle number density, but half of it is hydrogen. Since hydrogen has only one electron, the (free) electron density is lower, which corresponds to less occupied room in the phase-space. As a result, electrons from the bound carbon become free to reoccupy this space, and thereby increase the average carbon ionization. Because oxygen has roughly similar atomic/ionic properties to carbon, in the C and O mixture, the changes in CSD are minor (part (c)). Note that these examples cover high fractions of probable contaminants. As there are expected to be only a few atomic layers thick of residual carbohydrates and water on the target surface, this is a worst case estimate. Thus, pure plasma are assumed in the following CSD evaluations.

Now, the important aspect is how to compare the measured and computed CSD. One approach is calculating the CSD for a random (T,n) combination and comparing it to the measured one with the least residual squares method. This process is repeated until the (T,n) with the least deviation is found. The result of this process is shown in Figure 3.20 (a). with an uncertainty of $\sigma_{\mathrm{CSD}} = 0.2$ (orange), and the Saha solution of one fitting within the errorbars (blue).

However, this process neglects two points: The uncertainty of the measured CSD, and the sensitivity of the computed CSD to a perturbation in temperature or density. To graphically represent the issue of sensitivity, on the right side, the (T,n)-map is shown, which displays the **g**oodness **o**f **f**it (gof) in terms of **l**east **a**bsolute **r**esiduals (LAR). Close to the best fits (yellow-green area), there are two areas encircled in red. This contour line demonstrates that, occasionally, and for

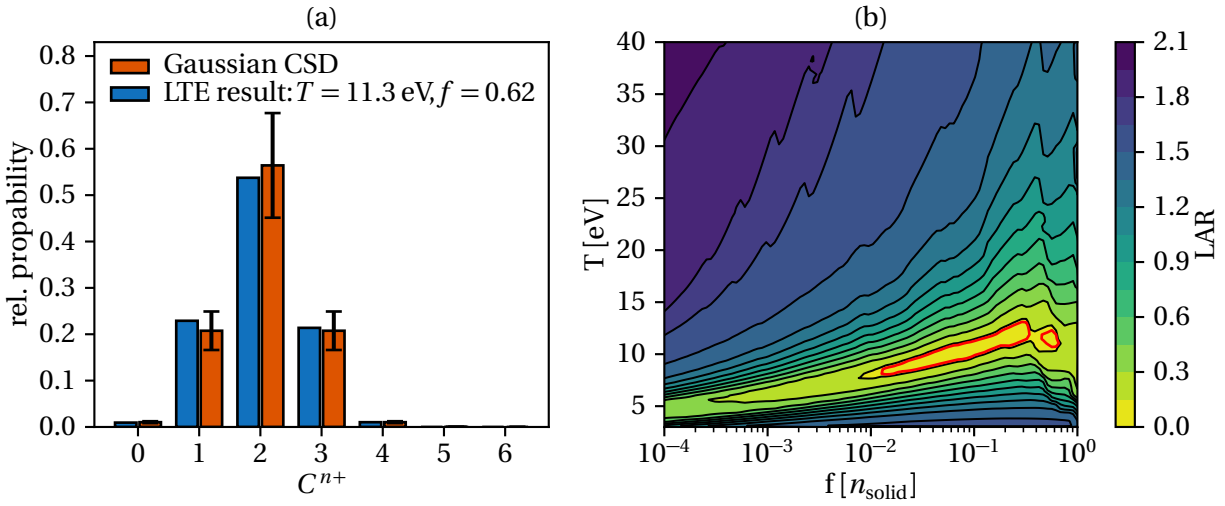

Figure 3.20: (a) Example comparison between a simulated CSD (blue) and an artificial Gaussian CSD. (b) The goodness of fit, in terms of least absolute residuals (LAR), between the artificial CSD and simulated ones across the temperature density plane. The red outlined isles indicate that in some cases, branching occurs.

some levels, there might exist multiple branches (two in this case). The question now is: How to choose the level of gof such that the sensitivity and error bars are represented in the end result. Suppose the map is recomputed multiple times for a randomly chosen distribution within the CSDs uncertainty. Then, the accuracy of (T,n) with respect to the data set is the positional variation of the geometric center of the branches: the bottom of the valleys on the (T,n)-map. This was done for Figure 3.21 (a) and (b), with 50 random drafts. If averaged over all branches and drafts, mean values and standard deviations can be found, which are represented by the black lines. This is the uncertainty of the method, as found by this **M**onte **C**arlo (MC) like approach, which is computationally expensive.

But, if the level for the contour line is properly chosen, if the first (mean) and second (standard deviation) moments of the (T,n)-values inside represent the errorbars of the CSD. To find which level corresponds to what uncertainty of the CSD, the procedure was repeated for varying σ_{CSD}. This is shown in Figure 3.22 (a) and (b), by the blue dots.

Finally, the level of the contour was varied to see how the uncertainty of the found (T,n)-pair changes in response. This is shown in Figure 3.22 (a) and (b), by the orange dots. It becomes apparent that, up to a level of about 0.4, the MC like method based on the CSD drafts yields the same values as the corresponding contour line. Above 0.4, the horizontal dimension of the plane is too restricted for a further increase of the LAR values, which can be seen in part (b). This correlation can be explained by the following:

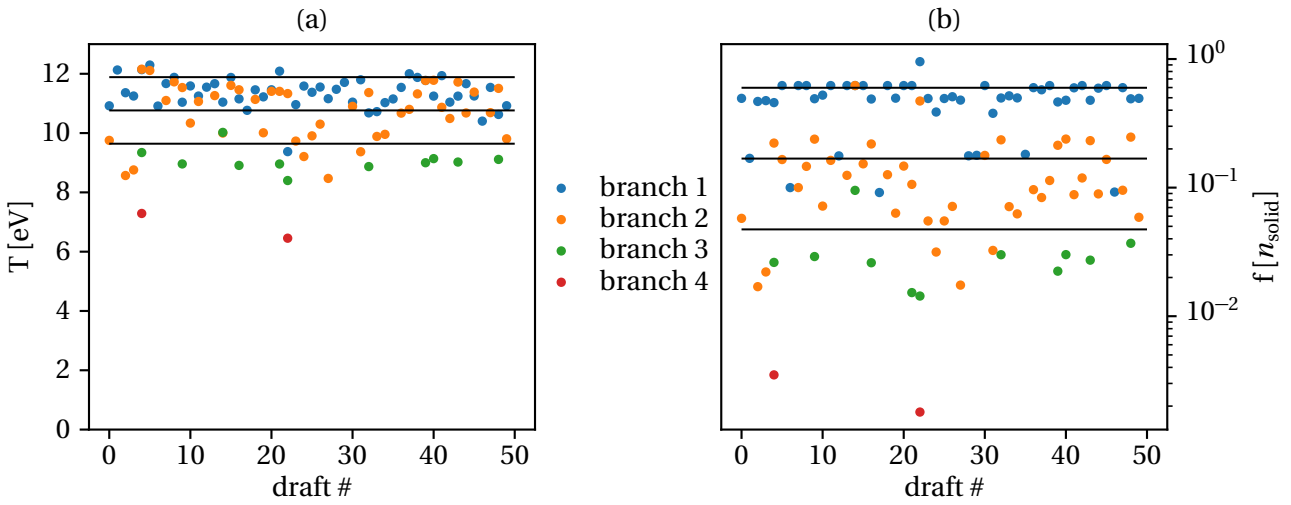

Figure 3.21: Temperature (a) and density (b), as found by the geometric center of the red encircled areas (branches) in the (T,n)-plane, for a number of random drafts out of the Gaussian CSD with an uncertainty of $\sigma_{CSD} = 0.2$. The black lines represent the mean values and the standard deviation, measured over all branches.

If a reasonable LTE result exists, it agrees within the error bars. The residual per species is thus limited to the size of its error bar. Therefore, the sum of the absolute residuals is limited to the sum of the error bars. This is the reason the LAR was chosen as the metric for the gof. Thus, the summation of the residuals allows for some slack in the agreement, as some species can over or undercut the measured CSD, if the others have sufficiently small residuals. However, Figure 3.22 (a) shows that the LAR method tends to yield a conservative estimate.
To summarize this section: The maximum allowed LAR, or height of the contour line in the (T,n)-plane, is chosen as the sum of the CSDs error bars. The assumptions made in the retrieval of the plasma parameters are therefore:

(i) during freezing, the plasma is weakly coupled with $\Gamma \ll 1$, such that SP potential lowering can be applied.

(ii) the partition functions are with a hard cutoff.

(iii) the spectrum can be assigned a set of plasma parameters (T,n) according to the freezing conditions.

(iv) the plasma is treated as pure target material only.

Even though the plasma is likely to be strongly coupled at some point during its evolution, for 1. to hold, only the coupling at the point of freezing matters. While hydrogen residuals sometimes

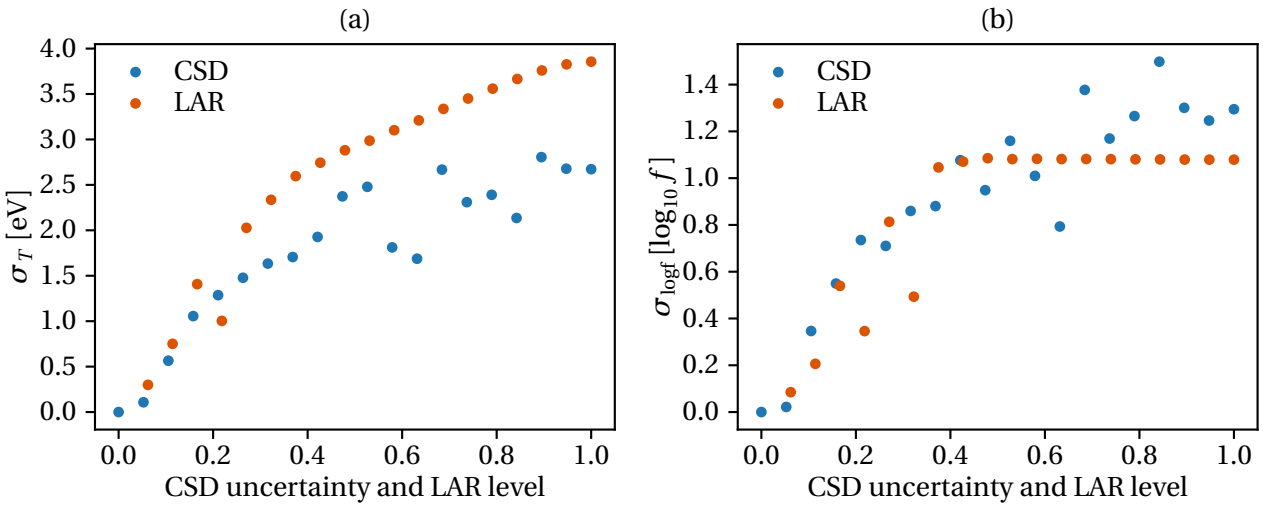

Figure 3.22: Standard deviation of the temperature (a) and density (b), as found by varying the relative CSD uncertainty (blue dots) and the LAR level in the (T,n)-plane (orange dots).

appear in the spectrum, they sit at very low kinetic energies, which leads to the assumption that they are ejected independently of the target material ions. Additionally, it was shown that hydrogen alters the computed CSD at high concentrations only. To elaborate on point 3.: Since, strictly, the freezing process does not happen instantaneously, the measured CSD is always a superposition of frozen CSD at multiple plasma parameters. However, even if instantaneous freezing is assumed, it must be further assumed that no kinetic energy is ejected during vastly different plasma conditions.

Chapter 4

Results and discussion

4.1 Carbon plasma

An important point for the experimental setup is the solid angle emission of the ion source, as this determines how critical the spectrometer alignment is. While the angle for spectrally integrated ablation is well studied for a variety of target materials, spectrally resolved measurements are performed to find the emission direction of the fastest ions.
For this purpose, a charged slit with a thickness of 3 mm was placed 3.8 cm in front of the plasma, as illustrated in fig. 3.16. In this setup, the distance from the plasma to the IP is $a = 9.5$ cm, and the distance from the slit capacitor to the IP is $b = 5.7$ cm.
The electric field is created by a 300 V potential across the 0.5 mm gap.
Charged particles passing the gap are then deflected according to their velocity, inertia, and charge. Because the slit is straight instead of curved around the plasma, particles passing through under a more shallow angle (large ϕ) are deflected more strongly. To illustrate this effect, the iso-energy lines are drawn into the IP frame in Figure 4.1 (a). This gives rise to three sections. One for the electrons at negative deflections, the one close to zero deflection for the neutrals, including X-rays and clusters, and the ions at positive deflections.
Inset (b) of Figure 4.1 shows the integrated deflection in each section across all angles. Interestingly, the target normal is also the principle axis of emission in the neutral section. Since X-rays are assumed isotropic, this might indicate that neutral carbon is emitted with a similar profile to the charged one.
Taking a lineout at $\phi = 0$ (Figure 4.2 (a)), three peaks for the carbon species can be observed. Due to valleys in the lineout, the ion section can be divided into one for each carbon species. Assuming a box shaped electric field, the particle velocities (and energies) can be evaluated. As shown in

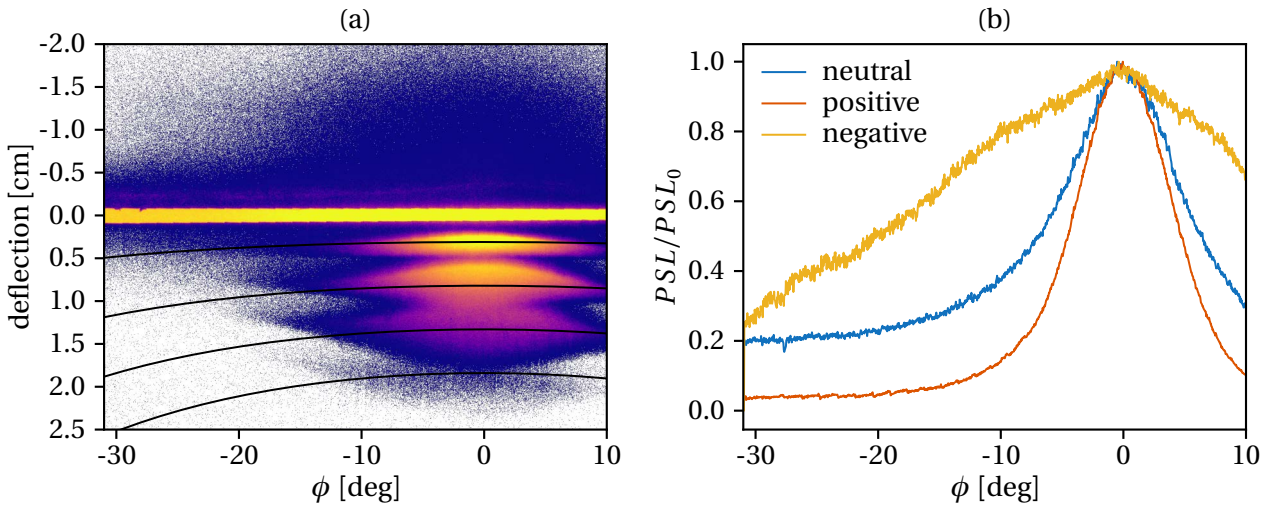

Figure 4.1: (a) IP data captured by the slit-capacitor and iso-energy lines drawn in black. (b) Angular distribution of the neutral (blue), positive (orange), and negative (yellow) charged emission as integrated from (a).

Figure 4.2 (b), a CSB fit was applied to the values within those sections in order to parametrize the spectra. Integrating the deflection in each segment and using the fit, the emission cone shown in Figure 4.3 (a), the spectral width shown in (b), and kinetic energy in (c), can be determined by the fit parameters. In this case, the spectral width is represented by the temperature T_{CSB}, and the energy by the offset in velocity E_c. While the spectral width decays towards larger angles, the kinetic energy stays approximately constant.
The shape of the emission can be parametrized as [145]:

$$I(\phi) \propto \cos^N(\phi) \quad . \tag{4.1}$$

Applying this equation to the data yields $N = 177$, or an FWHM of $2\phi = \arccos(0.5^{1/N}) \approx 10°$. Since this angle is known to become smaller with shorter pulses at similar fluence, it is comparable to the high intensities of $10^{15}\,\mathrm{W\,cm^{-2}}$ studied in [146]. However, in the work cited above, the spectral width increases with the angle, while the opposite is found here. Note that it is unknown where the lower cutoff for ion energies on IPs is, just that the IP does not see thermal particles with a couple eVs of kinetic energy.

4.2 Experimental setup

Due to these results, the TPS is ideally aligned perpendicular to the target surface. Figure 4.4 gives an overview of the different components in the octagonal vacuum chamber. As shown, tar-

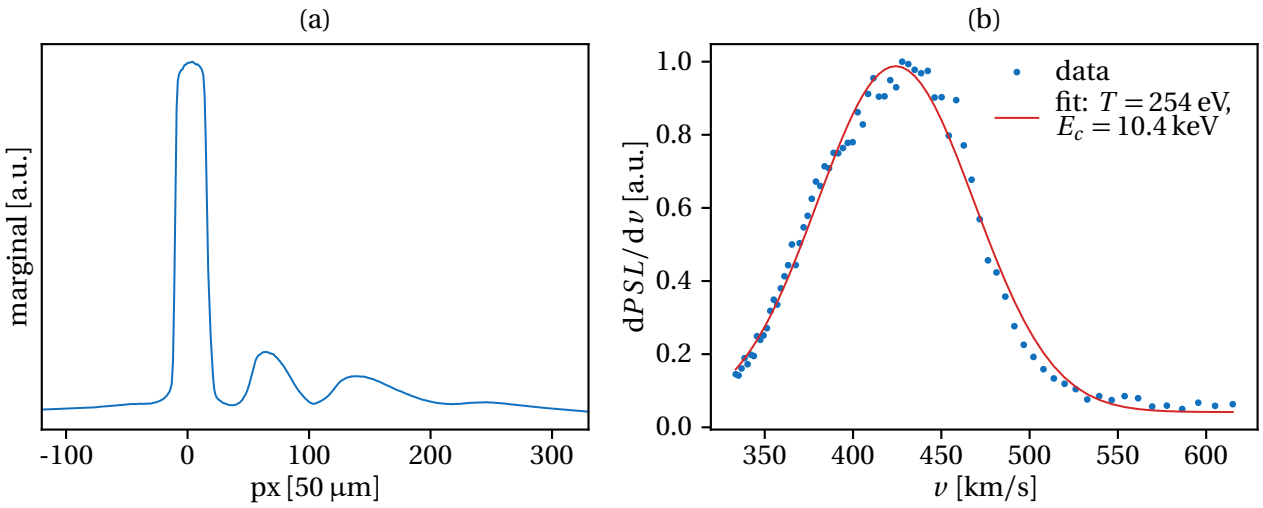

Figure 4.2: (a) Horizontal marginal of the IP data. (b) Example of the Coulomb shifted Maxwell-Boltzmann distribution fitted to C^{1+} signal in the target normal.

get and optics are integrated into vacuum with a pressure below 10^{-5} mbar.

In chronological order, the laser enters the setup from the right side. It is then reflected by the 90° off axis parabola with an effective focal length of 127 mm, or 5 inches. This illuminates an elliptical spot on the target due to the 45° incident angle. The reflected portion of the light is then dumped in the beam dump. The ions leave the lighted spot on target vertically, where the TPS is positioned.

In the TPS zone, the aperture of 200 µm diameter, the magnet-capacitor combination, and shielding from electromagnetic pulses and stray particles is installed. Usually, the distance from the target to the beginning of the TPS zone (aperture or pinhole) is approximately 15 cm, and the distance from there to the detector is 30 cm. Thus, the observed solid angle is about $1.4 \cdot 10^{-4}$ sr. The field zone of the TPS usually comes 5 cm after the pinhole.

For the detector, either Fujifilm image plates of the type BAS-TR1040 were used, or a microchannel plate from PHOTONIS USA (APD 1 PS 40/12/10/8 I 60:1 P43). It is a single MCP assembly (no stack) with an active diameter of 40 mm, 12 µm center-to-center spacing, pore size of 10 µm, and bias angle of $8° \pm 1°$. The used version is equipped with a P43 type phosphor screen. In this case, an Imaging Source camera DMK27BUP031 with an 16 mm objective captures the screen synchronized with the laser.

An example of the TPS traces can be seen in Figure 4.5 (a), with the simulated traces in the overlay, and the corresponding spectra in (b). As shown, the ionic species C^{1-5+} are present in an interval from about 2−10 keV kinetic energy. Interestingly, the energy does not scale with charge or charge to mass ratio.

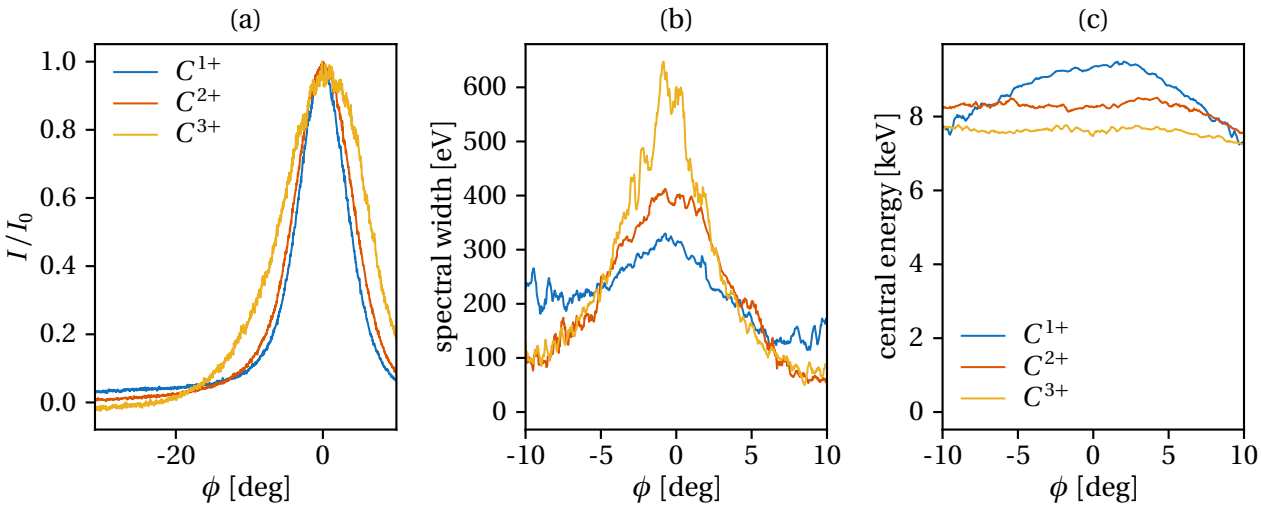

Figure 4.3: (a) Emission cone of the first three carbon species and their (b) spectral width and energies (c), according to the CSB fit.

This is also apparent in the hydrogen spectrum, which holds the slowest particles, besides the highest possible charge to mass ratio. Obviously, acceleration theories involving a constant electric field and charges in a bipolar layer struggle to explain this phenomenon. But before diving in depth into the charge states and kinetic energies, the results of multiple laser parameter scans are presented to paint a more complete picture of the driving factors behind the emission.

4.3 Single Pulse Laser Parameter Scan

For this purpose, parameter scans were conducted. Previous studies have demonstrated how to obtain fast ion emission with laser pulses of higher pulse energy than the PHASER and longer durations of tens-of-femtoseconds up to picoseconds [20, 35, 5, 36]. Therefore, the parameter range appears to be quite large in regards to successful supra-thermal ion generation.
However, the question regarding the driving factors remains. One common parameter, which is known to affect the ion and yield, is moving the target relative to the beam waist, as illustrated in Figure 4.4 [5]. As shown in Figure 4.6 for the total ions captured, this is also the case here. The maximum yield is reached at about ±100 µm. Since the Rayleigh length is 20 µm, this shift attenuates the peak intensity and fluence about one order of magnitude, down to 100 J cm^{-2}.
As of now, the change in emission cannot be attributed to a single factor, such as pre-plasma development. Rather, by changing z, many parameters are varied at the same time: fluence, intensity, curvature of the wave fronts, and plasma size, as well as the pre-plasma density, gradient, and temperature.

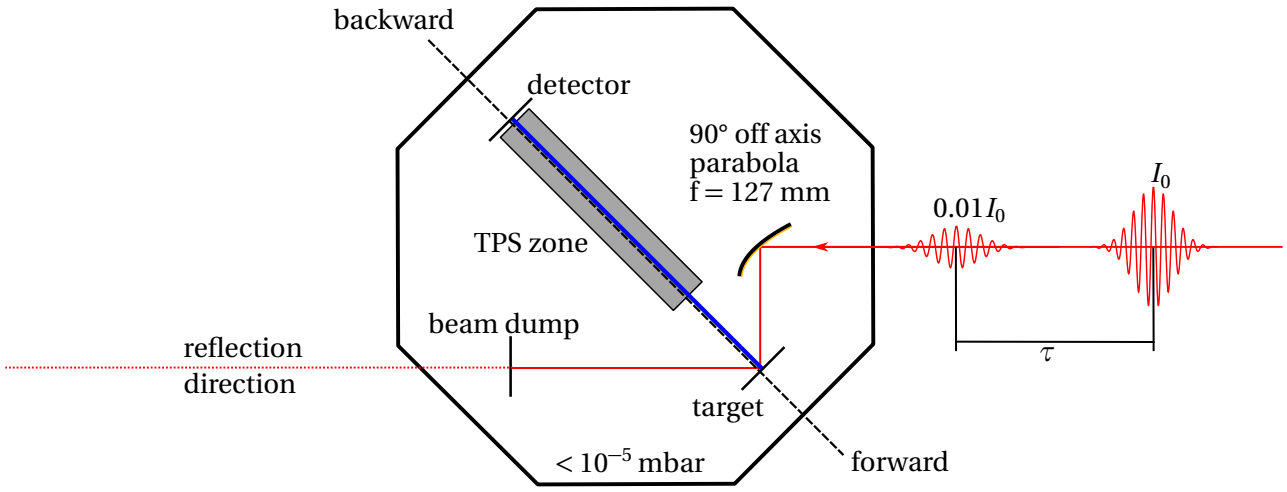

Figure 4.4: Experimental Setup: An 8 fs and 5 µJ laser pulse is used to ignite a pre-plasma on a glassy carbon target with an off axis parabola under 45° incident angle. It is then hit by an 8 fs, 500 µJ main pulse $\tau = 3$ ps after. The target surface is not positioned in the beam waist, but in a defocused position 120 µm towards the parabola.

Since the yield is slightly different for the directions of z, it can be concluded that the curvature of the wave fronts is not quite negligible in this case.
One explanation for the z-dependence is self-focusing in the pre-plasma [93]. For positive values of z, self-focusing works with the curvature of the wave fronts introduced by the parabola. For negative values, these factors counteract, and the incident wave fronts become flatter. This asymmetry might become more pronounced at higher intensities, where relativistic self-focusing [147] occurs. However, measurements with the third-order autocorrelator [148] showed that the ps-pulse contrast exceeds 10^8, which likely prevents the pre-plasma from extending far enough into the vacuum to sufficiently bend the wave fronts [149, 37]. Another, and more likely, cause of the asymmetry in yield is spherical aberration, which results in an asymmetrical beam waist [150].
Additionally, the change in yield occurs too suddenly to be solely caused by an increase in lateral plasma size. Therefore, plasma effects must either increase the total yield or reduce the angle of the emission cone.
To isolate the effect of each factor, a series of partly independent parameter scans with and without a dedicated pre-pulse were conducted.
In the literature, the spectra of the fast ion emission are sometimes described using a Maxwell-Boltzmann distribution shifted by a term accounting for the Coulomb propulsion, and adiabatic expansion [4], or a simple Gaussian [35]. While the goodness of fit is generally good for the found spectra, as demonstrated in Figure 4.3, not only the thermal nature, but also collisional friction

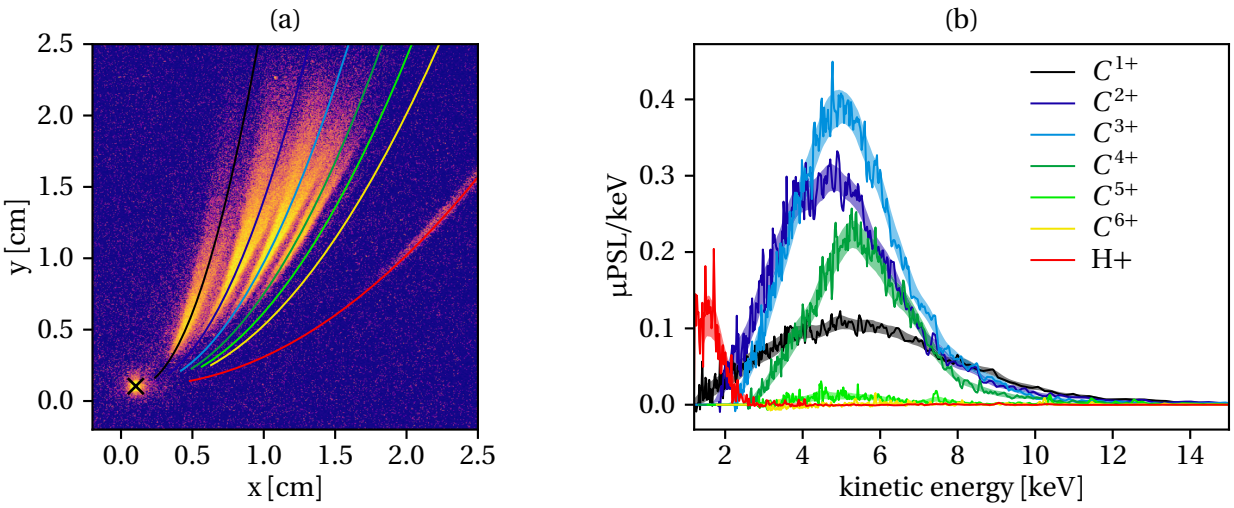

Figure 4.5: (a) Measured TPS traces and simulated parabolas for the carbon species (black to yellow) as well as protons (red). (b) Spectra corresponding to the data in (a).

and the timely collapse of the accelerating layer contribute to the spectral width.

For this reason, the spectra are characterized using weighted averages to describe the kinetic energy

$$\langle E_{\mathrm{kin}} \rangle = \frac{\sum_i \int E \cdot S_i(E)\,\mathrm{d}E}{\sum_i \int S_i(E)\,\mathrm{d}E} \quad , \tag{4.2}$$

and ionization states

$$Z_{\mathrm{av}} = \frac{\sum_i i \int S_i(E)\,\mathrm{d}E}{\sum_i \int S_i(E)\,\mathrm{d}E} \quad . \tag{4.3}$$

Figure 4.6 shows the corresponding average kinetic energy against the focal position z. Note that the abscissa is broken close to the focal position, as the signal in this region is too small for a reliable evaluation.

Defocusing affects the average order of ionization minimally, as it remains relatively steady at a value of $Z_{\mathrm{av}} = 2.5$. The kinetic energy, however, increased significantly, which correlates with the increase in fluence and intensity.

To factor out the illuminated area, a pulse energy variation was performed at the 40 µm defocused position. As shown in Figure 4.7, a maximum fluence of about 700 J cm^{-2} can be realized. At this position, the fluence exceeds the point of any significant yield. Tuning down the energy one order of magnitude, the yield peaks again between $50-100$ J cm^{-2}. Note that each setting requires optical realignment, which is why the peak was approached from both sides, resulting in a double data point.

This suggests that either the fluence or the intensity is the main driving factor of this emission.

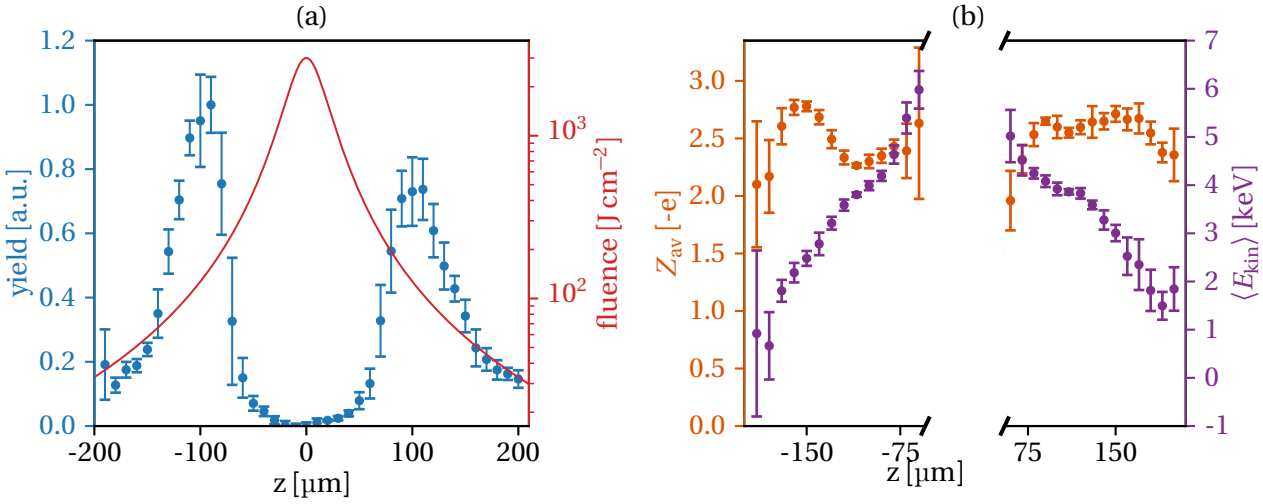

Figure 4.6: (a) Carbon yield, summed over all species with kinetic energies over 2 keV, depended on the focal position. A positive z value means the laser focus is positioned behind the targets surface. (b) Average order of ionization, and mean kinetic energy across the spectrum.

However, since the pulse pedestal is also attenuated, the time of the solid-plasma transition relative to the pulse center varies. This time delay is the subject of the next section.

To distinguish between fluence and intensity, the pulse duration was varied at the +100 µm position, with a constant pulse energy of 600 µJ and a fluence of 100 J cm^{-2}. This way, only the intensity is modulated.

For this purpose, the hollow core fiber was bypassed to use the pulses directly from the amplifier. This allows to tune the pulse duration by stretching the pulse in a grating compressor mirror pair. Doing so adds predominantly second order dispersion (chirp) to the spectral phase, which results in elongated pulses with a slight sweep in carrier frequency. This is limited to pulses with a sufficiently smooth spectrum, as with complex spectral shapes, the pulses tend to disintegrate if too much chirp is added, hence the amplifier pulses.

Therefore, the shortest possible pulse durations of about 5 fs were not included in the duration measurements. Random samples from the pulse train, as measured by SPIDER [54] are shown in Figure 4.8. Positive as well as negative dispersion was used to ensure possible effects due to the resulting carrier frequency sweep are taken into account.

As, especially the temporal profile of the longer pulses displayed in Figure 4.8 cannot be accurately described by a Gaussian shape, the duration was instead calculated using the maximum pulse intensity I_{max} according to

$$\tau = \int_{-\infty}^{\infty} \frac{I(t)}{I_{max}} \mathrm{d}t \quad . \tag{4.4}$$

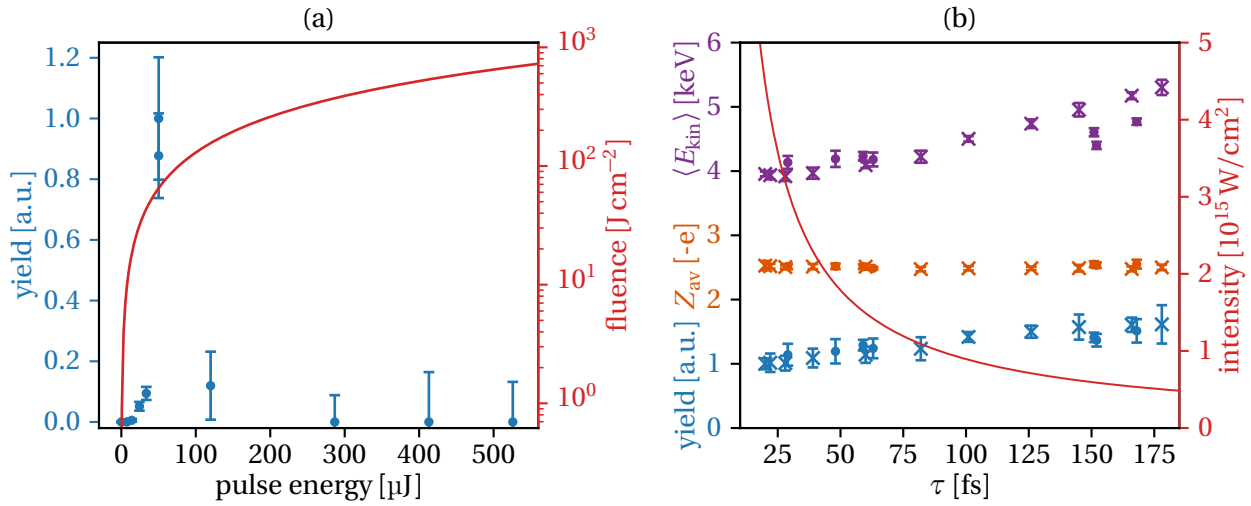

Figure 4.7: (a) Carbon yield for various pulse energies, and constant pulse duration. (b) Yield, average ionization, and mean kinetic energy for various pulse durations but constant fluence (pulse energy).

This metric is more robust compared to the usually used FWHM. For Gaussian shaped pulses, the values compare as $\tau \approx 1.06$ FWHM.

The results for these pulses are shown in Figure 4.7 (b). As depicted, there is a weak correlation between the pulse duration and signal strength. A decrease in intensity over an order of magnitude increases the yield only by a factor of 1.5. Similarly unaffected are Z_{av} and $\langle E_{kin} \rangle$ across the pulses.

This data suggests that the fluence is the driving factor of the emission, similar to TNSA type of accelerations, where, as long as sufficiently high intensities are sustained, the energy scales with fluence[16].

However, note that manipulating the spectral phase changes the ps-pulse contrast [151]. Consequently, more strongly chirped pulses may couple more efficiently to the preformed plasma [152] and thus increase the kinetic energy and yield. This will be discussed in more detail in the next section, with the help of a dedicated pre-pulse.

4.4 Double pulse plasma

For this purpose, a pre- and main-pulse configuration was set up, in which both pulses have an energy of 140 µJ. Figure 4.9 shows the result in a time frame of $0-3$ ps. It is found that ignition ideally occurs in close proximity to the main pulse, with an optimum at $200-300$ fs.

If the delay is too large, the yield goes to zero because the density gradient toward the vacuum

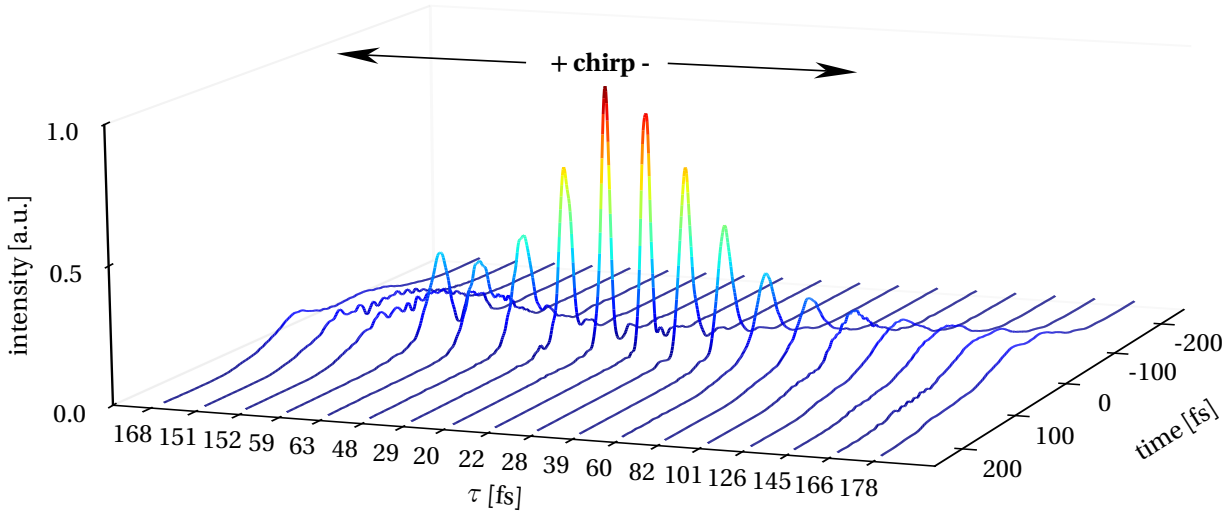

Figure 4.8: Laser pulse durations as reconstructed by the SPIDER diagnostic for positive and negative chirps. The pulse durations (τ values) were calculated by the metric presented in eq. (4.4). These representative pulse durations were used for the intensity parameter scan.

interface is too soft. This leads to the laser energy being deposited over a volume that is too large to establish a charge or density gradient.

At smaller delays, the density gradient is steep, the Debye length is smaller, and hence the number of heavy particles involved in the process is reduced.

Even though the longest pulse durations in the single pulse measurements were close in length to the optimal delay time, the observed change in yield was larger with the dedicated pre-pulse. Therefore, not only the time frame in which the fluence is delivered is important, but also the distribution. In these measurements, a well defined pre-pulse was more favorable, as the interrupted energy flux leaves time for the plasma to thermalize and recover charge neutrality.

4.5 The charge state distribution

Note that, throughout the results presented thus far (Figure 4.6, Figure 4.7), the average ionization stayed constant at about $Z_{av} = 2-2.5$.

Additionally, the kinetic energies displayed in Figure 4.5 do not scale linearly with the particle charge. As already stated, theories involving an electric field and constant charges fail to explain this occurrence.

Particle in cell simulations run with the EPOCH code [153] demonstrated that the short pulse used in the z-scan is strong enough to almost fully ionize the carbon plasma, and even in the defocused position mostly C^{3+} and C^{4+} are generated. This, and the fact that **A**mmosov-**D**elone-

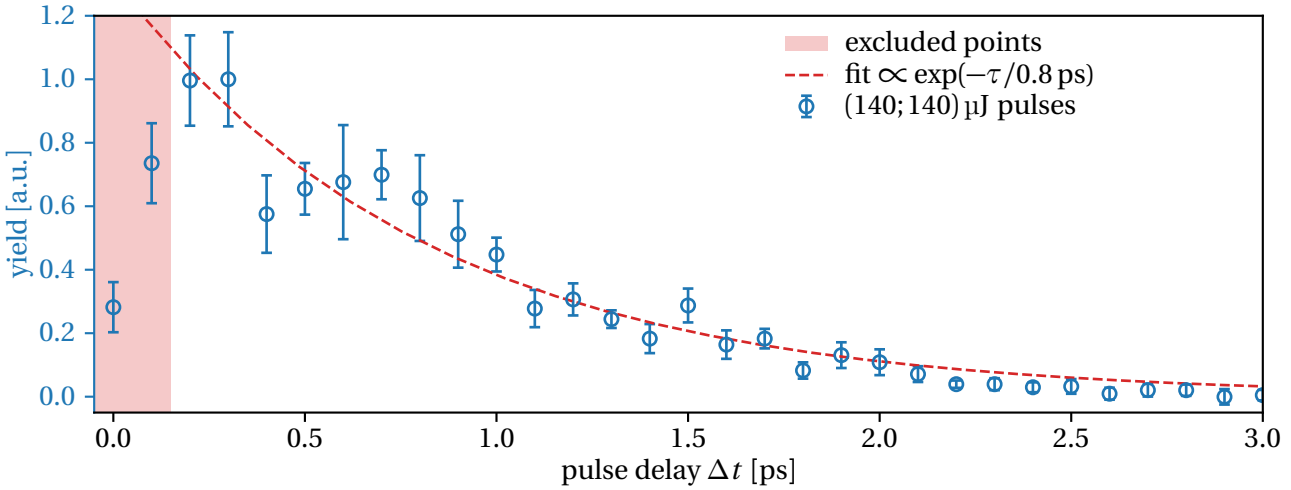

Figure 4.9: Ion yield for varying pulse delays at a fluence of 50 J cm^{-2} per pulse. The first two points were omitted from the fit.

Krainov (ADK) theory scales with the laser's electric field cubed [154], suggest that the CSD's origin is not field ionization.

In a dense plasma, the free electrons thermally relax on time scales in the range of tens to hundreds times the plasma period $1/\omega_{p,s}$ [40, 41]. This translates to times of only tens of femtoseconds for close to critical density plasma. After picoseconds, the heavy particles are in thermal equilibrium as well [42, 43].

As the ion charge state distribution (CSD) is mostly determined by the electronic subsystem, thermal relaxation affects the emission in terms of kinetic energy, as well as ion species and fast neutrals. This suggests that the particles do not have a fixed charge when being accelerated, but rather, constantly exchange charges through ionization and recombination while being accelerated, as is the case in local thermodynamic equilibrium (LTE).

During expansion, the CSD freezes at an effective temperature and effective density, as shown in [47, 45, 46]. This point is like an event horizon, beyond which information about the prevalent plasma conditions is lost.

After this point, the last prevalent plasma conditions can be retrieved according to the method described in section 3.4. Figure 4.10 shows the found temperature and density results of the procedure for the data set measured by variation of the focal position z.

The temperatures range mostly from $10-20$ eV, but close to $z=0$, they drop to about 5 eV. Densities range from $f=10^{-2}-10^{-1}$ times the solid density. Note that all branches are shown, which results in some points with vanishingly small error bars. These are included for reasons of completeness, but their meaningfulness is limited because they occur only for specific heights of the

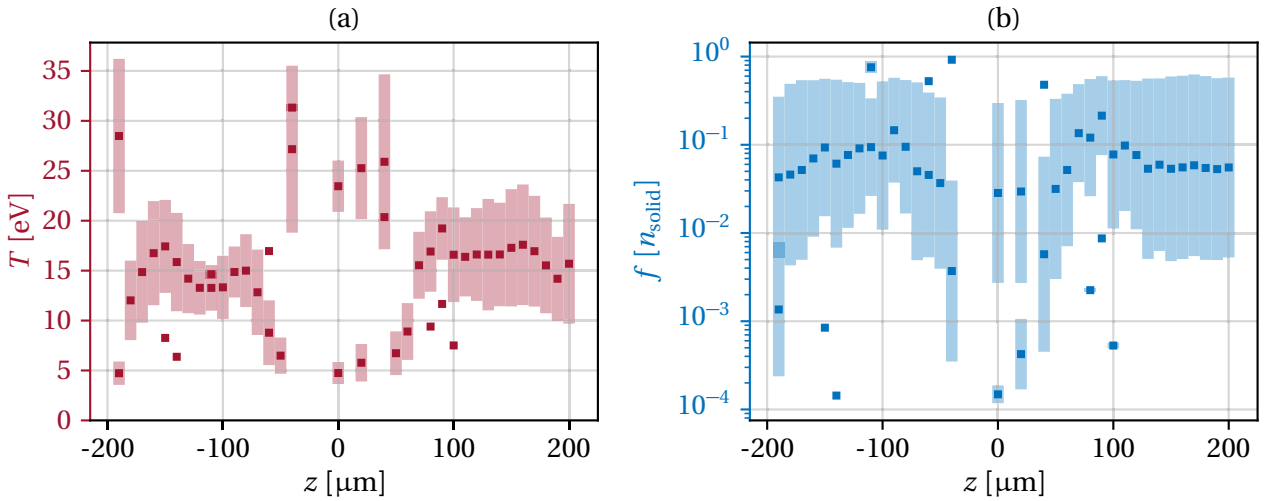

Figure 4.10: Temperatures (a) and densities (b), as found by the CSD analysis, for various focal positions. Multiple data points indicate the different branches. Missing points indicate that no agreement of the measured and Saha CSD was found.

contour line in the (T,n)-plane. Therefore, they are a sort of noise to which this method is prone. In the Appendix 5.8, the same evaluation applied to the spectra measured across various pulse durations can also be found. Figure 4.11 shows the temperatures and densities of the pulse delay measurement, of which the yield was presented in Figure 4.9. While the temperatures are lower, with $4-8$ eV, the densities are similar to the ones of the previous evaluation. The reason for the lower temperature is that $Z_{\mathrm{av}} = 2$ is lower than the average ionization of 2.5 measured in the z-scan. Note that the total fluence, meaning the accumulated fluence of both pulses, falls in the same range as the fluence in the single pulse scenario.

So, the reason behind the lower ionization can be attributed to two effects. The first one is the efficiency of the laser-plasma coupling, and the second one is the volume that is heated. If the coupled energy is spread over more particles, the temperature decreases. Thus, for large pulse delays, where pre-plasma expansion has progressed further, lower temperatures are expected. While barely significant, this effect can be seen in Figure 4.11.

Moving the target closer to the beam waist has a similar effect. The increase in fluence shifts the solid-plasma transition further away from the pulse center. Therefore, the mass density can expand longer before the acceleration is driven. What is different, in this scenario is that the power is constantly applied from the phase transition to the pulse peak. This might lead to zones depleted of electrons due to ponderomotive forces, and consequently a modulated coupling efficiency.

Similar effects become apparent in Figure 4.12 (c). There, the results of a pre-pulse delay scan are

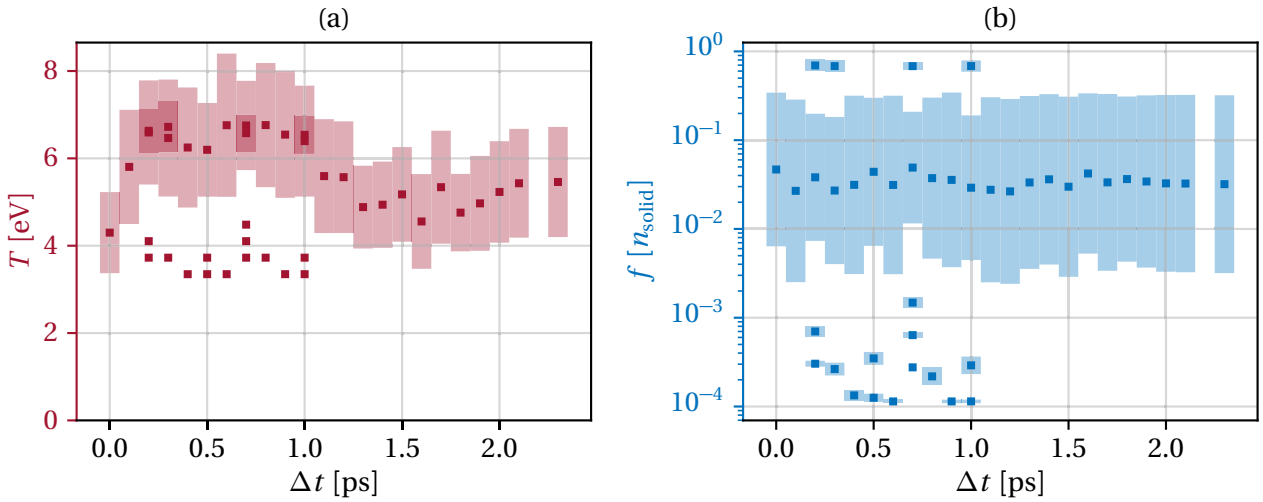

Figure 4.11: Temperatures (a) and densities (b), as found by the CSD analysis for various double-pulse delays. Multiple data points indicate the different branches. Missing points indicate no agreement of the measured and Saha CSD was found.

presented for multiple z-positions. A too defocused laser still yields a high average ionization, but subpar yield. An ideal z-position yields the highest ionization and yield and kinetic energy, while a smaller focal spot creates the same kinetic energy but less yield and average ionization.

4.6 The kinetic energies

From the presented data, aspects of the physics behind the acceleration can be discussed. One crucial point of discussion is the type of accelerating potential. As there are multiple mechanisms that explain supra-thermal energies, they are elaborated on in the following with respect to the findings.

Skin-layer ponderomotive acceleration (S-LPA) [155, 93, 156] is one of these mechanisms. Here, a laser pulse of sub-relativistic intensity interacts with a pre-plasma that has a nonlinear density gradient that is steep at the target and flat on the vacuum side.

The energy density rises with the increasing plasma density until it drops to zero on the high density side of the critical density. This drop occurs on a length scale similar to the Debye length, hence the name referring to a skin-layer.

Ponderomotive forces then drive two electron blocks apart: One that propagates into the target and one that escapes it. Afterwards, the ions follow the electrons due to attractive electric fields. Additionally, a zone depleted of electrons is formed, in which the ions repel themselves, similar to a Coulomb explosion [95, 157, 158, 94]. However, in proximity to the critical density is also

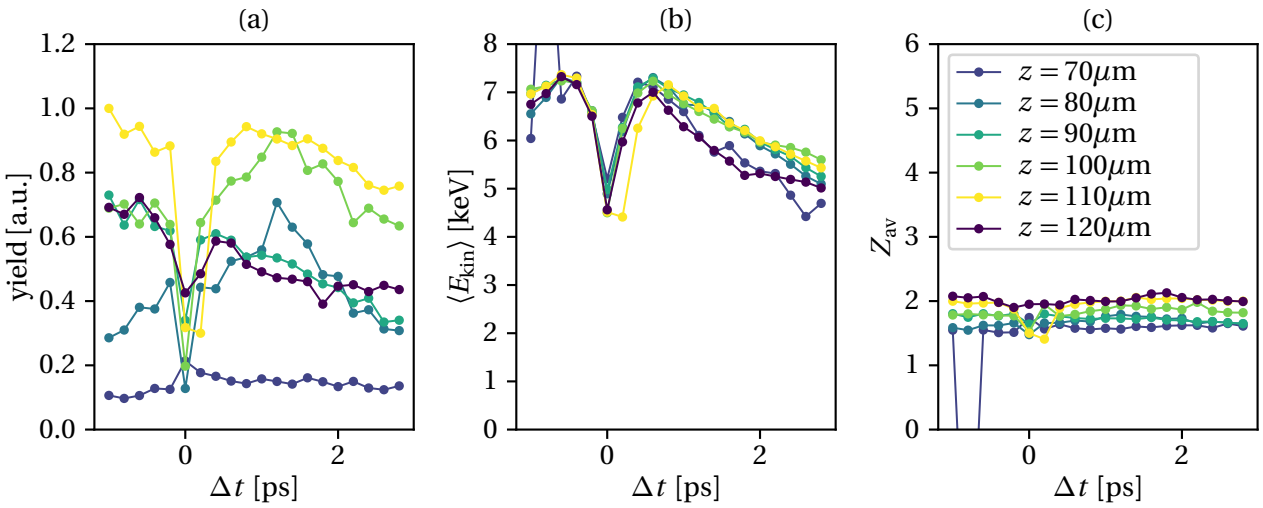

Figure 4.12: (a) Yield, (b) mean kinetic energy, and (c) average ion charge state for different pulse delays and focal positions (z).

where adsorption is the strongest. This leads to a locally heated plasma, which is confined by the surrounding colder plasma. The resulting thermokinetic forces, due to the increase in pressure, additionally drive the heavy particles in this volume apart.

Therefore, to fully describe the acceleration mechanism, a compound of thermo-, hydro-, and electrodynamic problems in three dimensions must be solved. However, with some considerations, the dominant mechanisms can be found.

By the means of classical mechanics, the time t_{acc} it takes for the ions of mass m and charge Z_{av} to gain the kinetic energy $\langle E_{kin} \rangle$ in an electric field of strength E_L can be estimated by

$$t_{acc} = \frac{\sqrt{2\langle E_{kin} \rangle m}}{Z_{av} E_L} \quad . \tag{4.5}$$

For an optimistic estimate, $E_L \approx 10^{11}\,\mathrm{V\,m^{-1}}$ can be chosen. This is about the average of the laser's absolute electric field. Inserting $Z_{av} = 2.5e$ and $\langle E_{kin} \rangle = 6\,\mathrm{keV}$ as measured, $t_{acc} = 150\,\mathrm{fs}$ is found. Even in this optimistic calculation, the result is about a magnitude larger than the laser pulse duration. Hence, the only way electrodynamic acceleration reaches these energies is if an electric field stronger than the one of the laser is sustained for longer than the pulse duration.

Because the plasma frequency ω_p is about half of a femtosecond at the critical density, a possible electrostatic field cannot extend the laser interaction by the required time.

In an attempt to rule out direct acceleration by the laser field, measurements with three different polarizations were performed. Figure 4.13 shows the ion yield (a) and Z_{av} (b) for these polarizations, which are further described in appendix fig. 5.9. As shown, the polarization does not vastly alter either parameter, which leads to the conclusion that coherent field effects are indeed not

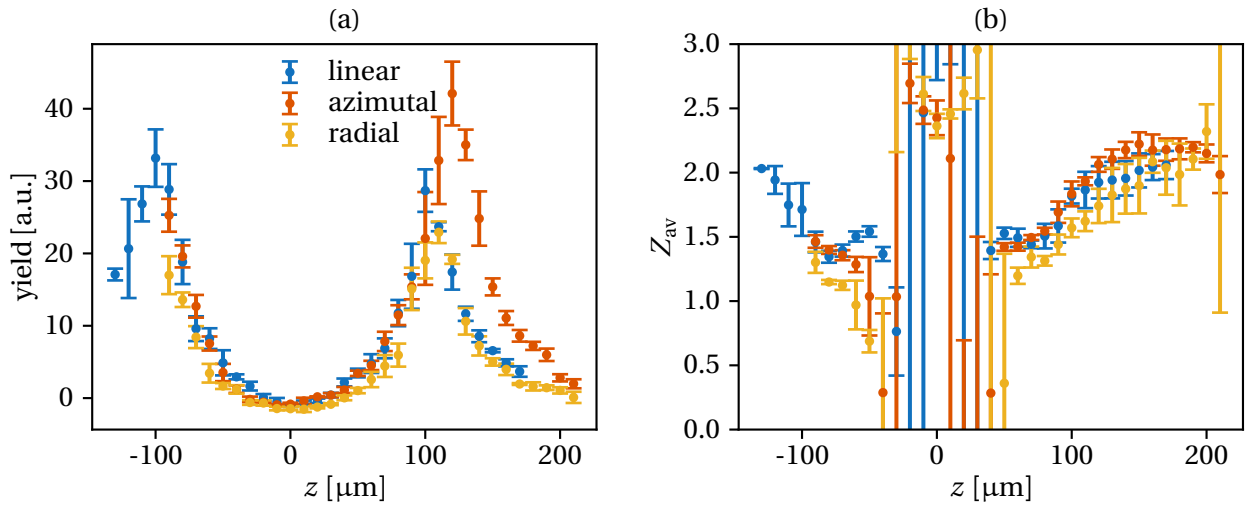

Figure 4.13: (a) Yield of the different types of polarization for various focal positions, and (b) the corresponding average charges.

the main driving factor.

While it is possible that electrons are accelerated to 10 keV, due to their low inertia, it is impossible that ions are dragged behind. In a plasma, the number of electrons per volume is $n_e = Z_{\text{av}} n_h$. But the mass density is lower by a factor $Z_{\text{av}} m_e / m_h$, which is approximately 10^{-4} in the case of carbon. Without continuous pumping of energy, as is the case in TNSA, an electron either leaves the plasma if it has sufficient amounts of kinetic energy, or it rebounds at the potential walls created by the ion cloud.

Therefore, ion acceleration due to pulling electrons can only dominate if the pulse duration is long enough to drive the ambipolar layer until the ions are ejected. In this case, a short ion burst of pulse duration, and kinetic energy

$$E_{\text{SLPA}} \approx 0.93 \cdot 10^{-16} s z I \lambda^2 \quad , \tag{4.6}$$

is generated [19]. Here, $s = 1/n - 1$ is a factor accounting for dielectric swelling with the plasma refractive index n.

As supported by the data, the kinetic energy of the supra-thermal ions does not scale like that. However, it might explain the increase in yield and kinetic energy if the pulse is stretched as in Figure 4.7 (b). As the pulse approaches the picosecond regime, a driving electric field is sustained for longer, in addition to the regardless present thermokinetic forces. Thus, more particles are caught in the field, and electrodynamic forces contribute more to the energy.

Another mechanism was studied by [37]. In this scheme, charge displacement in a plasma of finite thickness and density gradient l_{ss} leads to an accelerating electric field, which evolves over

time. The velocity of the ions increases logarithmically over timescales of $10-100\omega_{p,i}$. Assuming adiabatic expansion, the final velocities are multiples of the ion sound velocity

$$v_{c,i} = \sqrt{\frac{k_b T}{m_h}} \quad . \tag{4.7}$$

For now, neither T nor the initial plasma gradient are known, which prevents conclusions on whether this is indeed the mechanism at play.

4.7 Layered targets

Further insight into the origin of the supra-thermal particles can be gained by the use of layer targets. In vacuum, trace gases in the vacuum, mainly due to residual water and carbohydrates, form a thin layer on metallic surfaces.
As they consist of hydrogen, carbon, and oxygen, they have a much lower Z-number compared to many metals. This leads to different properties, which can be used in a comparison to the previously studied carbon material.
Electro-dynamically, a key difference is that higher Z materials offer a higher degree of ionization at the same temperature and density. In addition, the mass density gradient is naturally higher due to the larger initial density. Because the total number of electrons (bound and unbound) per unit volume is proportional to the mass density for most materials, stronger accelerating fields, due to steeper gradients in the charge density, can be achieved.
Hydro-dynamically, the inertia is larger as well, which is counterproductive in short-lived accelerating fields, but beneficial in repulsive interactions between the surface layer and bulk.
To study these compound effects a solid tungsten target with a vacuum-grown layer was tested. The results for a 5.5 fs, 2 J cm^{-2} and 180 J cm^{-2} pulse-pair, with a delay of 2 ps, are shown in Figure 4.14. The pulse duration was 5.5 fs, and In the case of tungsten emission itself ($m_W = 15.32 m_C$), almost vertical parabolas are expected. As shown in (a), they are missing which leads to the conclusion that W is too inert.
However, oxygen is present from O^{1+} to O^{6+}. This indicates, that the ejected particles come from the outer domain of the plasma.
Compared to the solid carbon measurements, two main differences stand out. First, there is about one order of magnitude fewer signal (0.4 µPSL/keV versus 0.2 µPSL/keV), since the layer thickness is expected to be only a couple of nm.
The other one is that the kinetic energies are three times as high as previously ($\sim$ 10 keV versus $\sim$ 30 keV). With the solid tungsten background, the oxygen particles have an "immovable" wall

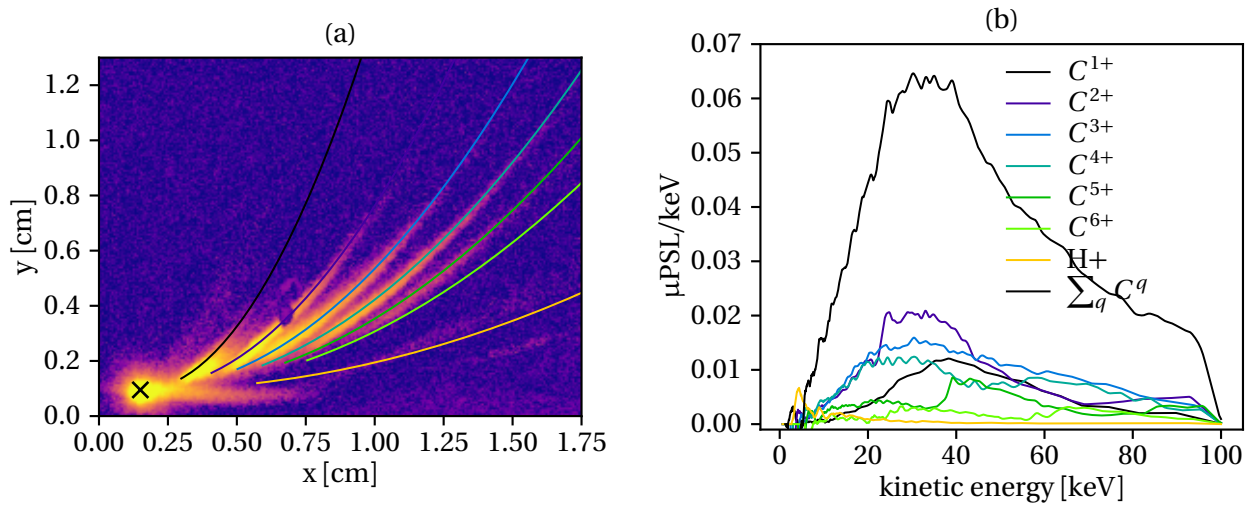

Figure 4.14: (a) TPS trace of carbon ions accelerated from a tungsten target. (b) Carbon spectra as measured with the carbon-tungsten target.

they can push off of. Thus, impulse conservation and therefore thermokinetic forces seem to be one limiting factor for the achievable kinetic energies.
Interestingly, the spectrum is broad, even though the oxygen layer is initially thin and at a well defined position.

4.8 Hydrodynamic simulations

In order to gain more information about the validity of early LTE, the next section tackles the plasma and pre-plasma development from the simulation side with the MULTI-FS code [52]. MULTI-FS is a one dimensional, two-fluid hydrodynamic code tailored to laser plasma interaction of femto- and picosecond time scales, for intensities from $10^{11}\,\mathrm{W\,cm^{-2}}$ to $10^{17}\,\mathrm{W\,cm^{-2}}$. While it was used in literature for single-pulse studies [79], for the here shown results, the code was extended by the ability to include double pulses. They were implemented as to have a modified Gaussian shape [52]:

$$I(t) = \frac{I_{\max}}{C_1}\Phi\left(\frac{t}{t_{\max}-\Delta t}\right)\exp\left(-C_2\frac{(t-t_{\max})^2}{\Delta t^2}\right) \quad , \tag{4.8}$$

with $\Phi(t) = \{t, \text{for } t \le 1; \text{and } 1, \text{for } t \ge 1\}$, $C_1 = \sqrt{\pi/4\ln 2}$, and $C_2 = 4\ln 2$. With this definition, the total pulse fluence can be easily calculated by $I_{\max}\cdot\Delta t$.
Multi-fs uses tabulated matter properties for the **e**quation **o**f **s**tate (EOS), **i**nverted **e**quation **o**f **s**tate (iEOS), Planck and Rosseland opacities [159], emissivities, and ionization. By default, the

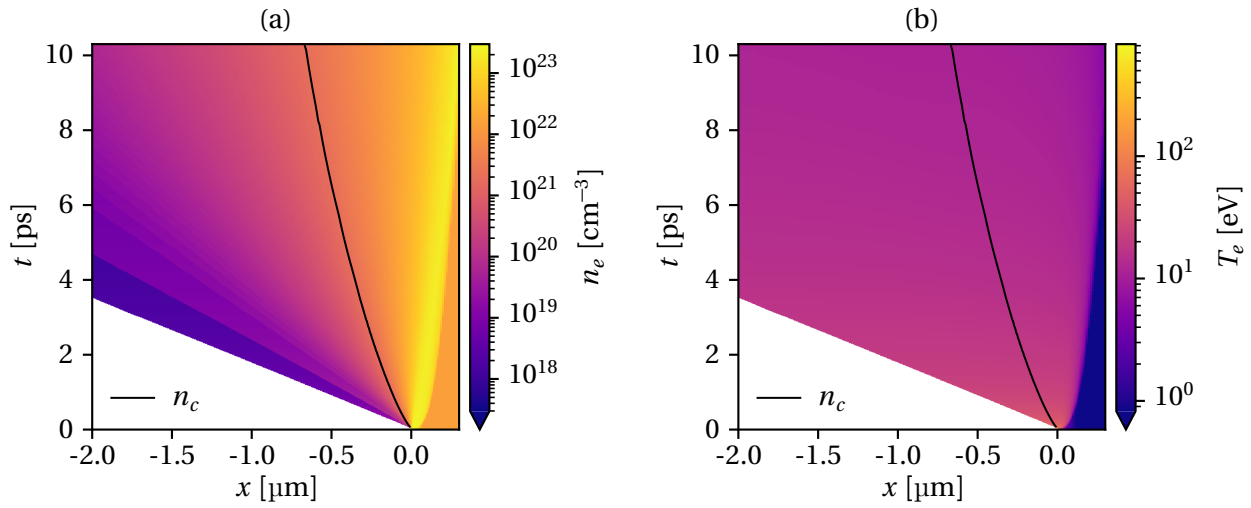

Figure 4.15: (a) Electron density n_e and (b) electron temperature T_e in the simulation volume over time. In both parts, the trajectory of the critical density was drawn.

code comes with values for aluminum. However the atomic mass, and Z-number can be selected.

A good approximation for the heavy particle EOS for most temperatures and densities is the one of an ideal plasma. In this case, the EOS is material independent, which is assumed to hold for up to solid densities.

In terms of the electron EOS, the default tabulated values were used.

To obtain the correct degree of ionization, which further affects thermodynamic properties, the ionization tables were changed according to the Saha solutions. A comparison of the default aluminum table with the new carbon table is shown in the appendix in Figure 5.4.

The opacity values can be found in the NIST FFAST [160], XCOM [161], XAAMDI [162], and Henke [163] databases. Even though energy transport by radiation is small compared to collisions in these types of plasma [52], the Rosseland and Planck opacities were changed to carbon using the extinction coefficients from FFAST. It should be noted that FFAST does not include some necessary single digit eV photon energies, which were extrapolated by the last known value on the soft side, instead. A comparison of the tables and the mass attenuation constants is listed in the appendix Figure 5.5,Figure 5.6, and Figure 5.7.

Plasma friction can be modeled by the Drude-Sommerfeld model, classical plasma model or electron-phonon interactions. For the results presented here, the Drude model was used.

The plasma is treated in 220 Lagrangian cells of exponentially increasing size along x (see chapter 5 for a more detailed explanation of the grid). For each cell, the simulations include spatial and temporal information about electron and ion temperatures, as well as the average ioniza-

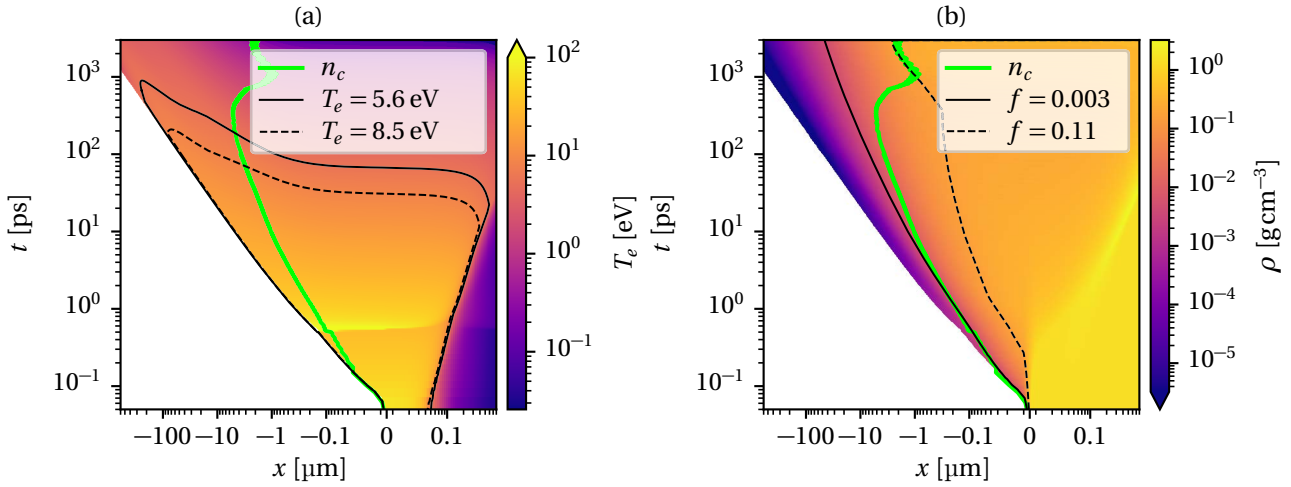

Figure 4.16: Results of the double-pulse simulation in MULTI-FS in terms of (a) temperature and (b) density. The contour lines show the results of the Saha solution found by analyzing the CSD.

tion. Since this is a hydrodynamic code only, quasi neutrality is preserved at all times, which does not allow for electric fields. The minimal ionization was set to 0.1.

In the following, results are presented for pulses with $\Delta t = 20$ fs duration and $I_{\max} = 2.5{\cdot}10^{15}$ W cm^{-2}, which gives a fluence of 50 J cm^{-2} per pulse. These are realistic on target values when the 50/50 pre-pulse unit is used in a ~ 80 µm defocused position.

Figure 4.15 presents the results of a simulation in which only the pre-pulse with 50 J cm^{-2} was used. This way, the conditions in the realm of interaction during the second pulse can be studied.

Densities $\lesssim 10^{22}$ cm^{-3} expand into the vacuum, while densities $\gtrsim 10^{22}$ cm^{-3} propagate into the bulk as a shock wave. Consequently, right in front of the target, a constant density of $\sim 10^{22}$ cm^{-3} is sustained, while the density gradient softens. To get a better impression of the extent of the plasma when it comes to laser interaction, the critical density is drawn into the maps shown in Figure 4.15 (a) and (b).

The later the post-pulse arrives, the softer the density gradient is. On the other hand, the later the pulse arrives, the higher the mass density is. The reason being that, at earlier times, the average ionization is higher, which allows the plasma to become critical at a lower density.

With falling T_e, the Debye length $\lambda_D \propto \sqrt{T_e}$ becomes smaller, and thereby the number of particles involved in charge perturbations reduces.

While MULTI-FS cannot account for charge separation effects, the following shows results of the double pulse scenario to study how temperature and density evolve from a hydrodynamic point of view. In the previously discussed acceleration mechanisms, the accelerated ions originate

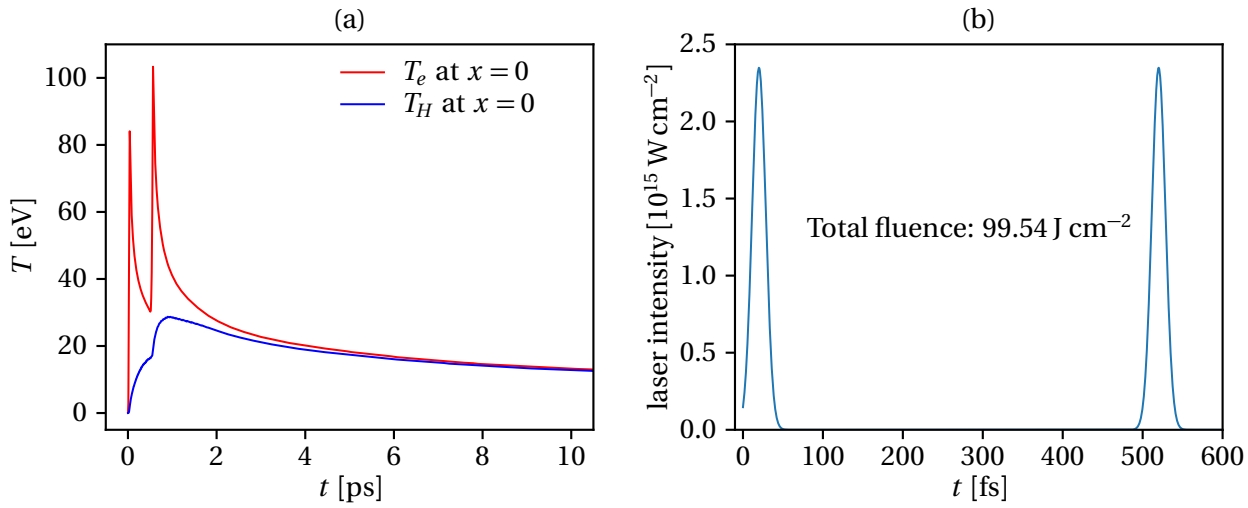

Figure 4.17: (a) Electron and heavy particle temperatures at different times and $x = 0$. (b) Heavy particle density at different times throughout the simulation volume.

from layers buried in pre-plasma, which is traversed upon expansion. So, even though the exact trajectory of the ions possibly cannot be simulated, information about the overall plasma conditions can be derived still. Figure 4.16 shows the results of the pulse sequence with $\Delta t = 0.6$ ps. This time is easily identified by the time where the peak temperature is reached. Note how the temperature is distributed fairly evenly at later times. This becomes apparent by the contour lines, which also represent the temperature results previously found by the Saha method. Part (b) shows the corresponding densities, as simulated and found experimentally.

To find out how electrons and ions compare in temperature, Figure 4.17 (a) and (b) show the same results, but for a discrete position. There, the temperature course is shown at the target surface ($x = 0$) in terms of ions and electrons. While the temperature delta is high right after the pulse hits, close to the target, the temperatures approach each other quickly (0 on the y-axis) due to the high density. Note that, in the outer parts of the plasma, a relatively constant difference in temperature can exist even for longer times. This is due to the low particle densities, which result in slow equilibration. In the dense part, the temperature relaxation occurs on the picosecond time scale due to the high present particle densities.

The double pulse shape that causes this temperature trajectory is shown in part (b). An aspect to highlight is that velocities $v_{\langle E \rangle} \approx 0.3\,\mu\text{m}\,\text{ps}^{-1}$ corresponding to $\langle E_{\text{kin}} \rangle \approx 5$ keV are within the expan-

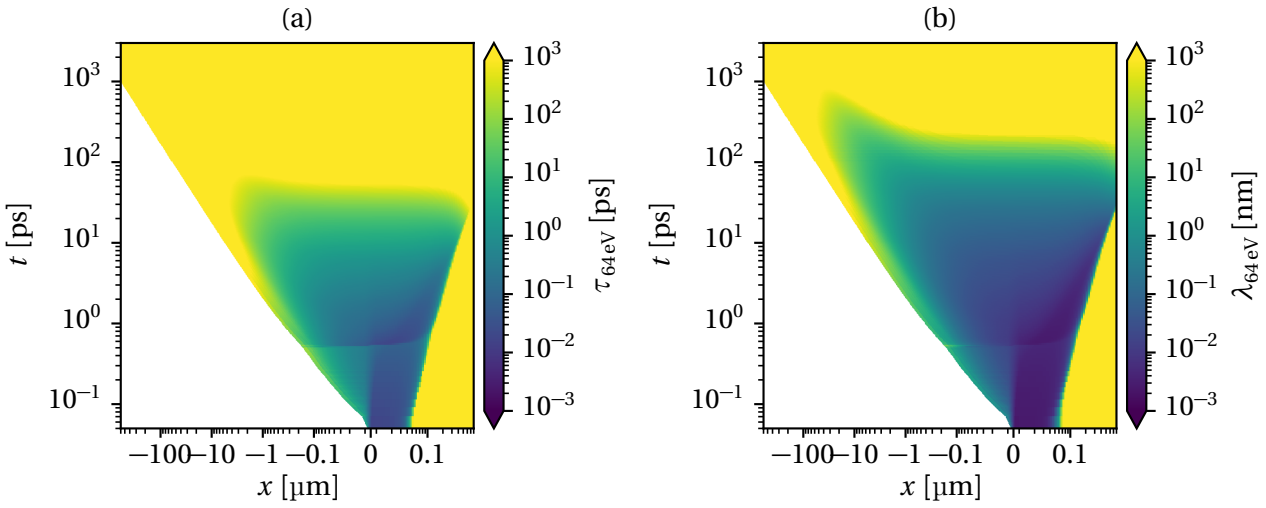

Figure 4.18: Characteristic time (a) and diffusion length (b) of the thermalization for a 64 eV energy gap (about the energy of the $C^{3+} \rightarrow C^{4+}$ transition).

sion speeds after the second pulse strikes the pre-plasma. However, the bimodal characteristic of the spectrum is missing.

As previously stated, MULTI-FS looks up the ionization in tables generated with a Saha solver. This implies that the plasma is always in LTE, which contradicts the assumption that the charge states fall out of LTE and thereby freeze. Therefore, in the following, the LTE conditions are discussed in more detail.

In section 2.2.3, the criteria for LTE were discussed in terms of the diffusion length λ and thermal relaxation time τ_{rel}. Knowledge of the tempo-spatial electron temperature and density now allows one to calculate where freezing likely occurs in the simulation volume. For one, this reveals the limits of the hydrodynamic simulation, but it also enables a comparison with the found (T,n)-values from the measured CSD.

Figure 4.18 shows τ_{rel} (a) and λ (b) over the simulation volume for an energy gap of 64 eV. This is the ionization energy for the $C^{3+} \rightarrow C^{4+}$ transition. As stated by eq. (2.31) and eq. (2.33), these values must be compared to the time and length scale of the T_e and n_e variation.

However, the equations as given initially are not applicable to the MULTI-FS data. On one hand, problems occur because x and t are finite. Thus, a shift in the positional argument can extend past the simulation boundaries.

Another issue comes from the fact that eq. (2.31) and eq. (2.33) only apply to monotonically decreasing shapes of T_e and n_e. Concave or convex temperature and density shapes can satisfy eq. (2.31) and eq. (2.33), even if the rate of change is large.

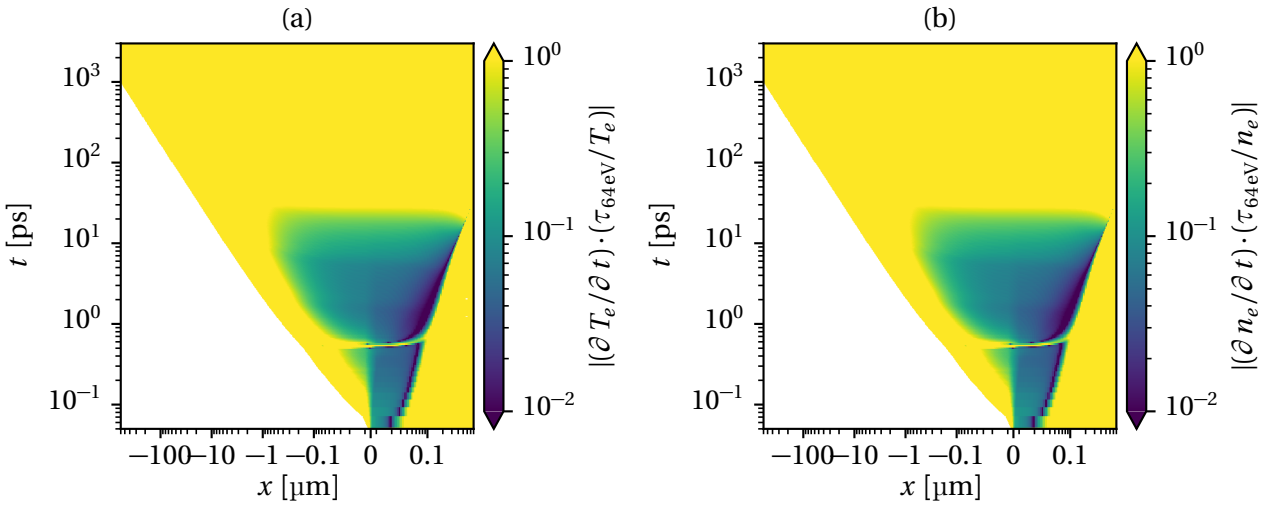

Figure 4.19: Comparison of the relaxation time $\tau_{64\mathrm{eV}}$, with the rate of change in temperature T_e (a) and density n_e (b).

To resolve these downsides, the criteria can be formulated with the help of derivatives. In terms of the rate of change this yields [77]

$$\frac{T_e(t+\tau_{\mathrm{rel},},x)-T_e(t,x)}{T_e(t,x)} \approx \left|\frac{\partial T_e}{\partial t}\frac{\tau_{\mathrm{rel}}}{T_e(t,x)}\right| \ll 1 \tag{4.9}$$

$$\frac{n_e(t+\tau_{\mathrm{rel},},x)-n_e(t,x)}{n_e(t,x)} \approx \left|\frac{\partial n_e}{\partial t}\frac{\tau_{\mathrm{rel}}}{n_e(t,x)}\right| \ll 1 \quad . \tag{4.10}$$

And analogously, in terms of the positional variation

$$\frac{T_e(t,x+\lambda)-T_e(t,x)}{T_e(t,x)} \approx \left|\frac{\partial T_e}{\partial x}\frac{\lambda}{T_e(t,x)}\right| \ll 1 \tag{4.11}$$

$$\frac{n_e(t,x+\lambda)-n_e(t,x)}{n_e(t,x)} \approx \left|\frac{\partial n_e}{\partial x}\frac{\lambda}{n_e(t,x)}\right| \ll 1 \quad . \tag{4.12}$$

Applying these equations to the simulation box for the 64 eV transition then shows where the individual criteria are satisfied. The results are shown in Figure 4.19 and Figure 4.20.
For LTE, all criteria must be satisfied at the same time and position. Thus, taking the product of the inverted criteria compacts all into one equation

$$\begin{aligned}\left[1-\left(1-\left|\frac{\partial T_e}{\partial t}\frac{\tau_{\mathrm{rel}}}{T_e(t,x)}\right|\right)_{>0}\left(1-\left|\frac{\partial n_e}{\partial t}\frac{\tau_{\mathrm{rel}}}{n_e(t,x)}\right|\right)_{>0} \quad \cdots \right. \\ \left.\left(1-\left|\frac{\partial T_e}{\partial x}\frac{\lambda}{n_e(t,x)}\right|\right)_{>0}\left(1-\left|\frac{\partial T_e}{\partial x}\frac{\lambda}{n_e(t,x)}\right|\right)_{>0}\right] \ll 1.\end{aligned} \tag{4.13}$$

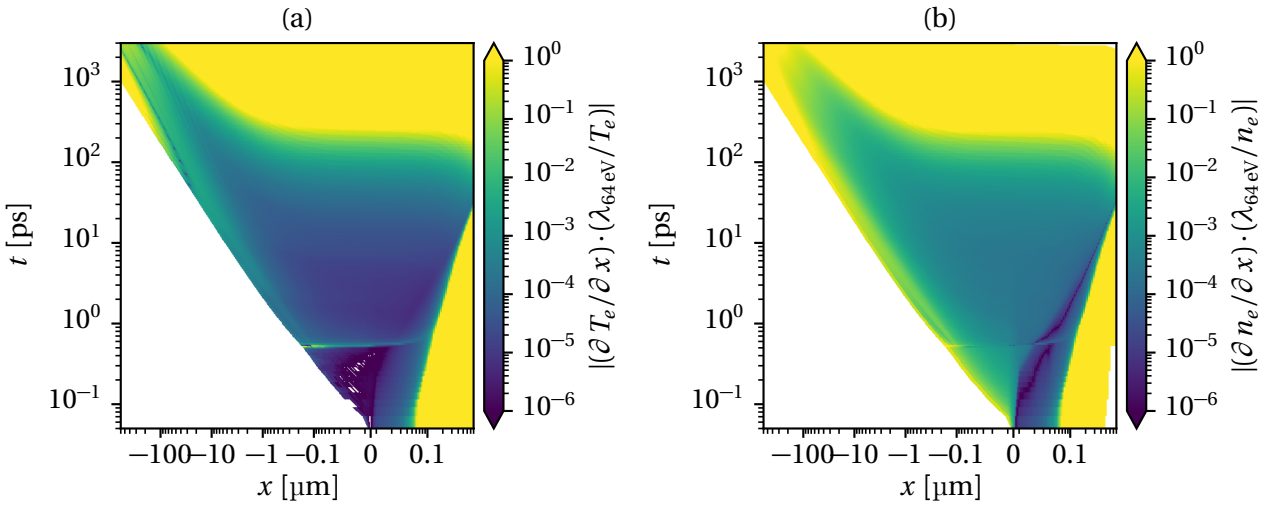

Figure 4.20: Comparison of the diffusion length λ, with the slope of the temperature T_e (a) and density n_e (b).

Since the terms in the inner bracket might be negative (LTE unlikely), these terms are truncated to only involve numbers greater than zero. This must be done because otherwise, an even number of negative terms might yield a positive number close to one, which may result in the criteria being satisfied.

Figure 4.21 (a) displays the topography of this equation applied to the MULTI-FS data. A value close to one on the color-scale means an LTE is less likely, while values close to zero indicate a high probability. For (b), the map from (a) was recalculated for a set of energy transitions ΔE. The graphs, showing the outline of the shape measured with contour lines of height 0.1, represent the different times and positions these transitions fall out of LTE. At this line height, each criterion in eq. (4.10) and eq. (4.12) is satisfied by at least one order of magnitude ($0.1 < 1 - 0.9^4 \approx 0.34$). This means, strictly speaking, that the simulation, or at least the ionization states, are valid only within these boundaries, depending on the highest occurring species.

This result may seem counterintuitive, as one might assume that the more time the plasma has to equilibrate, the more likely LTE becomes. Whereas the opposite is true, and the LTE conditions get worse over time in an expanding plasma. Along x, the contour lines stay close together until the time one transition leaves the LTE.

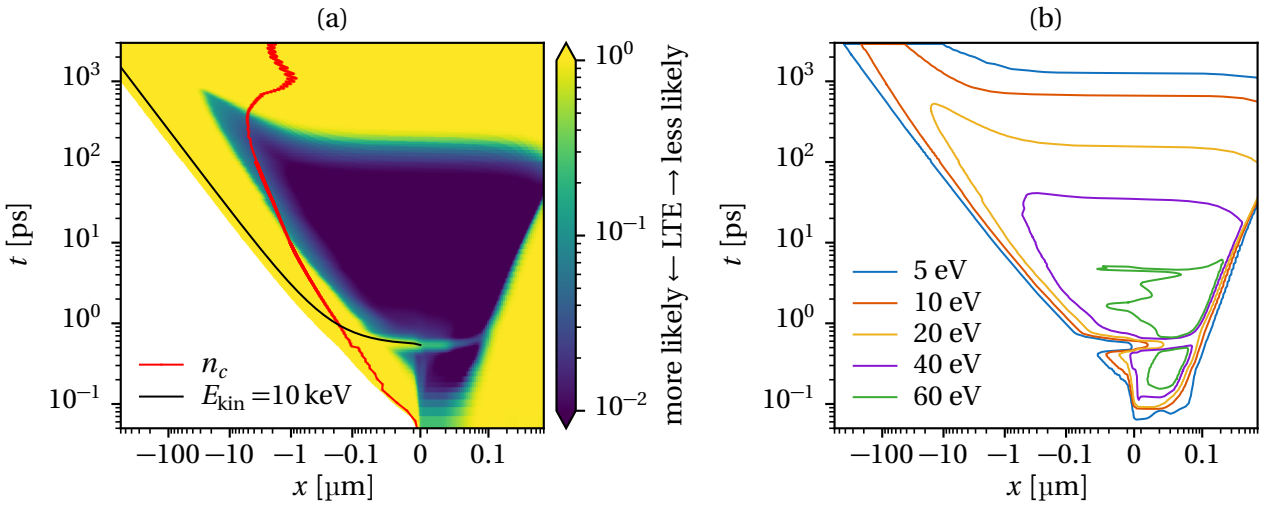

Figure 4.21: (a) Likelihood the plasma is in LTE according to the compound criterion given in eq. (4.13) for $\Delta E = 20\,\text{eV}$. (b) Map of the times and positions in plasma where different energy transitions fall out of LTE, measured with contour lines of height 0.1 .

4.9 Freezing simulation

With the results from the hydrodynamic simulations, it is possible to simulate the freezing process. Thus, the model of instantaneous freezing can be studied in more detail. Additionally, this simulation can be used to make predictions of the charge state and study the plasma expansion in the process.

For this purpose, an exponentially decaying heavy particle density is assumed

$$n(x) = n_0 \exp\left(-\frac{x}{\xi}\right) \quad . \tag{4.14}$$

Then, a "velocity" v is assumed with which a test particle runs through these states. Note that this can be interpreted in two ways. One would be that the test particle propagates through a plasma of decaying density, with said velocity. The other one is that the outermost layer of the plasma, which sits initially at n_0, moves away from the target and thereby experiences a decay in density. In this interpretation, the test particle is co-propagating with this layer, which moves with v through the series of states.

During expansion (thinning of the density), the temperature change is assumed to be polytropic

$$T' = T\left(\frac{n}{n'}\right)^{1-\kappa}, \tag{4.15}$$

with an exponent $0 \leq \kappa \sim 5/3 \leq \infty$. This was done to add an additional degree of freedom. The expansion can be (beyond) isothermal ($\kappa \sim 1$) if heat from the dense and hot part of the plasma

diffuses outside faster than the particle propagates. However, if losses due to radiation prevail, it can also be above adiabatic ($\kappa \geq 5/3$).
Now, an initial temperature T_0, and density n_0 combination is defined. These values are then used to compute an initial CSD, with a mean ionization of Z_{av}, according to the Saha solver.
With the Z_{av}, the time between collisions τ can be approximated by Spitzer collisions eq. (2.27). Together with v, this is used to calculate the mean free path $\lambda_{\text{free}} = v\tau$. It is further assumed that, at each interval λ_{free}, the test particle thermalizes. Another point of concern is that ionization and recombination violate particle conservation. This is handled by assuming a constant internal energy. Therefore, each change in ionization also changes the temperature

$$T' = \frac{n_e + n_h}{n'_e + n'_h} T \quad . \tag{4.16}$$

Since this changes the average ionization again, T' and Z_{av} are computed iteratively. Note that a constant inner energy barely affects the overall results because the fraction in eq. (4.16) is close to one. With these equations, the simulation cycles through the following steps:

1. Calculate $n_h(x) = n_0 \exp\left(-\frac{x}{\xi}\right)$
2. Iteratively calculate:
   a) $n_e(x)$ with Saha, and $N(x) = n_e(x) + n_h(x)$
   b) $T(x)$, and n_e according to isotropic equation, and conservation of the inner energy
3. Calculate $\lambda_{\text{free}} = \tau \cdot v$
4. $x = x + \mathrm{d}x$, with $\mathrm{d}x \ll \xi$; return to 1.

Using the MULTI-FS results: $T \approx 1\,\text{keV}$, $n_0 = 7.1 \cdot 10^{28}\,\text{cm}^{-3}$, $\xi = 10\,\text{nm}$, and $\kappa = 1.5$, $v = \sqrt{2 \cdot 10\,\text{keV}/12\,\text{u}}$, yields the results shown in Figure 4.22. Part (a) shows the test particle position x, and the corresponding mean free paths in addition to x, as calculated according to eq. (2.27) and eq. (2.28). In addition, the dashed lines represents the position of the TPS. The term $\lambda + x$ is dominated by x for positions $x/\xi \lesssim 10$, until the mean free path rapidly increases. This means that where $x < \lambda$, an ion is likely never colliding with an electron again. Therefore, this is the region where freezing of the CSD occurs. Part (b) shows the temperature and average ionization for each position, and (c) the electron and heavy particle densities. By defining the point of freezing as $\lambda = x$, a freezing temperature T_{fr} and density n_{fr} can be found. It is apparent that high energy transitions leave the LTE sooner than lower ones, as was shown by the hydrodynamic simulations. However, the difference between $\lambda_{60eV} = x$, and $\lambda_{10eV} = x$ is almost 2ξ,

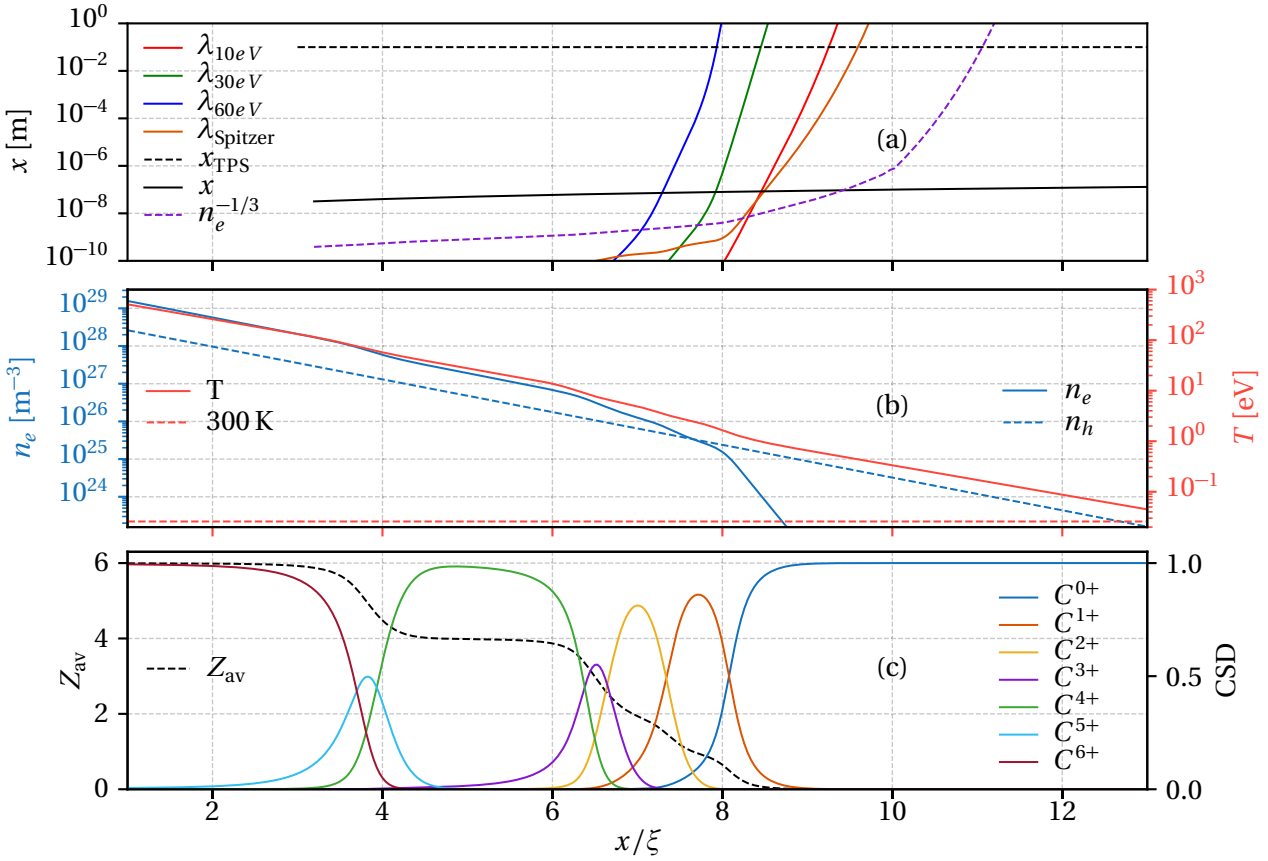

Figure 4.22: (a) Mean free path λ, test particle position x, mean inter-electron distance $n_e^{-1/3}$, and position of the TPS. (b) Heavy particle n_h density, electron density n_e, as well as the temperature T along x/ξ. (c) Average ionization Z_{av} (black dashed line), and CSD at the different positions. Here, $\kappa = 5/3$ was used.

which means the temperature and density difference at the point of freezing is about one order of magnitude.

Figure 4.23 shows the results for polytropic exponents in the range of $0.5 \leq \kappa \leq 3$, if $\lambda_{60eV} > x$ is the freezing criterion. The horizontal lines represent the range of temperatures and densities found by the Saha evaluation of the measured CSDs of the double pulse experiment. Note that $\Delta E = 60\,\text{eV}$ was chosen because for $\Delta E = 10\,\text{eV}$, the freezing temperatures are too low to agree with the measurements. This might be because eq. (2.28) gives a too low estimate, or the metric $\lambda = x$ is incomplete. Another explanation is that κ is rather not constant during the expansion. This is not a perfect assumption, considering n_e dictates the heat conductivity of the plasma, while T causes energy loss by black-body radiation according to the Stefan-Boltzmann law. However, for λ_{60eV} the computed and measured results agree in the area of $\kappa \gtrsim 1.7$, even though the temperature agreement is not optimal. It should be noted that in the z-scan measurement,

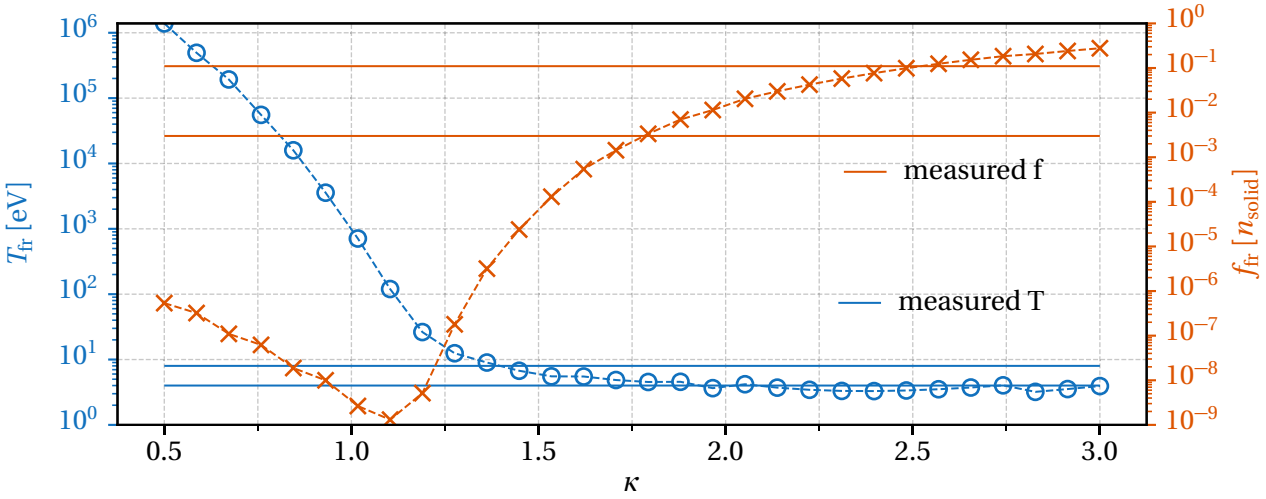

Figure 4.23: Freezing temperature and density for different polytropic exponents κ. T_0 was set to 1 keV, and $n_0 = n_{solid}$.

experimental temperatures of ~ 10 eV and densities $f \sim 10^{-2}$ were found. In other words, both parameters are higher, even though freezing occurs at either high T, low f, or high f, low T. These high (T,n) are not covered by fig. 4.23.

One possible explanation is that the simulation fails if T_0 is too high and/or n_e too small in relation to ξ. $T_0 = 2$ keV, $n_0 = 3 \cdot 10^{-3}\, n_{solid}$, $\xi = 10$ nm is one example. In this instance, $x < \lambda_{Spitzer}$ at all positions x. Therefore, freezing would occur at the initial conditions if $\lambda_{Spitzer}$ is considered as the freezing criterion. In these cases, whether $\lambda_{Spitzer}$ intersects x depends on ξ (ξ vertically shifts x in Figure 4.22 (a)). Exploiting this, a scenario where the high freezing temperature and density of the z-scan measurements are met can be fabricated. While this is a questionable procedure, it points out that these high (T,n) combinations are not entirely implausible. Another explanation is that the interaction of a fs-laser pulse with a step-like density gradient of a solid is not covered by the assumptions made here, as in this case $\xi \to 0$. If such a step is introduced to $n(x)$, freezing always occurs at the conditions present at the verge of this step. In the realm of $\xi \sim 10^{-12}$ m, the freezing temperature rises to about $10-15$ eV. Compared to the interatomic distance in a solid ($\sim$ Å), this value is unreasonably small. Thus, this simulation is only valid if the density gradient can be sufficiently approximated by an exponential decay. If this is the case, freezing always sets in at $x/\xi \sim 10$ and similar conditions for a large, but reasonable, range of 1 Å $\leq \xi \leq 1$ µm.

However, in the well-defined case of the interaction of a main-pulse with a pre-plasma, the chained results of the hydrodynamic and freezing simulations, match the experimental outcome.

Chapter 5

Summary and Conclusion

In this final chapter, the key outcomes of the research are summarized and discussed. It revisits the main research objectives defined in the first chapter and evaluates how they have been achieved. Finally, it offers remarks and highlights potential directions for future research.
One of the first steps was developing a TPS to examine the supra-thermal ions in terms of species and kinetic energies. For this purpose, the most important design cues were first defined and then followed to develop the specialized TPS. Because in this development, not only the E-field, but also the B-field can be varied over a wide range, the previously unknown and broadband ion emission could be accurately characterized. It turned out optimally suited for diagnosing laser-generated ions from bulk or thin-foil targets due to its slim design, which offered enough clearance for surrounding optics. At the same time, it proved to work with different detectors, while being able to maintain optimal use of space on the detector. This led to a low energy uncertainty across the spectrum.
In the experiments, the TPS was used with an image plate detector as well as an MCP detector. The response of which was unknown in the supra-thermal regime. Due to the versatility of the spectrometer, it was possible to examine the behavior of the response function, even without a tunable ion source, by stretching the parabolic traces in a predictable manner. With this procedure, a linear response was found across the present ion energies. Therefore, both detectors could be integrated successfully into the TPS to determine ion spectra from an ultra-short pulse laser plasma.
With this tool, it was demonstrated which the driving factors behind the supra-thermal ion emission are in the sub $10^{18}\,\mathrm{W\,cm^{-2}}$ regime. For this, single-pulse parameter scans with varying fluence, intensity, and spot size were performed on a glassy carbon target.
It was found that, for pulse durations $< 200\,\mathrm{fs}$, the fluence is the main driving factor behind the

supra-thermal emission. For the tested laser and glassy carbon target, a fluence $\sim 100\,\mathrm{J\,cm^{-2}}$ was found ideal in terms of yield. Without a dedicated pre-pulse for the initial ignition, this value is expected to result in pre-plasma development at the right time relative to pulse peak.
To also examine the pre-plasma conditions, a double-pulse setup was introduced. This allowed for variable delays between the pre-plasma ignition and post-pulse. With this setup, it was found that a proper pre-plasma development is crucial for the yield. By letting the pre-plasma self-develop on picosecond timescales before the main interaction, the yield could be tuned for a constant total fluence. At an optimal delay of $0.2-0.3$ ps, the yield was increased by a factor of about three. Therefore, defocusing the laser in combination with a double pulse sequence is an efficient way to optimize the ion yield at a given pulse energy. In total, pre-plasma timing, as well as the fluence, had the most impact on the yield. However, the ~ 10 keV kinetic energies and average ionization of about $2.0-2.5$ remained mostly unaffected, even if the laser polarization was altered. Only by employing a layered target, the kinetic energies could be increased by about a factor of three to ~ 30 keV. These findings lead to the conclusion that hydrodynamic acceleration processes are likely to dominate over field driven ones.
Further, it was found that the CSD is likely determined by the LTE conditions. To explore the LTE conditions in ultra-short pulse solid-laser interactions and the consequences for supra-thermal ion emission, considerations involving different LTE criteria were made. It was found that, in close to critical density plasma, they are easily satisfied in combination with a high Spitzer collisional frequency. Assuming local thermodynamic equilibrium during acceleration, and up to a certain point in the ejection process, it was demonstrated how the species distribution of the ions can be analyzed by solving the Saha equations. For this purpose, a known Saha solver was improved by shifting the calculations to the log-space, which allows for computation of high degrees of ionization, even for high Z materials. The involved partition functions of the materials were taken from the NIST database. This way, together with the plasma-appropriate ionization potential depression, the species distribution for a large range of plasma parameters could be calculated.
It was demonstrated how the freezing process, and the corresponding charge state distribution, can be exploited to recover the plasma conditions in the realm of ionization freezing. The frozen species composition of the accelerated ions allow for insights into an early and dense phase of the expanding plasma, which was found to be about a few orders of magnitude below the solid density and in the 5 eV to 15 eV range.
To further evaluate these values, the hydrodynamic two-fluid code MULTI-FS was extended to mimic the experiment. For this purpose, the feature of double-pulses was added to the code, as

well as modifications of the tabulated ionization and opacity maps. The results of the simulation were used for in depth-studies when and where early state plasma is in LTE by comparing the characteristic diffusion length and thermal relaxation time to the plasma dynamics. This revealed that the plasma is indeed in LTE shortly after laser interaction for a significant amount of its spatial extent. As time passes, the LTE conditions worsen across the plasma, until high energy transitions leave the LTE because the expansion leads to a reduction in overall density. Until about ~ 10 ps, energy gaps up to $\Delta E = 40$ eV are in equilibrium, which is similar to the $C^{2+} \rightarrow C^{3+}$ transition.

As suspected, different energy transitions drop out of LTE close to each other at the plasma vacuum interface. Hence, the model of instantaneous freezing is supported by these findings, if ejection occurs sufficiently early.

The results from the hydrodynamic simulations were used as input parameters for a novel freezing simulation, which assumes polytropic expansion of the plasma. Based on this combination, a polytropic exponent larger than the adiabatic value was found to predict the plasma expansion best, as this yields similar freezing conditions as found by the CSD measurements. Considering the energy losses due to radiation are high during the early and hot phase of the plasma, an exponent above adiabatic seems reasonable. According to this model, freezing always occurs at similar conditions for a given polytropic exponent, which explains why the average ionization remained nearly constant in the measurements.

The understanding of the charge states, yield, and kinetic energies are crucial challenges in creating feasible laser-solid particle sources. For the tested fluences, it was demonstrated that this type of supra-thermal emission is limited by thermodynamic properties of the plasma during expansion. Because the charge state distribution freezes during the ejection according to the plasma density and temperature, emission consisting of a high average ionization or single ionization states are suppressed. Since the kinetic energy was found to scale mostly with the target structure, special targets are a promising approach to increase the kinetic energy further [164]. With further exploration of the correlation between ion properties and initial position within the target, it might be possible to retrieve particle compositions in a depth-resolved manner simply by measuring the charged resolved spectrum.

Bibliography

[1] Hiroyuki Daido, Mamiko Nishiuchi, and Alexander S Pirozhkov. “Review of laser-driven ion sources and their applications”. In: *Reports on Progress in Physics* 75.5 (Apr. 2012), p. 056401. ISSN: 1361-6633. DOI: 10.1088/0034-4885/75/5/056401.

[2] André Anders. “Plasma and ion sources in large area coating: A review”. In: *Surface and Coatings Technology* 200.5–6 (Nov. 2005), pp. 1893–1906. ISSN: 0257-8972. DOI: 10.1016/j.surfcoat.2005.08.018.

[3] S. Kar et al. “Ion Acceleration in Multispecies Targets Driven by Intense Laser Radiation Pressure”. In: *Physical Review Letters* 109.18 (Nov. 2012), p. 185006. ISSN: 1079-7114. DOI: 10.1103/physrevlett.109.185006.

[4] L. Torrisi. “Coulomb-Boltzmann-Shifted distribution in laser-generated plasmas from 1010 up to 1019 W/cm2intensities”. In: *Radiation Effects and Defects in Solids* 171.1–2 (Feb. 2016), pp. 34–44. ISSN: 1029-4953. DOI: 10.1080/10420150.2016.1155585.

[5] Malay Dalui et al. “Compact acceleration of energetic neutral atoms using high intensity laser-solid interaction”. In: *Scientific Reports* 7.1 (June 2017). ISSN: 2045-2322. DOI: 10.1038/s41598-017-04152-3.

[6] Marek Tulej et al. “Current Progress in Femtosecond Laser Ablation/Ionisation Time-of-Flight Mass Spectrometry”. In: *Applied Sciences* 11.6 (Mar. 2021), p. 2562. ISSN: 2076-3417. DOI: 10.3390/app11062562.

[7] Michael N. R. Ashfold et al. “Pulsed laser ablation and deposition of thin films”. In: *Chemical Society Reviews* 33.1 (2004), p. 23. ISSN: 1460-4744. DOI: 10.1039/b207644f.

[8] Pankaj Chaudhary et al. “Cellular irradiations with laser-driven carbon ions at ultra-high dose rates”. In: *Physics in Medicine & Biology* 68.2 (Jan. 2023), p. 025015. ISSN: 1361-6560. DOI: 10.1088/1361-6560/aca387.

[9] H. M. Ayedh, A. Hallén, and B. G. Svensson. "Elimination of carbon vacancies in 4H-SiC epi-layers by near-surface ion implantation: Influence of the ion species". In: *Journal of Applied Physics* 118.17 (Nov. 2015). ISSN: 1089-7550. DOI: 10.1063/1.4934947.

[10] Xu Wang et al. "Synthesis of ultra-thin carbon layers on SiC substrate by ion implantation". In: *Carbon* 93 (Nov. 2015), pp. 230–241. ISSN: 0008-6223. DOI: 10.1016/j.carbon.2015.05.046.

[11] D.J. Brink, J. Camassel, and J.B. Malherbe. "Formation of a surface SiC layer by carbon-ion implantation into silicon". In: *Thin Solid Films* 449.1–2 (Feb. 2004), pp. 73–79. ISSN: 0040-6090. DOI: 10.1016/j.tsf.2003.10.018.

[12] Jan Riedlinger et al. "Electromagnetic Thomson parabola spectrometer for detection of fs laser-driven keV ions". In: *AIP Advances* 14.8 (Aug. 2024). ISSN: 2158-3226. DOI: 10.1063/5.0212122.

[13] Bernhard Hidding et al. "Progress in Hybrid Plasma Wakefield Acceleration". In: *Photonics* 10.2 (Jan. 2023), p. 99. ISSN: 2304-6732. DOI: 10.3390/photonics10020099.

[14] Malay Dalui et al. "Preferential enhancement of laser-driven carbon ion acceleration from optimized nanostructured surfaces". In: *Scientific Reports* 5.1 (July 2015). ISSN: 2045-2322. DOI: 10.1038/srep11930.

[15] B Qiao et al. "Revisit on ion acceleration mechanisms in solid targets driven by intense laser pulses". In: *Plasma Physics and Controlled Fusion* 61.1 (Nov. 2018), p. 014039. ISSN: 1361-6587. DOI: 10.1088/1361-6587/aaf18e.

[16] Yuji Oishi et al. "Proton Generation by Ultra-Short High-Power Laser and the Dependence on Laser Intensity and Pulse Duration". In: *The Review of Laser Engineering* 31.11 (2003), pp. 747–751. ISSN: 1349-6603. DOI: 10.2184/lsj.31.747.

[17] J. E. Crow, P. L. Auer, and J. E. Allen. "The expansion of a plasma into a vacuum". In: *Journal of Plasma Physics* 14.1 (Aug. 1975), pp. 65–76. ISSN: 1469-7807. DOI: 10.1017/s0022377800025538.

[18] P. Mora. "Plasma Expansion into a Vacuum". In: *Physical Review Letters* 90.18 (May 2003), p. 185002. ISSN: 1079-7114. DOI: 10.1103/physrevlett.90.185002.

[19] J. Badziak et al. "Generation of picosecond high-density ion fluxes by skin-layer laser-plasma interaction". In: *Laser and Particle Beams* 23.2 (June 2005), pp. 143–147. ISSN: 1469-803X. DOI: 10.1017/s0263034605050238.

[20] J. Badziak et al. “Laser-driven generation of high-current ion beams using skin-layer ponderomotive acceleration”. In: *Laser and Particle Beams* 23.4 (Oct. 2005), pp. 401–409. ISSN: 1469-803X. DOI: 10.1017/s0263034605050573.

[21] Y. Sentoku et al. “High energy proton acceleration in interaction of short laser pulse with dense plasma target”. In: *Physics of Plasmas* 10.5 (May 2003), pp. 2009–2015. ISSN: 1089-7674. DOI: 10.1063/1.1556298.

[22] M. Hegelich et al. “MeV Ion Jets from Short-Pulse-Laser Interaction with Thin Foils”. In: *Physical Review Letters* 89.8 (Aug. 2002), p. 085002. ISSN: 1079-7114. DOI: 10.1103/physrevlett.89.085002.

[23] D. Kirby et al. “Radiochromic film spectroscopy of laser-accelerated proton beams using the FLUKA code and dosimetry traceable to primary standards”. In: *Laser and Particle Beams* 29.2 (Apr. 2011), pp. 231–239. ISSN: 1469-803X. DOI: 10.1017/s0263034611000206.

[24] L. Torrisi and A. Torrisi. “Proton acceleration from TiH2 target plasma produced by different pulse laser intensity”. In: *Contributions to Plasma Physics* 63.7 (Apr. 2023). ISSN: 1521-3986. DOI: 10.1002/ctpp.202300024.

[25] M. J. Sadowski et al. “Mass- and energy-analyses of ions from plasma by means of a miniature Thomson spectrometer”. In: *Review of Scientific Instruments* 80.5 (May 2009). ISSN: 1089-7623. DOI: 10.1063/1.3131805.

[26] D. Gwynne et al. “Modified Thomson spectrometer design for high energy, multi-species ion sources”. In: *Review of Scientific Instruments* 85.3 (Mar. 2014). ISSN: 1089-7623. DOI: 10.1063/1.4866021.

[27] Sheroy Tata et al. “A gated Thomson parabola spectrometer for improved ion and neutral atom measurements in intense laser produced plasmas”. In: *Review of Scientific Instruments* 88.8 (Aug. 2017). ISSN: 1089-7623. DOI: 10.1063/1.4998685.

[28] A. Alejo et al. “High resolution Thomson Parabola Spectrometer for full spectral capture of multi-species ion beams”. In: *Review of Scientific Instruments* 87.8 (Aug. 2016). ISSN: 1089-7623. DOI: 10.1063/1.4961028.

[29] S. Sakabe et al. “Modified Thomson parabola ion spectrometer of wide dynamic range”. In: *Review of Scientific Instruments* 51.10 (Oct. 1980), pp. 1314–1315. ISSN: 1089-7623. DOI: 10.1063/1.1136073.

[30] R. Nedbailo et al. “Compact high repetition rate Thomson parabola ion spectrometer”. In: *Review of Scientific Instruments* 94.2 (Feb. 2023). ISSN: 1089-7623. DOI: 10.1063/5.0101859.

[31] J. T. Morrison et al. “Design of and data reduction from compact Thomson parabola spectrometers”. In: *Review of Scientific Instruments* 82.3 (Mar. 2011). ISSN: 1089-7623. DOI: 10.1063/1.3556444.

[32] Sadaoki Kojima et al. “Compact Thomson parabola spectrometer with variability of energy range and measurability of angular distribution for low-energy laser-driven accelerated ions”. In: *Review of Scientific Instruments* 91.5 (May 2020). ISSN: 1089-7623. DOI: 10.1063/5.0005450.

[33] K. Harres et al. “Development and calibration of a Thomson parabola with microchannel plate for the detection of laser-accelerated MeV ions”. In: *Review of Scientific Instruments* 79.9 (Sept. 2008). ISSN: 1089-7623. DOI: 10.1063/1.2987687.

[34] F. Schillaci et al. “Calibration and energy resolution study of a high dispersive power Thomson Parabola Spectrometer with monochromatic proton beams”. In: *Journal of Instrumentation* 9.10 (Oct. 2014), T10003–T10003. ISSN: 1748-0221. DOI: 10.1088/1748-0221/9/10/t10003.

[35] Ahmed M. Elsied et al. “Characteristics of Ions Emission from Ultrashort Laser Produced Plasma”. In: *Scientific Reports* 6.1 (Dec. 2016). ISSN: 2045-2322. DOI: 10.1038/srep38256.

[36] M. Nantel et al. “Temporal contrast in Ti:sapphire lasers, characterization and control”. In: *IEEE Journal of Selected Topics in Quantum Electronics* 4.2 (1998), pp. 449–458. ISSN: 1077-260X. DOI: 10.1109/2944.686755.

[37] T. Grismayer and P. Mora. “Influence of a finite initial ion density gradient on plasma expansion into a vacuum”. In: *Physics of Plasmas* 13.3 (Mar. 2006). ISSN: 1089-7674. DOI: 10.1063/1.2178653.

[38] S.C. Wilks and W.L. Kruer. “Absorption of ultrashort, ultra-intense laser light by solids and overdense plasmas”. In: *IEEE Journal of Quantum Electronics* 33.11 (1997), pp. 1954–1968. ISSN: 0018-9197. DOI: 10.1109/3.641310.

[39] S. Amoruso et al. “Thermal and nonthermal ion emission during high-fluence femtosecond laser ablation of metallic targets”. In: *Applied Physics Letters* 77.23 (Dec. 2000), pp. 3728–3730. ISSN: 1077-3118. DOI: 10.1063/1.1329869.

[40] Scott D. Baalrud and Jérôme Daligault. "Temperature anisotropy relaxation of the one-component plasma". In: *Contributions to Plasma Physics* 57.6–7 (June 2017), pp. 238–251. ISSN: 1521-3986. DOI: 10.1002/ctpp.201700028.

[41] Guy Dimonte and Jerome Daligault. "Molecular-Dynamics Simulations of Electron-Ion Temperature Relaxation in a Classical Coulomb Plasma". In: *Physical Review Letters* 101.13 (Sept. 2008), p. 135001. ISSN: 1079-7114. DOI: 10.1103/physrevlett.101.135001.

[42] Gérald Faussurier. "Electron-ion coupling factor for temperature relaxation in dense plasmas". In: *Physical Review E* 101.2 (Feb. 2020), p. 023206. ISSN: 2470-0053. DOI: 10.1103/physreve.101.023206.

[43] G. Hazak et al. "Temperature relaxation in two-temperature states of dense electron-ion systems". In: *Physical Review E* 64.6 (Nov. 2001), p. 066411. ISSN: 1095-3787. DOI: 10.1103/physreve.64.066411.

[44] V. Yu. Bychenkov et al. "Ion acceleration in expanding multispecies plasmas". In: *Physics of Plasmas* 11.6 (June 2004), pp. 3242–3250. ISSN: 1089-7674. DOI: 10.1063/1.1738649.

[45] André Anders. "Ion charge state distributions of vacuum arc plasmas: The origin of species". In: *Physical Review E* 55.1 (Jan. 1997), pp. 969–981. ISSN: 1095-3787. DOI: 10.1103/physreve.55.969.

[46] André Anders. "The evolution of ion charge states in cathodic vacuum arc plasmas: a review". In: *Plasma Sources Science and Technology* 21.3 (May 2012), p. 035014. ISSN: 1361-6595. DOI: 10.1088/0963-0252/21/3/035014.

[47] A. Anders. "Plasma fluctuations, local partial Saha equilibrium, and the broadening of vacuum-arc ion charge state distributions". In: *IEEE Transactions on Plasma Science* 27.4 (1999), pp. 1060–1067. ISSN: 0093-3813. DOI: 10.1109/27.782282.

[48] T. R. Preston et al. "Measurements of the K -Shell Opacity of a Solid-Density Magnesium Plasma Heated by an X-Ray Free-Electron Laser". In: *Physical Review Letters* 119.8 (Aug. 2017), p. 085001. ISSN: 1079-7114. DOI: 10.1103/physrevlett.119.085001.

[49] L. B. Fletcher et al. "Electron-Ion Temperature Relaxation in Warm Dense Hydrogen Observed With Picosecond Resolved X-Ray Scattering". In: *Frontiers in Physics* 10 (Mar. 2022). ISSN: 2296-424X. DOI: 10.3389/fphy.2022.838524.

[50] Steffen Mittelmann et al. "Hydrogen isotope analysis in W-tiles using fs-LIBS". In: *Scientific Reports* 13.1 (Feb. 2023). ISSN: 2045-2322. DOI: 10.1038/s41598-023-29138-2.

[51] C. Aragón and J.A. Aguilera. "Characterization of laser induced plasmas by optical emission spectroscopy: A review of experiments and methods". In: *Spectrochimica Acta Part B: Atomic Spectroscopy* 63.9 (Sept. 2008), pp. 893–916. ISSN: 0584-8547. DOI: 10.1016/j.sab.2008.05.010.

[52] R. Ramis et al. "MULTI-fs – A computer code for laser–plasma interaction in the femtosecond regime". In: *Computer Physics Communications* 183.3 (Mar. 2012), pp. 637–655. ISSN: 0010-4655. DOI: 10.1016/j.cpc.2011.10.016.

[53] Jean-Claude Diels and Wolfgang Rudolph. *Ultrashort laser pulse phenomena. Fundamentals, techniques, and applications on a femtosecond time scale.* Ed. by Jean-Claude Diels and Wolfgang Rudolph. 2nd ed. Optics and photonics. Previous ed.: 1996. - Includes bibliographical references and index. - Description based on print version record. Amsterdam: Elsevier, 2006. 652 pp. ISBN: 9780122154935. DOI: 10.1016/b978-0-12-215493-5.x5000-9.

[54] C. Iaconis and I.A. Walmsley. "Self-referencing spectral interferometry for measuring ultrashort optical pulses". In: *IEEE Journal of Quantum Electronics* 35.4 (Apr. 1999), pp. 501–509. ISSN: 0018-9197. DOI: 10.1109/3.753654.

[55] Daniel J. Kane and Rick Trebino. "Single-shot measurement of the intensity and phase of an arbitrary ultrashort pulse by using frequency-resolved optical gating". In: *Optics Letters* 18.10 (May 1993), p. 823. ISSN: 1539-4794. DOI: 10.1364/ol.18.000823.

[56] Rick Trebino et al. "Measuring ultrashort laser pulses in the time-frequency domain using frequency-resolved optical gating". In: *Review of Scientific Instruments* 68.9 (Sept. 1997), pp. 3277–3295. ISSN: 1089-7623. DOI: 10.1063/1.1148286.

[57] Miguel Miranda et al. "Characterization of broadband few-cycle laser pulses with the d-scan technique". In: *Optics Express* 20.17 (Aug. 2012), p. 18732. ISSN: 1094-4087. DOI: 10.1364/oe.20.018732.

[58] Hyo-Chang Kim and Yeon H. Lee. "Hermite–Gaussian and Laguerre–Gaussian beams beyond the paraxial approximation". In: *Optics Communications* 169.1–6 (Oct. 1999), pp. 9–16. ISSN: 0030-4018. DOI: 10.1016/s0030-4018(99)00411-3.

[59] Orazio Svelto. *Principles of Lasers.* Springer US, 2010. ISBN: 9781441913029. DOI: 10.1007/978-1-4419-1302-9.

[60] Amnon Yariv. *Optical waves in crystals. Propagation and control of laser radiation.* Ed. by Pochi Yeh. Wiley classics library ed. Wiley classics library. "Wiley-Interscience." - Originally published: New York, c1984 - Includes bibliographies and index. Hoboken, NJ: Wiley, 2003. 589 pp. ISBN: 0471430811.

[61] Xinke Wang et al. "Longitudinal field characterization of converging terahertz vortices with linear and circular polarizations". In: *Optics Express* 24.7 (Mar. 2016), p. 7178. ISSN: 1094-4087. DOI: 10.1364/oe.24.007178.

[62] P. Colosimo et al. "Scaling strong-field interactions towards the classical limit". In: *Nature Physics* 4.5 (Mar. 2008), pp. 386–389. ISSN: 1745-2481. DOI: 10.1038/nphys914.

[63] H. R. Reiss. "Unsuitability of the Keldysh parameter for laser fields". In: *Physical Review A* 82.2 (Aug. 2010), p. 023418. ISSN: 1094-1622. DOI: 10.1103/physreva.82.023418.

[64] W. Rozmus and V. T. Tikhonchuk. "Skin effect and interaction of short laser pulses with dense plasmas". In: *Physical Review A* 42.12 (Dec. 1990), pp. 7401–7412. ISSN: 1094-1622. DOI: 10.1103/physreva.42.7401.

[65] W. Rozmus, V. T. Tikhonchuk, and R. Cauble. "A model of ultrashort laser pulse absorption in solid targets". In: *Physics of Plasmas* 3.1 (Jan. 1996), pp. 360–367. ISSN: 1089-7674. DOI: 10.1063/1.871861.

[66] J. P. Palastro et al. "Resonance absorption of a broadband laser pulse". In: *Physics of Plasmas* 25.12 (Dec. 2018). ISSN: 1089-7674. DOI: 10.1063/1.5063589.

[67] F. Brunel. "Not-so-resonant, resonant absorption". In: *Physical Review Letters* 59.1 (July 1987), pp. 52–55. ISSN: 0031-9007. DOI: 10.1103/physrevlett.59.52.

[68] Robert J. Goldston and Paul H. Rutherford. *Introduction to plasma physics.* Ed. by Paul H. Rutherford. Reprinted. Literaturverz. S. 485 - 486. Bristol [u.a.]: Inst. of Physics Publ., 2003. 491 pp. ISBN: 9780750301831.

[69] W Fundamenski and OE Garcia. "Comparison of Coulomb collision rates in the plasma physics and magnetically confined fusion literature". In: *Report No. EFDA-JET-R (07) 01* (2007).

[70] Jérôme Daligault and Dmitry Mozyrsky. "Ion dynamics and energy relaxation rate in nonequilibrium electron-ion systems". In: *Physical Review E* 75.2 (Feb. 2007), p. 026402. ISSN: 1550-2376. DOI: 10.1103/physreve.75.026402.

[71] G. Cristoforetti et al. “Local Thermodynamic Equilibrium in Laser-Induced Breakdown Spectroscopy: Beyond the McWhirter criterion”. In: *Spectrochimica Acta Part B: Atomic Spectroscopy* 65.1 (Jan. 2010), pp. 86–95. ISSN: 0584-8547. DOI: 10.1016/j.sab.2009.11.005.

[72] Henri van Regemorter. “Rate of Collisional Excitation in Stellar Atmospheres.” In: *The Astrophysical Journal* 136 (Nov. 1962), p. 906. ISSN: 1538-4357. DOI: 10.1086/147445.

[73] P. Hannaford. “The Oscillator Strength in Atomic Absorption Spectroscopy”. In: *Microchemical Journal* 63.1 (Sept. 1999), pp. 43–52. ISSN: 0026-265X. DOI: 10.1006/mchj.1999.1766.

[74] A. W. Weiss. “Superposition of Configurations and Atomic Oscillator Strengths—Carbon i and ii”. In: *Physical Review* 162.1 (Oct. 1967), pp. 71–80. ISSN: 0031-899X. DOI: 10.1103/physrev.162.71.

[75] Takashi Fujimoto and R. W. P. McWhirter. “Validity criteria for local thermodynamic equilibrium in plasma spectroscopy”. In: *Physical Review A* 42.11 (Dec. 1990), pp. 6588–6601. ISSN: 1094-1622. DOI: 10.1103/physreva.42.6588.

[76] John D. Hey. “Criteria for local thermal equilibrium in non-hydrogenic plasmas”. In: *Journal of Quantitative Spectroscopy and Radiative Transfer* 16.1 (Jan. 1976), pp. 69–75. ISSN: 0022-4073. DOI: 10.1016/0022-4073(76)90124-2.

[77] G. Cristoforetti, E. Tognoni, and L.A. Gizzi. “Thermodynamic equilibrium states in laser-induced plasmas: From the general case to laser-induced breakdown spectroscopy plasmas”. In: *Spectrochimica Acta Part B: Atomic Spectroscopy* 90 (Dec. 2013), pp. 1–22. ISSN: 0584-8547. DOI: 10.1016/j.sab.2013.09.004.

[78] Shudi Zhang et al. “Laser-induced plasma temperature”. In: *Spectrochimica Acta Part B: Atomic Spectroscopy* 97 (July 2014), pp. 13–33. ISSN: 0584-8547. DOI: 10.1016/j.sab.2014.04.009.

[79] K. Eidmann et al. “Hydrodynamic simulation of subpicosecond laser interaction with solid-density matter”. In: *Physical Review E* 62.1 (July 2000), pp. 1202–1214. ISSN: 1095-3787. DOI: 10.1103/physreve.62.1202.

[80] Mofreh R. Zaghloul. “Reduced formulation and efficient algorithm for the determination of equilibrium composition and partition functions of ideal and nonideal complex plasma mixtures”. In: *Physical Review E* 69.2 (Feb. 2004), p. 026702. ISSN: 1550-2376. DOI: 10.1103/physreve.69.026702.

[81] P. Alimohamadi and G. J. Ferland. "A Practical Guide to the Partition Function of Atoms and Ions". In: *Publications of the Astronomical Society of the Pacific* 134.1037 (July 2022), p. 073001. ISSN: 1538-3873. DOI: 10.1088/1538-3873/ac7664.

[82] S. M. Blinder. "Canonical partition function for the hydrogen atom via the Coulomb propagator". In: *Journal of Mathematical Physics* 36.3 (Mar. 1995), pp. 1208–1216. ISSN: 1089-7658. DOI: 10.1063/1.531115.

[83] Giuliano D'Ammando, Gianpiero Colonna, and Mario Capitelli. "A simplified approach to calculate atomic partition functions in plasmas". In: *Physics of Plasmas* 20.3 (Mar. 2013). ISSN: 1089-7674. DOI: 10.1063/1.4794286.

[84] A. Kramida et al. *NIST Atomic Spectra Database*. National Institute of Standards and Technology, Gaithersburg, MD. Version (version 5.12). 2024. DOI: https://doi.org/10.18434/T4W30F. URL: https://physics.nist.gov/asd (visited on 07/31/2025).

[85] Po Yang et al. "The effects of partition function cutoff on spectral temperature measurement in argon plasma". In: *AIP Advances* 14.3 (Mar. 2024). ISSN: 2158-3226. DOI: 10.1063/5.0202284.

[86] Werner Ebeling, Wolf Kraeft, and Dietrich Kremp. *Theory of Bound States and Ionization Equilibrium in Plasmas and Solids*. Jan. 1976. URL: https://www.researchgate.net/publication/316880203_Theory_of_Bound_States_and_Ionization_Equilibrium_in_Plasmas_and_Solids.

[87] Setsuo Ichimaru. "Strongly coupled plasmas: high-density classical plasmas and degenerate electron liquids". In: *Reviews of Modern Physics* 54.4 (Oct. 1982), pp. 1017–1059. ISSN: 0034-6861. DOI: 10.1103/revmodphys.54.1017.

[88] Hans R. Griem. "High-Density Corrections in Plasma Spectroscopy". In: *Physical Review* 128.3 (Nov. 1962), pp. 997–1003. ISSN: 0031-899X. DOI: 10.1103/physrev.128.997.

[89] Yukap Hahn. "Plasma density effects on the three-body recombination rate coefficients". In: *Physics Letters A* 231.1–2 (June 1997), pp. 82–88. ISSN: 0375-9601. DOI: 10.1016/s0375-9601(97)00287-9.

[90] G. Ecker and W. Kröll. "Lowering of the Ionization Energy for a Plasma in Thermodynamic Equilibrium". In: *The Physics of Fluids* 6.1 (Jan. 1963), pp. 62–69. ISSN: 0031-9171. DOI: 10.1063/1.1724509.

[91] O. Ciricosta et al. “Detailed model for hot-dense aluminum plasmas generated by an x-ray free electron laser”. In: *Physics of Plasmas* 23.2 (Feb. 2016). ISSN: 1089-7674. DOI: 10.1063/1.4942540.

[92] John C Stewart and Kedar D Pyatt Jr. “Lowering of ionization potentials in plasmas”. In: *Astrophysical Journal, vol. 144, p. 1203* 144 (1966), p. 1203.

[93] H. Hora. In: *Czechoslovak Journal of Physics* 53.3 (2003), pp. 199–217. ISSN: 0011-4626. DOI: 10.1023/a:1022920829925.

[94] H. Dachraoui, W. Husinsky, and G. Betz. “Ultra-short laser ablation of metals and semiconductors: evidence of ultra-fast Coulomb explosion”. In: *Applied Physics A* 83.2 (Feb. 2006), pp. 333–336. ISSN: 1432-0630. DOI: 10.1007/s00339-006-3499-y.

[95] Xin Zhao and Yung C Shin. “Coulomb explosion and early plasma generation during femtosecond laser ablation of silicon at high laser fluence”. In: *Journal of Physics D: Applied Physics* 46.33 (July 2013), p. 335501. ISSN: 1361-6463. DOI: 10.1088/0022-3727/46/33/335501.

[96] N.M. Bulgakova et al. “A general continuum approach to describe fast electronic transport in pulsed laser irradiated materials: The problem of Coulomb explosion”. In: *Applied Physics A* 81.2 (July 2005), pp. 345–356. ISSN: 1432-0630. DOI: 10.1007/s00339-005-3242-0.

[97] A. Macchi et al. “Radiation pressure and radiation reaction effects in laser-solid interaction”. In: *LAT 2010: International Conference on Lasers, Applications, and Technologies*. Ed. by Vladislav Panchenko, Gérard Mourou, and Aleksei M. Zheltikov. Vol. 7994. SPIE, Sept. 2010, p. 799421. DOI: 10.1117/12.881906.

[98] J. Badziak. “Generation of ultra-intense ion beams by a short-pulse laser”. In: *Radiation Effects and Defects in Solids* 170.4 (Apr. 2015), pp. 256–270. ISSN: 1029-4953. DOI: 10.1080/10420150.2015.1036754.

[99] Yanwen Zhang et al. “Damage profile and ion distribution of slow heavy ions in compounds”. In: *Journal of Applied Physics* 105.10 (May 2009). ISSN: 1089-7550. DOI: 10.1063/1.3118582.

[100] Junji Miyahara et al. “A new type of X-ray area detector utilizing laser stimulated luminescence”. In: *Nuclear Instruments and Methods in Physics Research Section A: Accelerators, Spectrometers, Detectors and Associated Equipment* 246.1–3 (May 1986), pp. 572–578. ISSN: 0168-9002. DOI: 10.1016/0168-9002(86)90156-7.

[101] A. Alejo et al. "Characterisation of deuterium spectra from laser driven multi-species sources by employing differentially filtered image plate detectors in Thomson spectrometers". In: *Review of Scientific Instruments* 85.9 (Sept. 2014). ISSN: 1089-7623. DOI: 10.1063/1.4893780.

[102] I J Paterson et al. "Image plate response for conditions relevant to laser–plasma interaction experiments". In: *Measurement Science and Technology* 19.9 (Aug. 2008), p. 095301. ISSN: 1361-6501. DOI: 10.1088/0957-0233/19/9/095301.

[103] P. Martin et al. "Absolute calibration of Fujifilm BAS-TR image plate response to laser driven protons up to 40 MeV". In: *Review of Scientific Instruments* 93.5 (May 2022). ISSN: 1089-7623. DOI: 10.1063/5.0089402.

[104] V. Lelasseux and J. Fuchs. "Modelling energy deposition in TR image plate detectors for various ion types". In: *Journal of Instrumentation* 15.04 (Apr. 2020), P04002–P04002. ISSN: 1748-0221. DOI: 10.1088/1748-0221/15/04/p04002.

[105] L. Giudicotti. "Time dependent model of gain saturation in microchannel plates and channel electron multipliers". In: *Nuclear Instruments and Methods in Physics Research Section A: Accelerators, Spectrometers, Detectors and Associated Equipment* 659.1 (Dec. 2011), pp. 336–347. ISSN: 0168-9002. DOI: 10.1016/j.nima.2011.07.017.

[106] O Almen et al. "Fast rise time, high sensitivity MCP ion detector for low-energy ion spectroscopy". In: *Journal of Physics E: Scientific Instruments* 22.6 (June 1989), pp. 382–386. ISSN: 0022-3735. DOI: 10.1088/0022-3735/22/6/011.

[107] B Brehm et al. "Absolute detection efficiencies of a microchannel plate detector for ions". In: *Measurement Science and Technology* 6.7 (July 1995), pp. 953–958. ISSN: 1361-6501. DOI: 10.1088/0957-0233/6/7/015.

[108] Steffen Mittelmann et al. "Ablation characteristics of tungsten with ultra-short laser pulses". In: *Journal of Applied Physics* 136.10 (Sept. 2024). ISSN: 1089-7550. DOI: 10.1063/5.0222073.

[109] Marie Ouillé et al. "Relativistic-intensity near-single-cycle light waveforms at kHz repetition rate". In: *Light: Science & Applications* 9.1 (2020), p. 47.

[110] M. Nurhuda et al. "Optimization of hollow fiber pulse compression using pressure gradients". In: *Applied Physics B* 89.2–3 (Oct. 2007), pp. 209–215. ISSN: 1432-0649. DOI: 10.1007/s00340-007-2792-6.

[111] M. Nisoli et al. “Toward a terawatt-scale sub-10-fs laser technology”. In: *IEEE Journal of Selected Topics in Quantum Electronics* 4.2 (1998), pp. 414–420. ISSN: 1077-260X. DOI: 10.1109/2944.686749.

[112] Julian Wegner. “Ablation von Metallen mittels hochintensiver, few-cycle Laserpulse”. In: (2020). URL: https://docserv.uni-duesseldorf.de/servlets/DocumentServlet?id=52441.

[113] Steffen Mittelmann. “Optical Emission Spectroscopy of ultra-short Laser-induced Plasmas”. In: (2023). URL: https://docserv.uni-duesseldorf.de/servlets/DocumentServlet?id=61964.

[114] K. OSVAY et al. “On the temporal contrast of high intensity femtosecond laser pulses”. In: *Laser and Particle Beams* 23.3 (Aug. 2005), pp. 327–332. ISSN: 1469-803X. DOI: 10.1017/s0263034605050469.

[115] *SEQUOIA*. Amplitude. URL: https://amplitude-laser.com/add_ons/metrology/sequoia/ (visited on 03/10/2026).

[116] E. G. Gamaly et al. “Ablation of solids by femtosecond lasers: Ablation mechanism and ablation thresholds for metals and dielectrics”. In: *Physics of Plasmas* 9.3 (Mar. 2002), pp. 949–957. ISSN: 1089-7674. DOI: 10.1063/1.1447555.

[117] Haojie An, Jinshi Wang, and Fengzhou Fang. “Material removal on silicon towards atomic and close-to-atomic scale by infrared femtosecond laser”. In: *Materials Science in Semiconductor Processing* 158 (May 2023), p. 107368. ISSN: 1369-8001. DOI: 10.1016/j.mssp.2023.107368.

[118] Wolfgang Kautek et al. “Laser ablation of dielectrics with pulse durations between 20 fs and 3 ps”. In: *Applied Physics Letters* 69.21 (Nov. 1996), pp. 3146–3148. ISSN: 1077-3118. DOI: 10.1063/1.116810.

[119] H. Mustafa et al. “Effect of surface roughness on the ultrashort pulsed laser ablation fluence threshold of zinc and steel”. In: *Applied Surface Science* 488 (Sept. 2019), pp. 10–21. ISSN: 0169-4332. DOI: 10.1016/j.apsusc.2019.05.066.

[120] Adam Roberts et al. “Response of graphene to femtosecond high-intensity laser irradiation”. In: *Applied Physics Letters* 99.5 (Aug. 2011). ISSN: 1077-3118. DOI: 10.1063/1.3623760.

[121] A. Gil-Villalba et al. “Deviation from threshold model in ultrafast laser ablation of graphene at sub-micron scale”. In: *Applied Physics Letters* 107.6 (Aug. 2015). ISSN: 1077-3118. DOI: 10.1063/1.4928391.

[122] Valter Kiisk et al. “Nanosecond laser treatment of graphene”. In: *Applied Surface Science* 276 (July 2013), pp. 133–137. ISSN: 0169-4332. DOI: 10.1016/j.apsusc.2013.03.047.

[123] S. Amoruso et al. “Experimental and theoretical investigations of femtosecond laser ablation of aluminum in vacuum”. In: *Journal of Applied Physics* 98.4 (Aug. 2005). ISSN: 1089-7550. DOI: 10.1063/1.2032616.

[124] Zhanliang Sun, Matthias Lenzner, and Wolfgang Rudolph. “Generic incubation law for laser damage and ablation thresholds”. In: *Journal of Applied Physics* 117.7 (Feb. 2015). ISSN: 1089-7550. DOI: 10.1063/1.4913282.

[125] Hong-qiang Dou et al. “Femtosecond laser ablation of Al-Mg alloy in vacuum and air”. In: *Applied Surface Science* 447 (July 2018), pp. 388–392. ISSN: 0169-4332. DOI: 10.1016/j.apsusc.2018.04.003.

[126] I.N. Saraeva et al. “Effect of fs/ps laser pulsewidth on ablation of metals and silicon in air and liquids, and on their nanoparticle yields”. In: *Applied Surface Science* 470 (Mar. 2019), pp. 1018–1034. ISSN: 0169-4332. DOI: 10.1016/j.apsusc.2018.11.199.

[127] Xueming Lv et al. “Laser-induced damage threshold of silicon under combined millisecond and nanosecond laser irradiation”. In: *Journal of Applied Physics* 121.11 (Mar. 2017). ISSN: 1089-7550. DOI: 10.1063/1.4978379.

[128] Dongye Zhao et al. “Highly depth-resolved characterization of fusion-related tungsten material based on picosecond laser-induced breakdown spectroscopy”. In: *Journal of Analytical Atomic Spectrometry* 35.12 (2020), pp. 2867–2879. ISSN: 1364-5544. DOI: 10.1039/d0ja00340a.

[129] Hassan Yousefi Oderji et al. “Evaluation of explosive sublimation as the mechanism of nanosecond laser ablation of tungsten under vacuum conditions”. In: *Spectrochimica Acta Part B: Atomic Spectroscopy* 122 (Aug. 2016), pp. 1–8. ISSN: 0584-8547. DOI: 10.1016/j.sab.2016.05.008.

[130] *DMK 37BUX226*. THE IMAGING SOURCE. URL: https://www.theimagingsource.com/de-de/product/industrial/37u/dmk37bux226/ (visited on 03/10/2026).

[131] Jack Tanabe. *Iron Dominated Electromagnets: Design, Fabrication, Assembly and Measurements*. Sept. 2005. DOI: 10.2172/878409.

[132] W. H. Press et al. *Numerical Recipes 3rd Edition: The Art of Scientific Computing. The art of scientific computing*. 3rd Edition. Cambridge University Press, 2007, p. 1235. ISBN: 9780521880688.

[133] Lawrence F. Shampine and Mark W. Reichelt. "The MATLAB ODE Suite". In: *SIAM Journal on Scientific Computing* 18.1 (1997), pp. 1–22. DOI: 10.1137/S1064827594276424. eprint: https://doi.org/10.1137/S1064827594276424. URL: https://doi.org/10.1137/S1064827594276424.

[134] H. C. Burger and P. H. van Cittert. "Wahre und scheinbare Intensitätsverteilung in Spektrallinien". In: *Zeitschrift für Physik* 79.11–12 (Nov. 1932), pp. 722–730. ISSN: 0044-3328. DOI: 10.1007/bf01340490.

[135] H. C. Burger and P. H. van Cittert. "Wahre und scheinbare Intensitätsverteilung in Spektrallinien. II". In: *Zeitschrift für Physik* 81.7–8 (July 1933), pp. 428–434. ISSN: 0044-3328. DOI: 10.1007/bf01342288.

[136] L. Torrisi et al. "Equivalent ion temperature in Ta plasma produced by high energy laser ablation". In: *Journal of Applied Physics* 99.8 (Apr. 2006). ISSN: 1089-7550. DOI: 10.1063/1.2189932.

[137] S. C. Singh et al. "Ion flux enhancements and oscillations in spatially confined laser produced aluminum plasmas". In: *Physics of Plasmas* 21.9 (Sept. 2014). ISSN: 1089-7674. DOI: 10.1063/1.4895601.

[138] P. Nica et al. "Investigation of femtosecond laser-produced plasma from various metallic targets using the Langmuir probe characteristic". In: *Physics of Plasmas* 24.10 (Oct. 2017). ISSN: 1089-7674. DOI: 10.1063/1.5006076.

[139] R Engeln et al. "Flow dynamics and invasion by background gas of a supersonically expanding thermal plasma". In: *Plasma Sources Science and Technology* 10.4 (Oct. 2001), pp. 595–605. ISSN: 1361-6595. DOI: 10.1088/0963-0252/10/4/308.

[140] L. Torrisi et al. "Tantalum ions produced by 1064 nm pulsed laser irradiation". In: *Journal of Applied Physics* 91.7 (Apr. 2002), pp. 4685–4692. ISSN: 1089-7550. DOI: 10.1063/1.1446660.

[141] Krzysztof Sikorski. "Bisection is optimal". In: *Numerische Mathematik* 40.1 (1982), pp. 111–117.

[142] Tjalling J Ypma. "Historical development of the Newton–Raphson method". In: *SIAM review* 37.4 (1995), pp. 531–551.

[143] H.-K. Chung et al. "FLYCHK: Generalized population kinetics and spectral model for rapid spectroscopic analysis for all elements". In: *High Energy Density Physics* 1.1 (Dec. 2005), pp. 3–12. ISSN: 1574-1818. DOI: 10.1016/j.hedp.2005.07.001.

[144] H. K. Chung et al. "FLYCHK manual". In: (2008).

[145] Dilawar Ali, M.Z. Butt, and M. Khaleeq-ur-Rahman. "Ablation yield and angular distribution of ablated particles from laser-irradiated metals: The most fundamental determining factor". In: *Applied Surface Science* 257.7 (Jan. 2011), pp. 2854–2860. ISSN: 0169-4332. DOI: 10.1016/j.apsusc.2010.10.080.

[146] B. Verhoff, S. S. Harilal, and A. Hassanein. "Angular emission of ions and mass deposition from femtosecond and nanosecond laser-produced plasmas". In: *Journal of Applied Physics* 111.12 (June 2012). ISSN: 1089-7550. DOI: 10.1063/1.4730444.

[147] T Matsuoka et al. "Focus optimization of relativistic self-focusing for anomalous laser penetration into overdense plasmas (super-penetration)". In: *Plasma Physics and Controlled Fusion* 50.10 (Sept. 2008), p. 105011. ISSN: 1361-6587. DOI: 10.1088/0741-3335/50/10/105011.

[148] M. Cerchez et al. "ARCTURUS laser: a versatile high-contrast, high-power multi-beam laser system". In: *High Power Laser Science and Engineering* 7 (2019). ISSN: 2052-3289. DOI: 10.1017/hpl.2019.21.

[149] R. S. Craxton and R. L. McCrory. "Hydrodynamics of thermal self-focusing in laser plasmas". In: *Journal of Applied Physics* 56.1 (July 1984), pp. 108–117. ISSN: 1089-7550. DOI: 10.1063/1.333742.

[150] M. Kempe and W. Rudolph. "Impact of chromatic and spherical aberration on the focusing of ultrashort light pulses by lenses". In: *Optics Letters* 18.2 (Jan. 1993), p. 137. ISSN: 1539-4794. DOI: 10.1364/ol.18.000137.

[151] S. Fourmaux et al. "Pedestal cleaning for high laser pulse contrast ratio with a 100 TW class laser system". In: *Optics Express* 19.9 (Apr. 2011), p. 8486. ISSN: 1094-4087. DOI: 10.1364/oe.19.008486.

[152] S. Bastiani et al. "Experimental study of the interaction of subpicosecond laser pulses with solid targets of varying initial scale lengths". In: *Physical Review E* 56.6 (Dec. 1997), pp. 7179–7185. ISSN: 1095-3787. DOI: 10.1103/physreve.56.7179.

[153] T D Arber et al. "Contemporary particle-in-cell approach to laser-plasma modelling". In: *Plasma Physics and Controlled Fusion* 57.11 (Nov. 2015), pp. 1–26. DOI: http://dx.doi.org/10.1088/0741-3335/57/11/113001. URL: https://epochpic.github.io/documentation.html.

[154] ChuanLiang Wang et al. "Strong-field atomic ionization in elliptically polarized laser fields". In: *Physical Review A* 90.1 (July 2014), p. 013422. ISSN: 1094-1622. DOI: 10.1103/physreva.90.013422.

[155] J Badziak et al. "Production of ultrahigh ion current densities at skin-layer subrelativistic laser–plasma interaction". In: *Plasma Physics and Controlled Fusion* 46.12B (Nov. 2004), B541–B555. ISSN: 1361-6587. DOI: 10.1088/0741-3335/46/12b/044.

[156] E. Yazdani et al. "Layers from initial Rayleigh density profiles by directed nonlinear force driven plasma blocks for alternative fast ignition". In: *Laser and Particle Beams* 27.1 (Jan. 2009), pp. 149–156. ISSN: 1469-803X. DOI: 10.1017/s0263034609000214.

[157] R. Stoian et al. "Coulomb explosion in ultrashort pulsed laser ablation ofAl2O3". In: *Physical Review B* 62.19 (Nov. 2000), pp. 13167–13173. ISSN: 1095-3795. DOI: 10.1103/physrevb.62.13167.

[158] E. Fourkal, I. Velchev, and C.-M. Ma. "Coulomb explosion effect and the maximum energy of protons accelerated by high-power lasers". In: *Physical Review E* 71.3 (Mar. 2005), p. 036412. ISSN: 1550-2376. DOI: 10.1103/physreve.71.036412.

[159] M.S. Cho et al. "Opacity calculation for aluminum, iron, and gold plasmas using FLYCHK code". In: *Journal of Quantitative Spectroscopy and Radiative Transfer* 257 (Dec. 2020), p. 107369. ISSN: 0022-4073. DOI: 10.1016/j.jqsrt.2020.107369.

[160] C. T. Chantler et al. *X-Ray Form Factor, Attenuation and Scattering Tables*. National Institute of Standarts and Technology, Nist. Version (version 2.1). 2005. DOI: https://dx.doi.org/10.18434/T4HS32. URL: http://physics.nist.gov/ffast (visited on 07/31/2025).

[161] M. J. Berger et al. *XCOM: Photon Cross Section Database*. National Institute of Standards and Technology, Gaithersburg, MD. Version (version 1.5). 2010. DOI: https://dx.doi.org/10.18434/T48G6X. URL: http://physics.nist.gov/xcom (visited on 07/31/2025).

[162] J. H. Hubbell and S. M. Seltzer. *Tables of X-Ray Mass Attenuation Coefficients and Mass Energy-Absorption Coefficients*. National Institute of Standards and Technology, Gaithersburg, MD. Version (version 1.4). 2004. DOI: https://dx.doi.org/10.18434/T4D01F. URL: http://physics.nist.gov/xaamdi (visited on 07/31/2025).

[163] E.M. Gullikson B.L. Henke and J.C. Davis. "X-ray interactions: photoabsorption, scattering, transmission, and reflection at E=50-30000 eV, Z=1-92". In: *Atomic Data and Nuclear Data Tables* Vol. 54 (no.2) (1993), pp. 181–342. URL: https://henke.lbl.gov (visited on 2025).

[164] Malay Dalui et al. "Mass selection in laser-plasma ion accelerator on nanostructured surfaces". In: *Physics of Plasmas* 24.1 (Jan. 2017). ISSN: 1089-7674. DOI: 10.1063/1.4973887.

[165] Ming Shian Li et al. "Electrically Switchable High-Fold-Helix Spiral Phase Plate Based on Polymer Dispersed Liquid Crystals". In: *Applied Physics Express* 6.11 (Nov. 2013), p. 112201. ISSN: 1882-0786. DOI: 10.7567/apex.6.112201.

[166] Jose Francisco Algorri et al. "Generation of Optical Vortices by an Ideal Liquid Crystal Spiral Phase Plate". In: *IEEE Electron Device Letters* 35.8 (Aug. 2014), pp. 856–858. ISSN: 1558-0563. DOI: 10.1109/led.2014.2331339.

[167] Jan Riedlinger et al. "Temperature and density measurement of an ultra short laser pulse driven carbon plasma by skin-layer ion emission analysis". In: *Journal of Applied Physics* 137.19 (May 2025). ISSN: 1089-7550. DOI: 10.1063/5.0265555.

[168] Jan Riedlinger et al. "Dynamics of supra-thermal carbon ion emission driven by single and double femtosecond-laser-pulses". In: *Physics of Plasmas* 33.1 (Jan. 2026). ISSN: 1089-7674. DOI: 10.1063/5.0303467.

Appendix

Knife edge spectroscopy

To measure the virtual size of a light or particle source, so-called knife spectroscopy can be used. Here, a well defined edge is inserted partially into the beam, which creates a step function P on the detector. If we assume the source resembles a Gaussian shape $I(x) = A\exp(-(x/\xi)^2)$ with width ξ, P can be analytically expressed as:

$$P(h) = \int_h^\infty I(x)\,\mathrm{d}x \tag{5.1}$$

$$= \int_h^\infty A\exp\left(-\left(\frac{x}{\xi}\right)^2\right)\mathrm{d}x \tag{5.2}$$

$$= A^*\left[|\xi| - \xi\cdot\mathrm{erf}\left(\frac{h}{\xi}\right)\right] \quad . \tag{5.3}$$

Fitting the analytical to measured step function, ξ can be derived from the steepness of the step. As ξ is expected to be smaller or similar to the µm detector resolution, a geometrically favorable setup must be used. In such a setting, the knife edge is placed close to the plasma, at a distance $a = 2.6\,\mathrm{cm}$, and further away from the detector, with distance $b = 65\,\mathrm{cm}$. Therefore, the geomet-

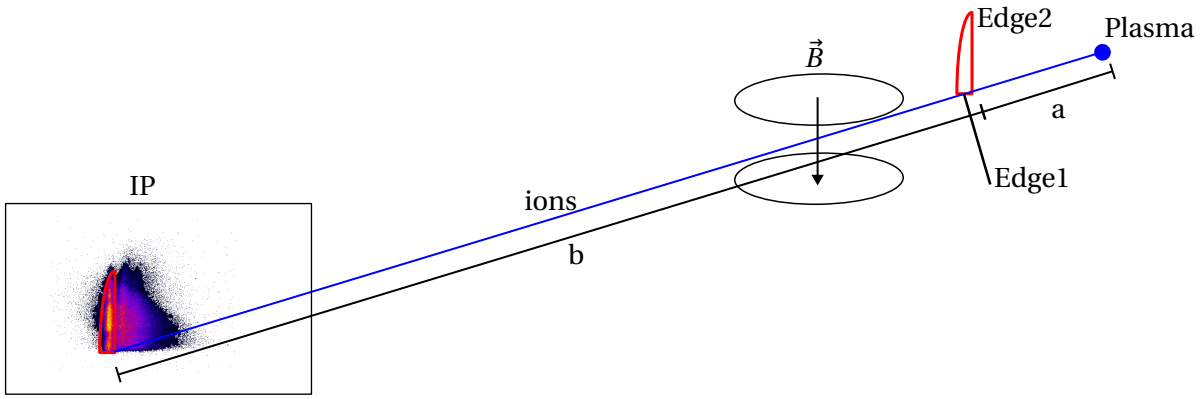

Figure 5.1: Experimental setup of the knife edge spectroscopy.

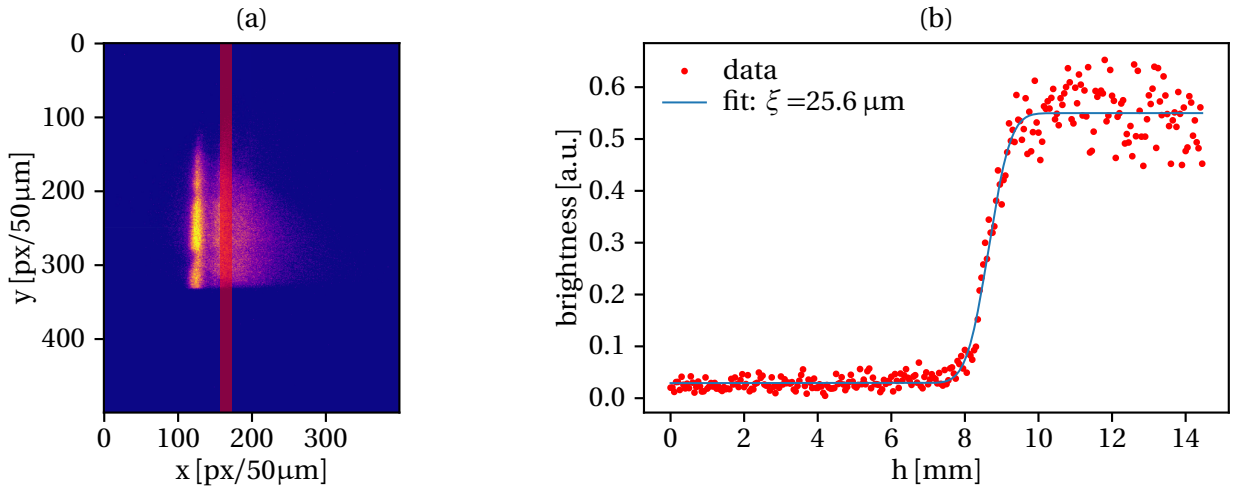

Figure 5.2: (a): Knife edge signal and (b) step function with the corresponding fit.

ric magnification is

$$V = \frac{a+b}{a} \quad . \tag{5.4}$$

A problem arises because the plasma emits X-rays, ions, and electrons in the same direction. To prevent their signals from overlapping, the magnetic field (only) of the Thomson parabola spectrometer was used to separate them horizontally after the edge is introduced. In order to do that, a vertical slit aperture was added, which is visible in Figure 5.2 (a). To the right, the ion signal of the first and second carbon species is apparent. In Figure 5.2 (b), the data points of the lineout indicated in (a) are drawn, as well as the fit of the error function. The parameter of interest $\xi = 26.1\,\mu\text{m}$, multiplied with the inverse magnification of $1/V = 0.0385$ is given in the legend. As the particles are ordered horizontally by charge and impulse, shifting the lineout in this direction, the source size dependent on the deflection is found. Figure 5.3 shows the result in which it be comes apparent that the source size is withing $\xi_{\text{av}} = 22.7 \pm 3.6\,\mu\text{m}$. At deflections close to zero where the signal is due to X-rays, the source size is slightly larger at 30 µm. This is close to the diameter of the laser projected onto the target $\sqrt{2} \cdot 2w_I \approx 25\,\mu\text{m}$ at the defocused position at which the measurement was taken. Note that the width of the intensity is smaller than the one of the electric field $w_I = w/\sqrt{2}$.

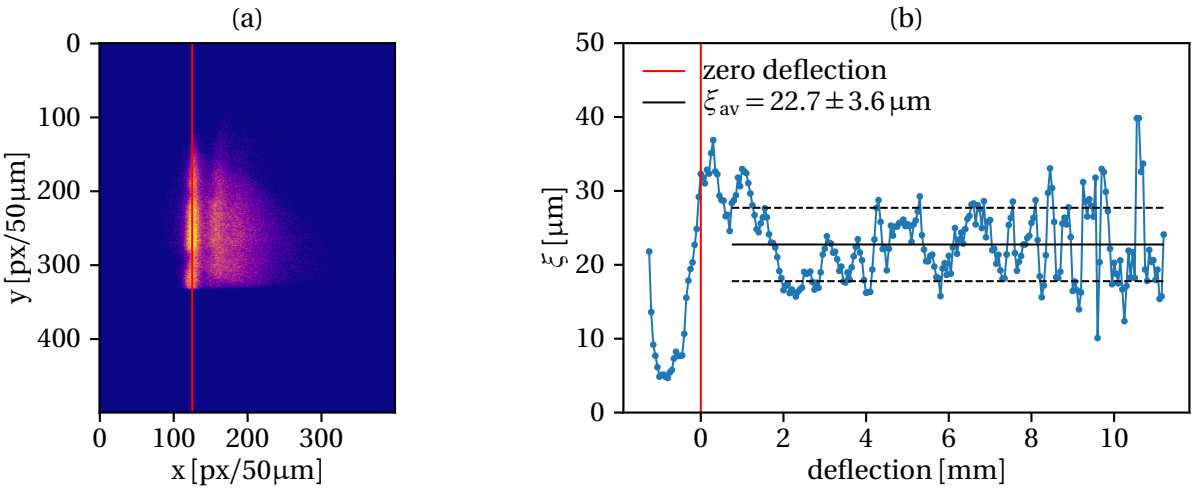

Figure 5.3: (a): Knife edge signal and (b) step function with the corresponding fit.

Ionization tables

In the fort.13 file of the openly available version of MULTI-FS, the ionization tables are saved after the identifier "10002000". The first two fields give the number of density NR and temperature NT values, which span open the grid of tabulated ionizations. Then, the NR density ρ-values follow, and after that, the NT T-values. Finally, NR×NT values holding the average ionization at the (ρ, T)-combination follow. Here, the first NR entries correspond to the given NR ρ-values and the first temperature T_1. The second NR entries correspond again to the given NR ρ-values and the second temperature T_2, and so on. Figure 5.4 shows a comparison between the default aluminum ionization table (a), and the table created with the Saha solver (b). Note that the temperature axis was restricted to more accurately tabulate the region of interest.

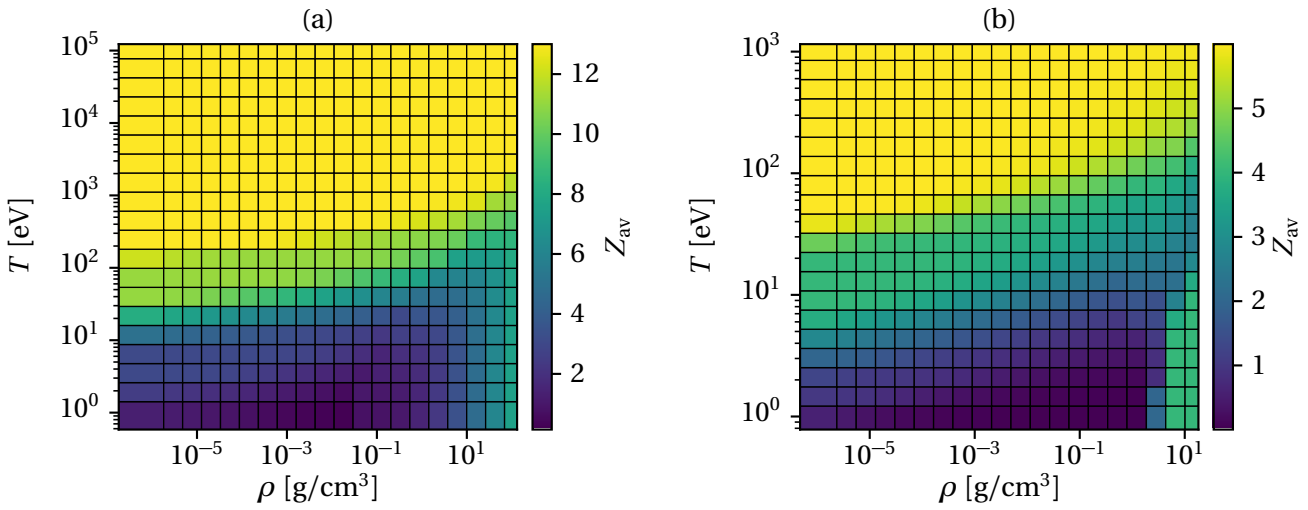

Figure 5.4: Default aluminum ionization table as read from the fort.13 in MULTI-FS.

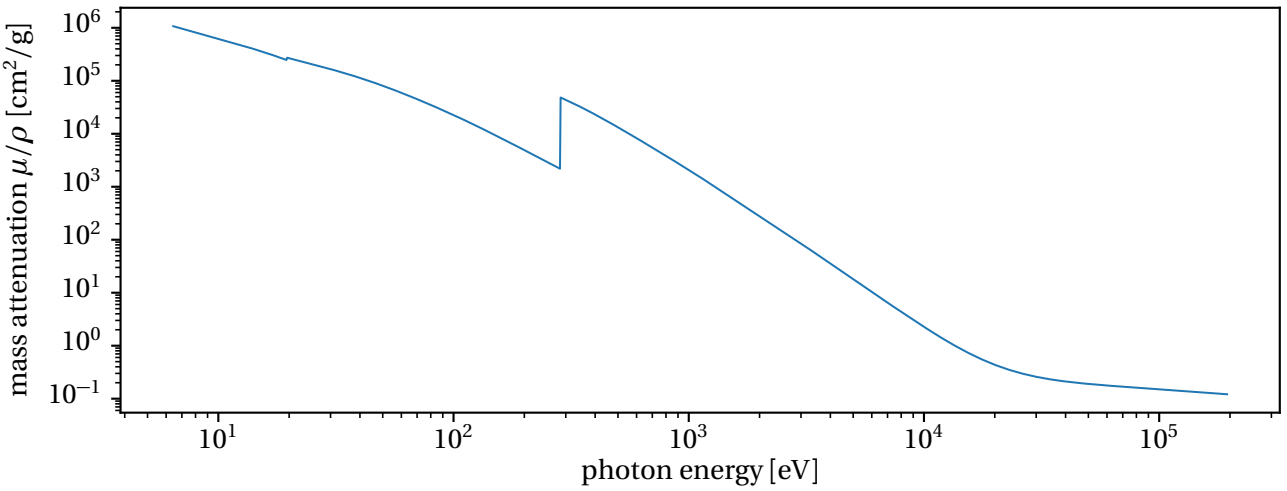

Figure 5.5: Mass attenuation coefficient from the FFAST database [160]. This graph was used to calculate the Plank and Rosseland opacities for MULTI-FS.

Rosseland- and Planck-Opacity

In similar fashion, the mean values for the Rosseland

$$\chi_k^R = \frac{\int_{\nu_{k-1}}^{\nu_k} \frac{\partial I^P(\nu)}{\partial T} \mathrm{d}\nu}{\int_{\nu_{k-1}}^{\nu_k} \frac{1}{\chi(\nu)} \frac{\partial I^P(\nu)}{\partial T} \mathrm{d}\nu} \quad , \tag{5.5}$$

and mean Plank opacities

$$\chi_k^P = \frac{\int_{\nu_{k-1}}^{\nu_k} \chi(\nu) I^P(\nu) \mathrm{d}\nu}{\int_{\nu_{k-1}}^{\nu_k} I^P(\nu) \mathrm{d}\nu} \quad , \tag{5.6}$$

are tabulated after the identifiers "10003000" and "10004000" respectively. The only difference is that after NR and NT, two fields follow, which hold the lower $h\nu_{k-1}$ and upper energy bound $h\nu_k$ of a bin. Therefore, throughout the fort.13 file, the identifiers are repeated for each bin. After that, NR×NT values for the opacity follow. In order to compute the table, two things are needed. The first is the Planck spectral intensity

$$I^P(\nu) = \frac{2h\nu^3}{c^2\left(\exp\left(\frac{h\nu}{kT}\right)-1\right)} \quad , \tag{5.7}$$

and the second one are the mass attenuation coefficients $\chi(\nu)$. For this work, these were read from the FFAST database. The data assumes the attenuation is proportional to the density. In plasma, where the particle composition and energy levels are state dependent, it should be noted that this is strictly speaking not the case. Figure 5.5 shows χ across a large range of photon energies. Note that the range does not go down to 1 eV, which is the smallest bin boundary. This was fixed by simply extrapolating the graph with a constant, using the left most value. Doing so, gives the mass attenuation charts, which are shown in Figure 5.6 and Figure 5.7 in comparison with the default aluminum tables.

Grid in MULTI-FS

In MULTI-FS, the size of the cells in the grid is not initialized to be constant. Rather, it is stacked from one side of the simulation volume to the other according to [52]

$$\Delta r_{i+1} = k \cdot \Delta r_i \quad . \tag{5.8}$$

Here, k is a constant which describes the size progression. For a given layer thickness d, and number of cells N, the relationship is

$$d = \sum_{i=0}^{N-1} \Delta r_i \quad . \tag{5.9}$$

Inserting eq. (5.8), and taking the result of the partial sum of the geometric series yields

$$d = \Delta r_0 \sum_{i=0}^{N-1} k^i \tag{5.10}$$

$$= \Delta r_0 \cdot \frac{1-k^N}{1-k} \quad . \tag{5.11}$$

Therefore, the resolutions of the first, and last cell are

$$\Delta r_0 = \frac{1-k}{1-k^N} d \tag{5.12}$$

$$\Delta r_{N-1} = \frac{1-k}{1-k^N} k^{N-1} d \quad . \tag{5.13}$$

Most simulations were carried out using $k = 1.06$ and $N = 220$, which gives $\Delta r_0 \approx 0.5\,\text{nm}$ and $\Delta r_{N-1} \approx 0.17\,\text{mm}$ at $d = 3\,\text{mm}$.

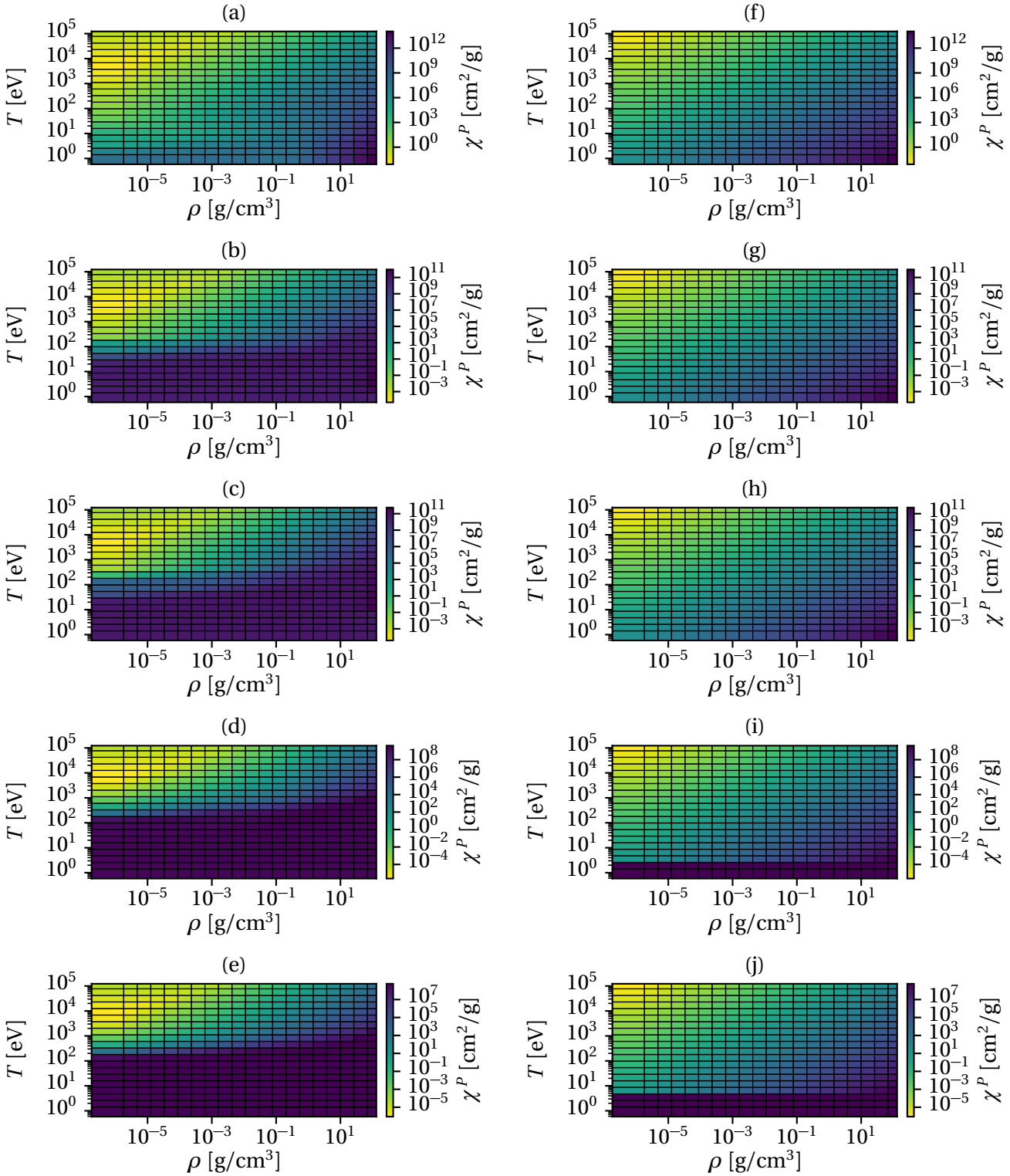

Figure 5.6: Used Planck absorption for the default aluminum (a-e), and carbon (f-j) for photon energies from top to bottom: 1-10 eV, 150-250 eV, 700-900 eV, 2000-2200 eV, 2800-3100 eV.

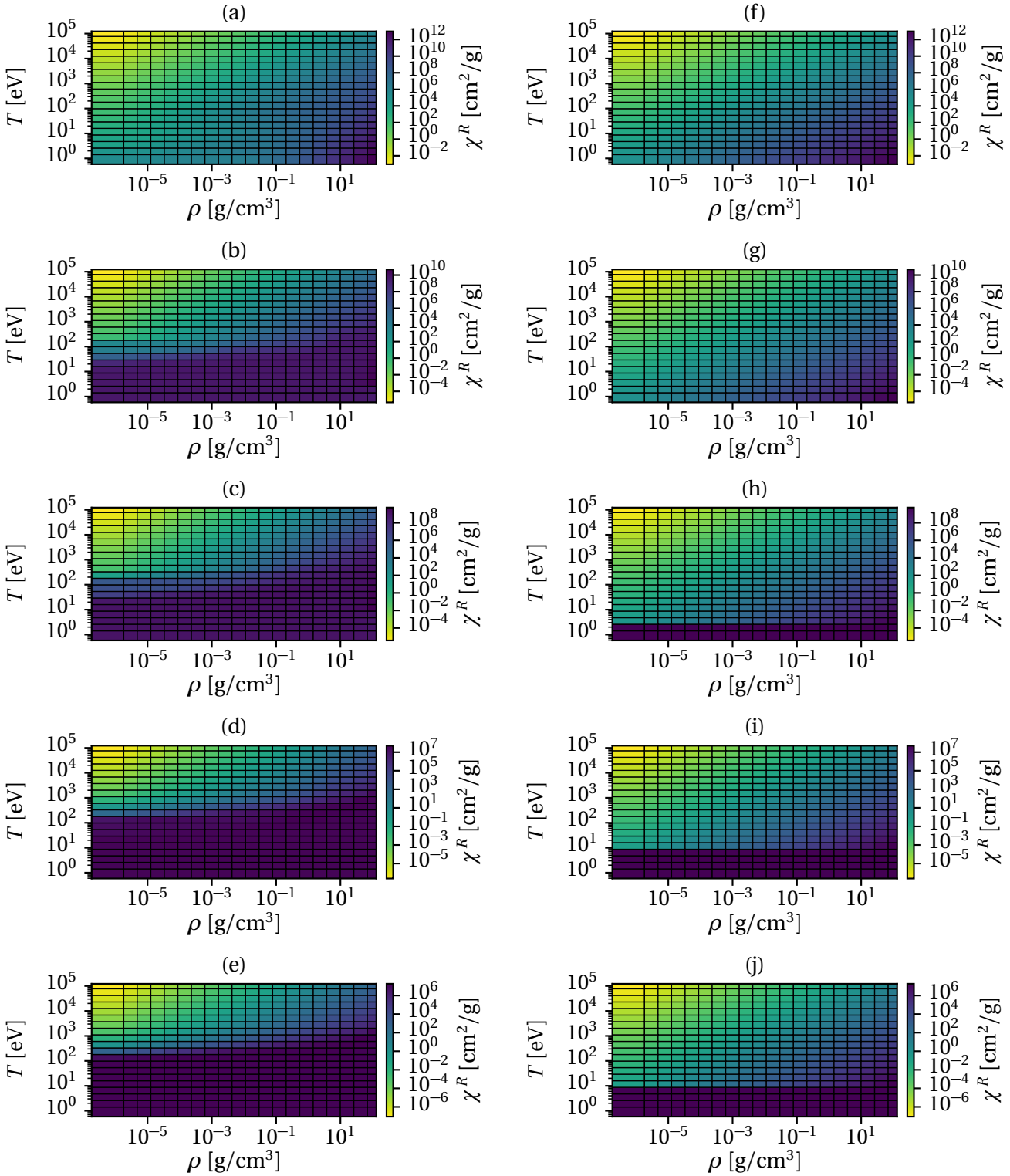

Figure 5.7: Used Rosseland opacities for the default aluminum (a-e), and carbon (f-j) for photon energies from top to bottom: 1-10 eV, 150-250 eV, 700-900 eV, 2000-2200 eV, 2800-3100 eV.

(T,n)-scans

For completeness reasons, here are the temperature and density evaluations of the CSDs as measured by variation of the laser pulse duration.

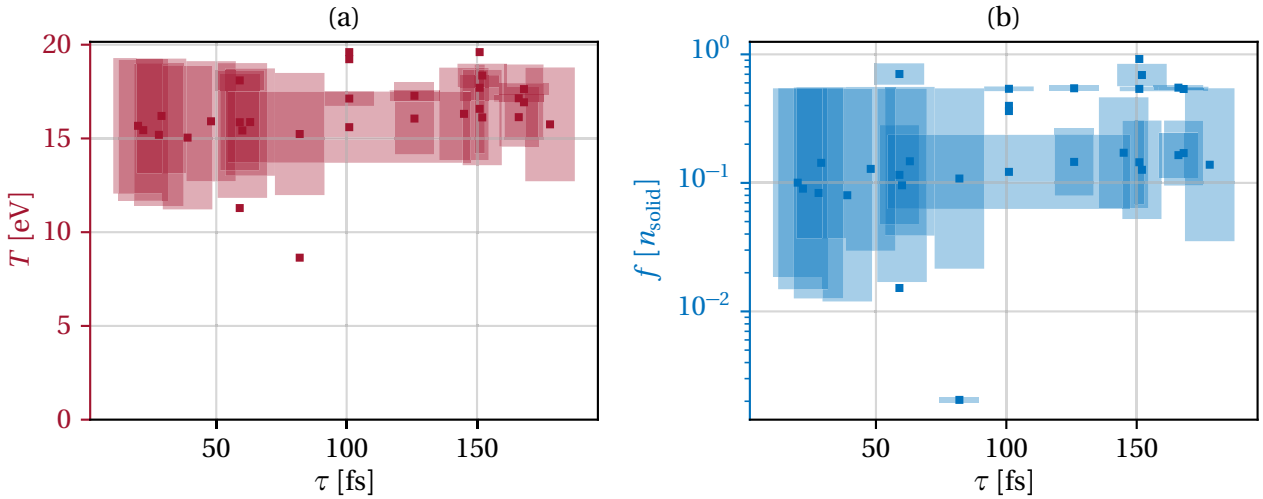

Figure 5.8: Temperatures (a) and densities (b) as found by the CSD analysis for various pulse lengths. Multiple data points indicate the different branches, missing points indicate no agreement of the measured and Saha CSD was found.

Vector beams

As described in the first chapter, the polarization of a laser is usually consistent across the beam profile. This is true for either linear or circular polarization. The PHASER system, however, offers the possibility to generate vector vortex beams, in which the direction of polarization varies across the beam. Such beams can be described in Cartesian coordinates as

$$\vec{E}(t,x,y,z) = \begin{pmatrix} E_0(r)\cos(\theta)\exp(i(\omega t - kz)) \\ E_0(r)\sin(\theta)\exp(i(\omega t - kz)) \\ 0 \end{pmatrix} \quad . \tag{5.14}$$

Here, θ is constant for linear polarization, $\theta = \arctan(x/y)$ for radial polarization, and $\theta = \arctan(x/y) + \pi/2$ for azimuthal polarization, and $r = \sqrt{x^2 + y^2}$ is the radial distance to the optical axis. Figure 5.9 gives a comparison of these three types of beams for different positions in the half cycle. In practice, this is achieved by inserting a **L**iquid **C**rystal **P**olymer (LCP) Vortex Retarder into the beam. This is a type of **L**iquid **C**rystal **S**patial **L**ight **M**odulator (LCSLM) [165, 166], which alters the polarization across the beam profile, as the name suggests.

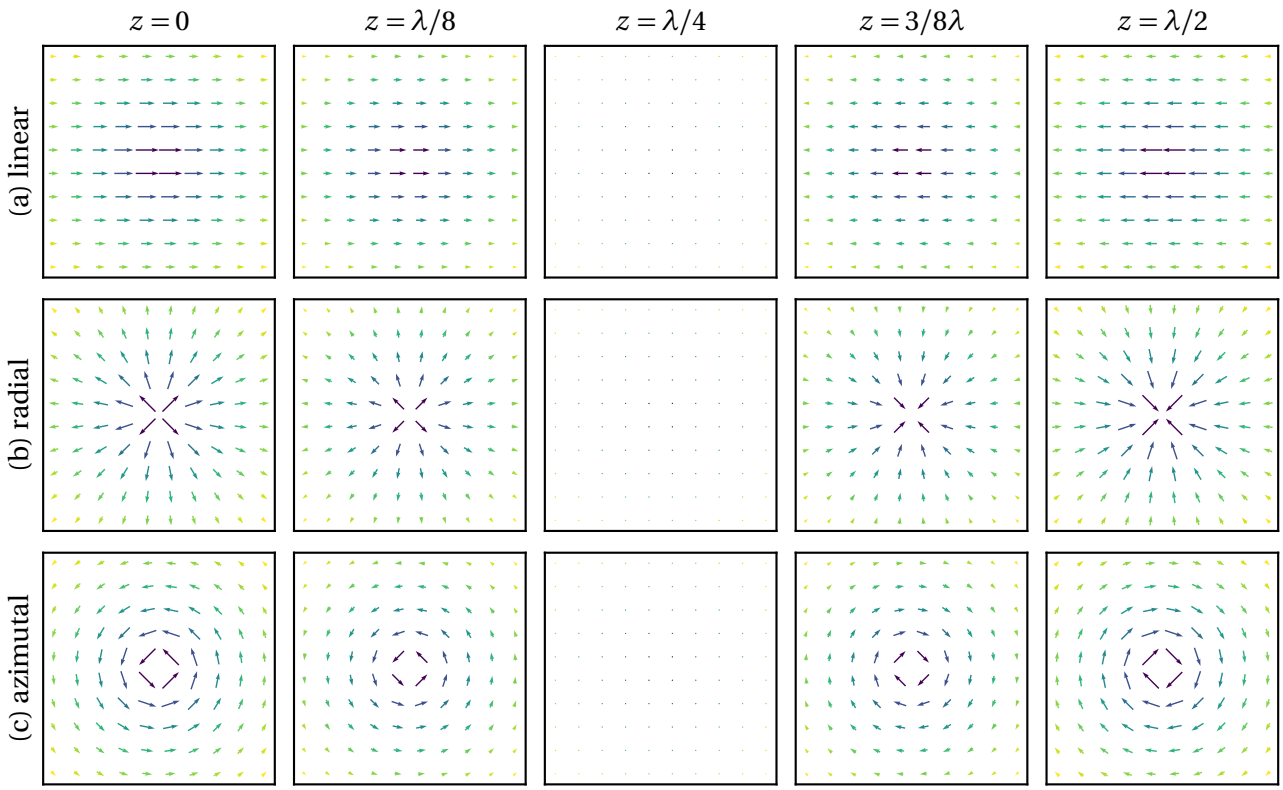

Figure 5.9: A comparison of the different polarization types used to compare the ion yield. In (a, upper row), the propagation of electric field of a linear polarized laser with a gaussian beam profile is shown. (b) and (c) show the same step for radial and azimutal polarization respectively.

Publications

Peer-reviewed articles

Jan Riedlinger, Lars Torben Schwabe, Qëndresa Ibraimi, Georg Pretzer, **Electromagnetic Thomson parabola spectrometer for detection of fs laser-driven keV ions**. AIP Advances 1 August 2024; 14 (8): 085304 doi:10.1063/5.0212122
Key contributions to the publication:

- Writing and editing in draft and review
- Conceptualization and realization of the experimental setup
- Supervision and participation in data acquisition, curation, and visualization
- Lead in methodology

Steffen Mittelmann, Jan Riedlinger, Benedikt Buchner, Thomas Schwarz-Selinger, Matej Mayer, Georg Pretzler, **Ablation characteristics of tungsten with ultra-short laser pulses**. J. Appl. Phys. 14 September 2024; 136 (10): 103103 doi:10.1063/5.0222073
Key contributions to the publication:

- Conceptualization
- Data acquisition
- Methodology

Jan Riedlinger, Qëndresa Ibraimi, Lars Torben Schwabe, Simon Lohnert, Georg Pretzler, **Temperature and density measurement of an ultra short laser pulse driven carbon plasma by skin-layer ion emission analysis**. J. Appl. Phys. 21 May 2025; 137 (19): 193301doi:10.1063/5.0265555
Key contributions to the publication:

- Writing and editing in draft and review
- Conceptualization and realization of the experimental setup
- Supervision and participation in data acquisition, curation, and visualization
- Lead in methodology

Jan Riedlinger, Nico Potzkai, Lars Torben Schwabe, Qëndresa Ibraimi, Daniel Gavva, Georg Pretzler, **Dynamics of supra-thermal carbon ion emission driven by single and double femtosecond-laser-pulses**. Phys. Plasmas 1 January 2026; 33 (1): 012701 doi:10.1063/5.0303467
Key contributions to the publication:

- Writing and editing in draft and review
- Conceptualization and realization of the experimental setup
- Supervision and participation in data acquisition, curation, and visualization
- Lead in methodology

Manuscript in preparation

Jan Riedlinger, Nico Potzkai, Marc Osenberg, Lars Torben Schwabe, Georg Pretzler,**Local thermodynamic equilibrium in laser-solid interaction modeled by hydrodynamic simulations** Key contributions to the unsubmitted manuscript:

- Writing and editing in draft and review
- Conceptualization and realization of the experimental setup
- Supervision and participation in data acquisition, curation, and visualization
- Lead in methodology

Taken from Publications

For this thesis, parts of the publications were used in altered and unaltered form. Slight changes were made in terms of wording and visual representations to fit the template and writing of this work.

Electromagnetic Thomson parabola spectrometer for detection of fs laser-driven keV ions [12]
The parts of this work concerned with ion spectroscopy, are predominantly taken from this reference. These parts appear mainly chapter 1, 2, 3, and 5 (2.4, 3.2).

Temperature and density measurement of an ultra short laser pulse driven carbon plasma by skin-layer ion emission analysis [167]
The parts of this work concerned with plasma parameters, are mainly taken from this reference. This includes predominantly parts of chapter 1, 2, 3, 4, and 5 (2.3, 3.3, 3.4, 4.2).

Dynamics of supra-thermal carbon ion emission driven by single and double femtosecond-laser-pulses [168]
The parts of this work concerned with ion emission, are mainly taken from this reference. This includes mainly parts of chapter 1, 2, 3, 4, and 5 (2.3, 3.3, 3.4, 4.1, 4.3, 4.4, 4.5, 4.6, 4.8).

Local thermodynamic equilibrium in laser-solid interaction modeled by hydrodynamic simulations
The parts of this work concerned with LTE conditions, are mainly taken from this draft. This includes mainly parts of chapter 1, 2, 4, and 5 (2.2, 2.3, 4.8). Not that this manuscript has not been published by the time this work is submitted.

Acronyms

ADK **A**mmosov-**D**elone-**K**rainov 70

AK3 third order **a**uto-**c**orrelator . . . . . 38 f.

ASE self-**a**mplified **s**pontaneous **e**mission 35, 39

ATF **a**mplitude **t**ransfer **f**unction 47

BSI **b**arrier **s**uppression **i**onization . . . . . 10 f.

CCD **c**harge **c**oupled **d**evice . . . . . 27 ff.

CE **C**oulomb **e**xplosion 24

CEP **c**arrier **e**nvelope **p**hase 8, 34

CI **c**ollisional **i**onization 11

CR-39 **C**olumbia **R**esin 39 27

CSB **C**oulomb **s**hifted (Maxwell-)**B**oltzmann 51, 53, 62

CSD **c**harge **s**tate **d**istribution . . . . . 3, 22 f., 56–60, 70, 84 f., 88 f.

CTE **c**omplete **t**hermodynamic **e**quilibrium 14

DH **D**ebye-**H**ückel 20

EEK **e**lectron **e**xcitation **k**inetic 14

EK **E**cker and **K**röll . . . . . 20 f.

EOS **e**quation **o**f **s**tate . . . . . 76 f.

FFT **f**ast **F**ourier **T**ransform 47

FL **f**lourescent **l**ayers 27

FROG **f**requency-**r**esolved **o**ptical **g**ating 9

FS **f**used **s**ilica 40

FT **F**ourier **T**ransform . . . . . 6 f., 50

FWHM **f**ull **w**idth at **h**alf **m**aximum 6, 8, 68

gof **g**oodness **o**f **f**it . . . . . 57 ff.

He:Ne **H**elium **N**eon 29

HHU **H**einrich-**H**eine-**U**niversität 34

iEOS **i**nverted **e**quation **o**f **s**tate 76

IP **i**mage **p**lates . . . . . 27, 29–33, 52, 61 f.

IPD **i**onization **p**otential **d**epression . . . . . 11, 16 ff., 20, 53 ff.

LAR **l**east **a**bsolute **r**esiduals . . . . . 57 ff.

laser **l**ight **a**mplification by **s**timulated **e**mission of **r**adiation 4, 6, 36

LCP **L**iquid **C**rystal **P**olymer 116

LCSLM **L**iquid **C**rystal **S**patial **L**ight **M**odulator 116

LIDT **l**aser **i**nduced **d**amage **t**hreshold . . . . . 36 ff.

LIP **l**aser **i**nduced **p**lasma . . . . . 14 ff.

LTE **l**ocal **t**hermodynamic **e**quilibrium . . . . . 15 f., 21 f., 55, 59, 76, 80 ff., 84, 88 f.

LWFA **l**aser **w**ake **f**ield **a**cceleration 23

MC **M**onte **C**arlo 58

MCP **m**icro **c**hannel **p**lates 24, 27, 29, 31–34

MPI **m**ulti **p**hoton **i**onization . . . . . 10 f.

NIR **n**ear **i**nfra **r**ed 11

OTF **o**ptical **t**ransfer **f**unction 47

PC **P**ockels **c**ell . . . . . 35 f.

PHASER **P**hase-stabilized **H**eine l**aser** . . . . . 34 f., 40, 64

PSF **p**oint **s**pread **f**unction . . . . . 25 ff., 48

PSL **p**hoto-**s**timulated **l**uminescence . . . . . 29 f.

PWM **p**ulse **w**idth **m**odulation 45

QL **q**uantum **l**evel 29

SP **S**tewart and **P**yatt 20, 55, 59

SPIDER **s**ectral **p**hase **i**nterferometry for **d**irect **e**lectric-field **r**econstruction 9, 35, 67

TE **t**hermodynamic **e**quilibrium 15

TEM$_{mn}$ **t**ransvers **e**lectromagnetic **m**odes 9

TF **t**ransfer **f**unction . . . . . 47, 49 f.

TI **t**unnel **i**onization . . . . . 10 f.

TNSA **t**arget **n**normal **s**heet **a**cceleration 23, 68, 74

TOF **t**ime-**o**f-**f**light 24

TPS **T**homson **p**arabola **s**pectrometer . . . . . 2, 24 f., 30, 52, 62 f., 84, 87

VA **v**ariable **a**ttenuator 40

VIS **vis**ible 11

List of Figures

List of Tables

Danksagung

An dieser Stelle möchte ich allen danken, die mich während meines Werdegangs unterstützt und begleitet haben.

Besonderer Dank gilt an dieser Stelle meinem Doktorvater, Prof. **Georg Pretzler**. Zu Beginn der Bachelorarbeit durfte ich Teil des Teams werden und habe so die Möglichkeit bekommen mich intra- und extradisziplinär weiterzuentwickeln. Extradisziplinär ist mir besonders die Corona Zeit im Gedächtnis geblieben, in der Sie keine Mühen gescheut haben um möglichst gute Onlinelehre zu stellen. Das Streaming Setup aufzubauen oder aber auch die Übungszettel auf den online Betrieb umzustellen, war sowohl lehrreich als auch spaßig. Während der Promotion haben Sie sich immer Zeit genommen, um über Physik, nicht nur der Optik, zu diskutieren.

Ebenso gilt mein Dank **Götz Lehmann**, dem Mentor meiner Promotion. Von dir habe ich einen guten Teil meiner Programmierkentnisse. Das war sehr wertvoll, weil mir diese Skills bereits im Studium, aber auch während der Promotion viele Möglichkeiten eröffnet haben. Möglicherweise aber noch wichtiger ist deine Gelassenheit, von der ich immer mal versuche, mir eine Scheibe abzuschneiden.

Als Nächstes möchte ich mich bei meinen ehemaligen Kollegen bedanken, die mir viel mit auf den Weg gegeben haben.

Basti, bei dir hat es quasi angefangen, als du meine Bachelorarbeit betreut hast. Du hast mir von Begin an sehr viel Vertrauen im Labor und bei meiner Arbeit entgegengebracht, wodurch ich stets mein Handeln hinterfragen musste und eigene Fehler machen konnte. Bis heute gilt die Zeit mit dir als Benchmark für mich, wie eine erfolgreiche Betreuung einer Abschlussarbeit aussehen sollte. Deine gute Laune ist ansteckend, so fand ich es immer schön, im benachbarten Büro zu sitzen und lautes Lachen von nebenan zu hören.

Julian, auch wenn sich unsere Zeit (als Doktoranden zumindest) nur kurz überschnitten hat, hat mir die Zeit gefallen. Ohne deine Arbeit am variablen Abschwächer hätte ein Teil meiner Promotion nicht durchgeführt werden können. Viel wichtiger aber finde ich, dass du jemand bist, der auch einen Blick auf die anderen wichtigen Dinge im Leben hat, sowie Sport und Freundschaften. Dieser Blickwinkel hat geholfen, die Promotion ganz gut zu überstehen.

Michael, bei dir möchte ich mich besonders für die gemeinsame Zeit im Büro bedanken. Es herrschte eine angenehme Atmosphäre und dank dir war immer für ausreichend Kaffee gesorgt. Ebenso warst du stets derjenige der für ausreichend Versorgung an Silberspiegeln, Spiegelhaltern, Glassubstaten, PI-Motoren, Kabeln usw. gesorgt hat. Mit dir kann man außerdem nach Feierabend gut die Physik vergessen (auch wenn das auch privat immer ein tolles Gesprächsthema ist).

Steffen, dich als Kollegen und Freund zu haben, hat maßgeblich zu dem Erfolg dieser Arbeit beigetragen. So hast du hast mir z.B. den wichtigsten Ratschlag zum Publizieren gegeben: Einfach anfangen. Aber auch zwischenmenschlich hat es immer gut getan mit dir eine Auszeit von der Physik zu nehmen, sei es in Düsseldorf oder München.

Kommen wir nun zu den aktuellen Kollegen im Institut.

Stefan, bei dir würde ich mich gerne für deinen Einsatz an vielen Fronten bedanken. Quasi alles, was im Labor nicht käuflich ist, ist angefertigt von dir. Du hast immer dafür gesorgt, dass es uns und dem Labor gut geht. Sicherheit kommt bei dir an erster Stelle, und trotzdem findest du für alles eine Lösung. Ohne dich und deinen gesunden Pragmatismus wäre der Laborbetrieb nicht möglich gewesen.

Marc, Nico, Torben, Qëndresa, bei euch muss ich mich auch ganz herzlich für die schöne gemeinsame Zeit bedanken. Ihr habt den Alltag am Institut super angenehm gemacht, egal wie viel Arbeit es gerade zu erledigen gab. Egal was war, zusammen hat es immer funktioniert. Sei es der Aufbau einer neuen Kammer, Justage von Sachen, Programmierung, Automatisierung, Organisatorisches oder sonstigem. Ich finde, wir sind ein ziemlich gutes Team. Aber auch abseits der Arbeit habe ich so das Glück gehabt Freunde zu finden, die besonders für jede (Sport-)Veranstaltung zu haben sind.

Selbstverständlich möchte ich mich auch bei allen **meinen Studenten** bedanken, die mich tatkräftig bei der Umsetzung von Projekten unterstützt haben.

Nicht zu vergessen sind natürlich auch die institutsfernen Freunde und meine Familie, von denen ich immer unterstützt wurde.

Abschließend muss ich **Lisa** besonders danken. Du musstest dir auch nach längeren Arbeitstagen und Nachtschichten einen Haushalt mit mir teilen, und warst, sobald es Probleme gab, immer involviert. Dennoch haben wir es geschafft, uns eine gute Zeit während der Promotion zu machen. Das war definitiv eine Belastungsprobe, und ich freue mich, dass wir so ein gutes Team sind. Vielen Dank, dass du mir wann immer nötig den Rücken freigehalten hast.

Eidesstattliche Versicherung

Ich versichere an Eides Statt, dass die Dissertation von mir selbstständig und ohne unzulässige fremde Hilfe unter Beachtung der „Grundsätze zur Sicherung guter wissenschaftlicher Praxis an der Heinrich-Heine-Universität Düsseldorf“ erstellt worden ist.

Jan Riedlinger
Düsseldorf, 24. März 2026